Analytical Microfluidic Systems Utilizing Multiphase Interfaces and Artificial Heliotropism with Novel Photomechanical Actuators

By

Ye Liu

A dissertation submitted in partial fulfillment
of the requirements for the degree of

Doctor of Philosophy
(Electrical Engineering)
at the
UNIVERSITY OF WISCONSIN-MADISON
2012

Date of final oral examination: 08/17/12

This dissertation is approved by the following members of the Final Oral Committee:

Hongrui Jiang, Professor, Electrical and Computer Engineering
Dan Botez, Professor, Electrical and Computer Engineering
Xiaochun Li, Professor, Mechanical Engineering
Luke Mawst, Professor, Electrical and Computer Engineering
Justin Williams, Associate Professor, Biomedical Engineering

ACKNOWLEDGMENTS

I would like to sincerely thank all those who have helped me and have confidence in me through this path. Without you, it would be unable for me to get this point.

All of the research was performed under the supervision and advice of my advisor, Professor Hongrui Jiang. I appreciate him for giving me the opportunity to work in this group, under his guidance. His patience, guidance, motivation and intelligence have been the beacon to me. I've learned a lot from him not only in the strategy of and attitude towards research, but also in the way how to position myself and handle the important things in life. It was his timely and effective advice that directed me through the path.

I am extremely grateful to Professor Nicolas Abbott for his kindly advice for the LC sensing project. I am also thankful to Professor Justin Williams and his group for showing me the right way to use a fluorescence microscopy. I appreciate all the help and suggestion of my committee members, including Professor Dan Botez, Professor Xiaochun Li, Professor Luke Mawst and Professor Justin Williams.

I also appreciate all the help provided by Dr. Guangyun Lin in the Department of Bacteriology and Dr. Zhongqiang Yang in the Department of Chemical and Biological Engineering at University of Wisconsin-Madison for assistance in inspiring discussions and experimental materials.

It's the versatile facilities at the UW-Madison that enable my progresses and simplifies my research life. Many thanks to the Wisconsin Center for Applied Microelectronics (WCAM) facility at the University of Wisconsin-Madison and their staff (Rebecca Bauer and Dan

Christensen) for training and access to cleanroom facilities. I am also grateful to Richard Noll at the Materials Science Center and Anna Kiyanova at the Soft Material Laboratory at the University of Wisconsin-Madison for assistance in characterizing instruments such as SEM, DSC and TGA. I would also like to thank the student Mechanical Engineering Shop and their staff (Richard Proctor) for training and helping with the machining for mechanical parts. I would like to thank staffs in the ECE department for help with photocopying and paper works.

This work would not have been possible without the many inspiring discussions and technical assistance/consultation with my colleagues at the University of Wisconsin-Madison: Drs. Chi-Wei Lo, Xuefeng Zeng, Difeng Zhu, George Huang, Xi Zhang and, Chenhui Li, Bader Aldalali, Jason Greenwood, David Busacker, Carter Smith, Chi-chieh Huang, Aditi Kanhere, Alireza Ashtiani and Travis Portz. I thank Dr. Chensha Li for his supplement with liquid-crystal elastomers. I would especially thank Dr. Daming Cheng for his inspiring previous work and patiently guidance in the liquid-crystal sensing project.

Coming to the most important person in my life, I would like to thank my parents and my wife, Ying Zheng. It's their help, understanding and giving that walks me through the everyday life.

I also want to thank my grandma for her care, God bless her and she can recover from her recent heart failure.

My work was partly supported by Wisconsin Institutes for Discovery, the U.S. National Science Foundation (Grant number: ECCS 0702095), the U.S. National Science Foundation (Grant number: ECCS 0622202), the US Department of Homeland Security, through a grant awarded to the National Center for Food Protection and Defense at the University of Minnesota (grant number DHS-2007-ST-061-000003), and the Wisconsin Alumni Research Foundation.

Table of Contents

Index of Tables

Index of Figures

Chapter 1. Introduction

1.1 Microfluidic systems, lab-on-a-chip and optofluidic systems

Progresses and demands in molecular analysis, bio-defense and molecular biology have urged the birth of novel, miniaturized (thus portable) and versatile systems, serving as platforms for sensing and testing. Pushed by this trend, microfluidics systems (MFS), which involves channels with dimensions of tens of microns and multi-phase fluidics flowing and interaction in them, have emerged as a distinct new area of research [1]. As a multidisciplinary field, MFS developing intersects engineering, physics, chemistry, microfabrication and biotechnology, and is used in versatile applications such as fuel cells, droplet-based digital microfluidics, micro-propulsion and, especially, lab-on-a-chip (LoC) for analytical purposes.

"Lab-on-a-chip"s (LoCs), or used to be known as micro total analysis systems (µTASs), are extremely important fields inside the whole MFS scope. The concept of LoC has enlightened tremendous research and enabled scaling down from laboratory equipments and supplies that usually take an entire room to the size of tens of millimeters or even sub-millimeters. The advantages of LoC are not limited to the portability, but also include lower-cost (i.e. less material needed for fabrication), much less quantity of reagents and target phase needed for analysis (thus possibly higher concentration and subsequently shorter detection time, higher sensitivity and higher resolution) and the ability to be incorporated with or into a human body.

With the rapid progressing of MFS and LoC systems, the concept optofluidics was coined in 2003 so as to reflect a new research field that combines MFS and optical systems [2]. Fluids exhibit unique properties such as: the ability to change the optical property of the fluid medium within a device by simply replacing one fluid with another; the optically smooth interface between two immiscible fluids; and the ability of flowing streams of miscible fluids to create gradients in optical properties by diffusion. Optofluidic systems utilize these properties to build the optics out of the same fluidic toolkit and thus combine optics and microfluidics on the same chip [3]. Certain optofluidic systems make the fabrication of high quality microscale optical components simpler and more flexible. Moreover, they integrate complex optical sensing and analysis tools and the fluidic sampling channel together, thus provide new methods for analytical applications such as biochemical sensing.

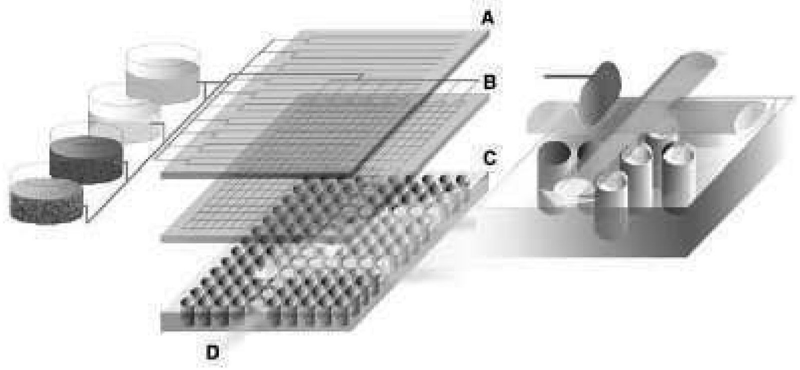

Figure 1-1. A generalized layer construction of an optofluidic device. An optofluidic device typically consists of three layers. a, The topmost layer consists of the microfluidic controls. Microfluidic valves and pumps may be incorporated in this layer. b, The middle layer contains the microfluidic channels. c, The third layer is the optical structure and may contain photonic crystal structures, sensors, sources and waveguides. d, Light can be guided within the third layer. [3]

1.1.1 Microfluidic physics

Microfluidic systems differ from conventional fluidic systems in two major ways: First, the components, especially channels in the systems are in the dimensions of tens of micrometers. Second, according to the small dimensions, the amount of fluid manipulated in the channel is thus very small (10^{-9} to 10^{-8} liters). Thus, certain dominating fluidic phenomena are shown over others in microfluidic systems, which affect the fabrication and operation principles of microfluidic devices. Thus, a brief understanding towards these phenomena is critical to my project. The dominating effects utilized in my project include laminar flow, diffusion and surface tension.

The fluid flows usually have two regimes, laminar and turbulent. Laminar flow, sometimes known as streamline flow, occurs when a fluid flows in parallel layers, with no disruption between the layers [3]. In laminar flows, the velocity of a fluid element is not a random function of time, while in turbulent flows, the movement of fluid is usually chaotic and unpredictable. Reynolds number (Re) is a dimensionless number used to describe the flow regimes, which is determined by

$$\mathrm{Re} = \frac{\rho \upsilon D_h}{\mu} \tag{1.1}$$

where ρ is the density of fluid, ν is the characteristic velocity of the fluid, μ is the fluid viscosity, and D_h is the hydraulic diameter. For a channel with rectangular cross-section,

$$D_h = \frac{2}{\left(\frac{1}{L} + \frac{1}{W}\right)} \tag{1.2}$$

Typically, when the Reynolds number of a flow is smaller than 2300, the flow is considered a laminar flow. Since the Reynolds number is proportional to the hydraulic diameter and thus proportional to (L×W)/(L+W) , when the characteristic dimensions of a fluidic system are small, the Reynolds number will be small and the flow in this system is generally laminar.

Laminar flow has important features. For example, two or more laminar flow streams in contact with each other will exchange materials only by diffusion at the contacting interface. Thus, multiple contacting laminar flows have certain applications, such as fabricating thin membranes in microfluidic channel by interfacial polymerization [4] and collecting/sensing gaseous and aerosolized samples [5]. Another example is generating the packets of fluid with laminar flow or more specifically, slug flow, so as to create stable interface of different phases, such as multi liquid microlenses in microfluidic channel [6,7], microfluidic bubble logic[8], coding/decoding of droplet trains [9], and thin liquid crystal (LC) sensing film, etc.

Since diffusion is the major way for material exchange in laminar flow regime, it is another significant phenomenon in MFS. The relation between the diffusion distance of a particle, d, and the diffusion time, t, is modeled as

$$d = \sqrt{2Dt} \text{ or } t = \frac{d^2}{2D} \qquad (1.3)$$

where D is the diffusion coefficient of the particle. Since d would be very small in an MFS, t is even smaller, thus diffusion could be a very efficient material transfer mechanism in an MFS.

Surface tension is another critical physical mechanism in microscale. Surface tension is due to the cohesion between similar molecules at the interface of multi-phases. Since the amount of liquid in an MFS is extremely small, gravity usually won't take significant effect, thus surface tension usually dominates in microscale. Various applications in microfluidic systems have been demonstrated employing surface tension. As an example, Beebe and coworkers utilized surface tension to create virtual walls to control the flow of liquid on microfluidic chips [4, 10-12]. Another example was to employ hydrophilic/hydrophobic interface pining the droplet of water to realized liquid microlens, which could be controlled by various stimulus to tune its focal length [6, 7, 13-15].

1.1.2 Multiphase interfaces in microfluidic systems

Interfaces between multiple phases are significant components in microfluidic systems, which are directly related to the physical phenomena stated above, and have demonstrated various applications. Typical multiphase interfaces include gas/liquid interfaces, interfaces between immiscible liquids, and interfaces between miscible liquid. These interfaces, integrated in microfluidic systems, have versatile applications due to their unique properties, such as large surface area to volume ratio (SAV) and the ability to create extraordinarily smooth surface.

Large SAV ratio of multiphase interfaces in microfluidic systems is due to their small dimensions. Large SAV ratio implies large contact area and short diffusion distance into bulk, thus diffusion-based reaction through these interfaces can be effectively accelerated. This in turn increases sensitivity of sensing tasks performed by the involving microfluidic systems, when these reactions are used for sensing. Examples include a stable two-phase laminar interface created by surface modification of half of the glass wall with OTS, which is then used for the extraction of different concentrations of ephedrine for subsequent gas chromatography [16], and using gas/liquid interfaces to acquire gaseous samples or airborne targets for sensing purpose [17, 18].

The surface tension at the multiphase interfaces in microfluidic systems creates extraordinarily smooth surface in steady state which can be explained by the principle of minimum energy. This smooth surface could generally be better than polished solid materials, thus provides an option for fabricating high-quality optics in microscale. Moreover, the multiphase interface is tunable by essentially controlling the pressure difference between the interacting phases or surface status of the interface (e.g. contact angle of liquid droplets on a substrate). The optical elements formed with multiphase interfaces thus have capabilities such as tunable focal lengths. Tunable microlenses have been demonstrated at oil-water or air-water interfaces. These microlenses are tunable by the actuation of stimuli-responsive hydrogel rings [13] or posts [14], as shown in Figure 1-2 The liquid lenses can also be controlled pneumatically [6, 7].

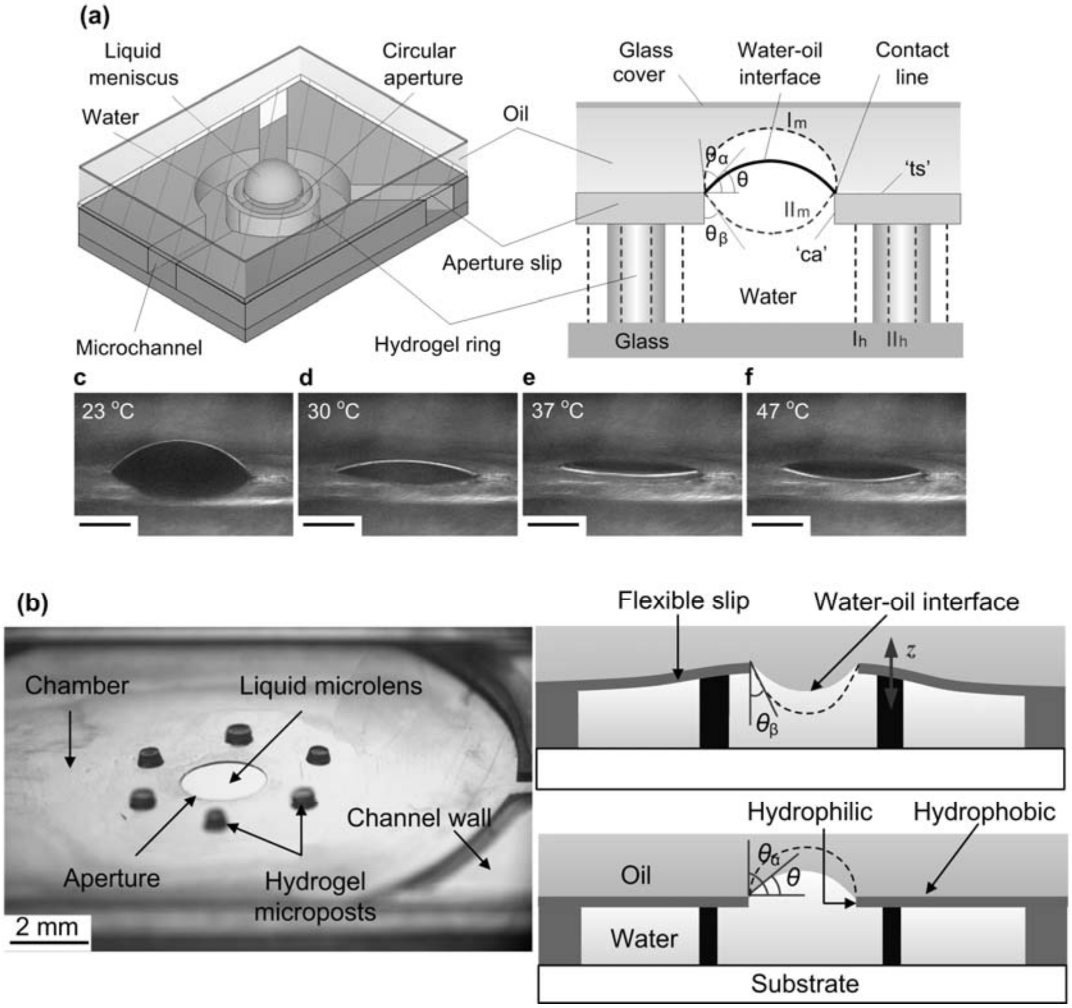

Figure 1-2 (a) Smart microlens using a pinned liquid-liquid interface actuated by a stimuli-responsive hydrogel ring [13]. (b) Microlens formed by an oil-water interface which is pinned at a orifice in a flexible slip. Stimuli-responsive hydrogel posts are used to actuate the slip, thus to change the curvature of the interface [14].

Controllable multiphase interfaces in MFSs are usually created through the boundary of two immiscible liquids [13, 14] and adjusting the wettability of the substrate [5, 6] while considering the geometry of the microchannels. By doing so, the contact angle of certain liquid on a substrate can be confined and thus the shape of the liquid /air interface can be determined.

1.1.3 Applications and components of microfluidic systems

Numerous applications have already been demonstrated by microfluidic systems, in multiple fields such as chemistry: chemical synthesis [19, 20], physics: controlled mixing system [21-23] and biology: gene chips [24-28]. Furthermore, as stated above, microfluidic environments provide unique advantages, for instances, large SAV, short diffusion distance, smooth surface created by surface tension and the possibility to precisely handle small amount of chemical or biological reagents. Chemical and biological sensing and analysis is thus a major application of lab-on-a-chip microfluidic systems, especially for in-field test for toxic materials and other defense and homeland security applications [29-34]. Another interesting application for microfluidic systems (or optofluidic systems, in this case,) is optics. In addition to the microlenses described in section 1.1.2, more liquid optics are demonstrated by microfluidic systems, such as liquid mirrors [18] and tunable liquid lenses [35, 36]. Drug delivery is another promising field in utilizing microfludics. Microfluidic systems for drug delivery are reviewed intensively by Robert Langer [37]. In these microchips, drug delivery is realized by controllable hydrogel [38, 39], and controllable hydrogel arrays combined with valves [40].

From above, we see that sensing and actuating (or more precisely, sample collecting and delivery) are the two major functions performed by an analytical microfluidic system. As described in section 1.1.2., multiphase interfaces usually serve as the substrate or transducer for sensing purposes. Other “building blocks” to be integrated into an MFS to enable and enhance the sensing performance include active-assembly components [41], filters [42-44], and reactors [45]. For the actuating perspective, sample collecting and delivery is generally enabled by bulk fluid controlled by micromixers and micropumps [46, 47], and valves [48, 49].

Microvalves utilizing different actuating mechanisms have been designed and prototyped. One important control mechanism for the valves is through pneumatics. Pneumatically driven microvalves is also demonstrated to be a promising candidate to be integrated onto LoC systems and exhibits promising advantages, such as small dead volumes, complete sealing, and high controllability (linear driving force) [50, 51]. Another prevailing method for microfluidic valve is to use elastic, stimuli-responsive materials-different kinds of stimuli hydrogel [52-60]. The actuating mechanisms of such materials including elastic force from hydrogel swelling (Beebe and coworkers) [58], configuration change (swelling and shrinking) of a hydrogel post embedded in a microfabricated valve structure (Ziaie and coworkers) [61] and the responses of a phenylboronicacid-based hydrogel towards changes in the glucose and pH concentrations [53]. Other mechanisms, such as piezoelectrically actuated materials are also utilized for microvalves [62, 63].

Micromixers and micropumps serve as the “hearts” of microfluidic systems, which is critical to sample acquisition and handling. The subcategories of micropumps include reciprocating displacement, aperiodic displacement, electroosmotic micropumps, and dynamic micropumps based on electrohydrodynamic and magnetohydrodynamic effects [64]. A direct way to fabricate complex and biocompatible pumps which can be integrated into with other microfluidic components is through a multilayer soft lithography process [50, 65]. Actuation mechanisms for micropumps include external magnetic force [23], diaphragms and pistons and using a gear driven by electromagnetic motor [66].

1.2 Photomechanical actuators and their applications in photovoltaic energy harvesting systems

As stated above, sensing and actuating are the major functions of a microfluidic system, or especially, a LoC system. Controlled actuation and manipulation of fluids inside MFSs are also usually prerequisites for creation, sensing and other applications of LoC systems and optofluidics systems. Effective actuation methods include external mechanics (driving fluids with external force, e.g. syringe pumps) [6], micropumps [46, 47], electrical-wetting [3], thermo-mechanical actuation materials (hydrogel) [18] and pH-sensitive actuation materials [13, 14], *etc.*. Since biochemical sensing is a significant application of LoCs and thus certain target phases are sensitive to temperature and pH value, novel actuators to be utilized into LoC systems are always of interest. Among which, we are focused on photomechanical actuators with can be mechanical actuated by light, thus can be considered as a promising candidate of next-generation actuators due to its bio-compatibility and remote-controllability.

1.2.1 Photomechanical actuators and liquid crystal elastomers

Actuators are essential components in not only microfluidic systems, but also in other micro-electro-mechanical systems (MEMS) or micro-opto-mechanical systems (MOMS). Actuator materials have the ability to change their physical dimensions in response to external stimuli and transfer various forms of energy into mechanical work. Depending on their corresponding energy supplies, they can be classified into electrical, thermal, pneumatic and optical actuators [67]. Comparing to electrically driven, optical actuation offers an alternative way to couple energy into actuator structures, which demonstrate distinctive advantages such as wireless actuation, remote controllability, electromechanical decoupling, low noise, elimination of electrical circuits and higher-level integrity. In particular, micro/nano-mechanical devices at the molecular level will most likely be powered by light or electromagnetic radiations [68, 69]. Unfortunately, there are only a few material systems exhibiting photomechanical properties. Materials undergo mechanical deformations in response to light due to the photostriction [70, 71], polarization [72-74], charge effect [75, 76], and radioactive forces on microstructures [77]. Optical triggering of shape memory actuation was also reported for optical actuation [78]. However, these approaches may suffer either from the low actuation strokes, the need for special light sources, low speed, or from the lack of reversibility.

Another way to achieve photomechanical actuation is through opto-thermo-mechanical coupling [79, 80]. This indirect transduction mechanism, however, sometimes process higher efficiency, larger actuation strains, and reversibility. Nematic liquid crystal elastomers (LCEs) [81] have proven to be a truly equilibrium reversible actuating system which can return to the equilibrium shape once the stimulus is removed. They possess several important features that lead to promising new actuation materials [82-88] such as orientational order exhibited by the mesogenic units in amorphous soft materials, topological constraints via the crosslinks, and responsive molecular shape due to the coupling between the orientational order and mechanical strain [81]. Nematic LCEs can thus dramatically and reversibly contract or elongate in response to temperature change.

The response of a polymer to an external stimulus can be modified and improved when incorporated with different materials that impart new physical response, thus refining the actuation performance. Carbon nanotubes (CNTs) are one of the effective filling materials for nanocomposites due to their one-dimension structures, nanometrescale diameters, high aspect ratios, large surface areas, and excellent conductivities and other physical and mechanical properties [89-91]. CNTs, especially the single-wall carbon nanotubes (SWCNTs), show strong absorptions in the visible and near-IR region owing to band gap transitions [92]. Thus, by incorporating CNTs and polymer phase actuators, novel photomechanical actuators can possibly be developed.

1.2.2 Applications of photomechanical actuators in energy harvesting and artificial heliotropism

Energy harvesting is the process by which energy is derived from external sources (e.g., solar power, thermal energy, wind energy, salinity gradients, and kinetic energy), captured, and stored for various applications consuming energy. One novel yet promising application for energy harvesting is to provide the power to small autonomous sensors/actuators incorporated in MEMS or MFS, which are often small and consume little power. Scavenging energy from light, wind, heat or even ambient vibrations could enable these systems to be functional “indefinitely”. Energy harvesting can utilize various mechanisms, such as ambient-radiation energy harvesting [93], biomechanical harvesting [94], piezoelectric energy harvesting [95] and photovoltaic harvesting [96-104].

As a renewable clean energy source, photovoltaic harvesting converts solar energy to electric power [96]. Research and development effort to increase the output from photovoltaic harvesting system mostly focuses on several aspects, such as enhancing the solar-to-electric conversion efficiency [97-99] and using the concentrators by increasing the available solar radiation onto the solar cell surface [100-104]. Another interesting method is artificial heliotropism, similar to solar tracking, which utilizes actuators to enhancing output of photovoltaic systems, by tilting solar panels towards the solar illumination direction in real-time. Partially due to the lack of proper photomechanical actuators, current man-made systems for full-range solar tracking are generally realized through mechatronic designs, thus actuators utilized are electro-motors (active tracking), materials (usually Freon) exhibiting large thermal expansion and shape memory alloys (passive tracking) [105]. Though this method is self-contained (i.e. it's compatible with enhancing of the conversion efficiency and utilizing the concentrators) the complicated actuator system needed in these designs for solar tracking and the resultant high cost are of concern. Further, the power consumption by the electro-mechanical systems themselves to realize solar tracking might negate the gain. Thus, enhancement of photovoltaic systems by novel photomechanical actuators through artificial heliotropism is still a field that needs intensively exploring and exploiting. In this sense, instead of directly using the photomechanical actuators described in section 1.2.1 into MFSs, we decided to utilize them in a photovoltaic energy harvesting system first, as a test and demonstration of their potential in micro systems.

1.3 Fabrication methods

1.3.1 Microfluidic tectonics (μFT)

In order to *in-situ* incorporate different modules and components of a microfluidic system onto a common substrate (e.g. glass) in a simple and compatible process, an efficient and sophisticated fabrication standard process or platform is needed. Such components of MFSs include multiphase interfaces for sample acquisition/handling (e. g. liquid/air interfaces for aerosolized sample collection [5]), the sensing elements (such as LC thin films for biochemical sensing [106]) and the detection elements (such as electrodes, optical fibers or microlenses for performance enhancement [6]). This fabrication platform should thus support *in-situ* fabrication of stimuli-responsive and structural polymers, as well as fabrication/integration of metal/glass microstructures. Microfluidic tectonics (μFT) [107] is demonstrated to be such a promising platform with the capability to be integrated with microelectromechanical systems (MEMS) technology to accommodate these requirements in a relatively simple fashion [13-15, 23, 107, 108].

μFT is compatible with the liquid-phase photopolymerization (LP^3) technology which enables a rapid, simple and low-cost creation of micro components [44, 108]. Similar to the conventional lithography approaches, the LP^3 approach basically starts from a pre-polymer liquid consisting of a monomer (the bulk material or the “bricks” of the structure), a cross-linker (the “adhesive” between the monomer) and a photo-initiator (which absorbs the photo-energy to enable the crosslinking). Thus, exposure to UV initializes the cross-linking process of the prepolymer to form a polymer. The unpolymerized pre-polymer liquid can be developed with a solvent like ethanol, leaving behind the polymer microstructure on the device [109].

Unlike the conventional photolithography technology, which spins/casts photosensitive materials on entire substrates, LP^3 can be conducted at designated areas filled with liquid-phase pre-polymer, thus is more controllable. LP^3 has other advantages such as low temperature (less than 100 °C), simple (minimal clean room usage) and time-efficient (in the range of tens to hundreds of second). Additionally, though μFT alone also have its inherent problems, it's able to merge it with LP^3 and conventional MEMS processes, thus taking the advantage of the three different fabrication approaches/platforms. For example, μFT combined with LP^3 offers a wider variety of bio-compatible materials to work with, including PDMS and responsive hydrogels. As a demonstration, programmable autonomous micromixers, micropumps [110, 111], cooling system [112], tunable liquid microlenses [6, 7] and LC sensing systems [106] have been realized by this merge.

1.3.2 Other fabrication methods

Other fabrication methods included in this report of studies include interfacial fabrication, surface micromachining and conventional macro-scale machining.

Interfacial fabrication utilizes reactions or interactions between two immiscible phases (usually an organic and aqueous solution) to form a membrane inside microchannel [4, 113]. As an important *in situ* fabrication method, it generally starts from define boundaries between hydrophilic and hydrophobic areas on the channel surfaces. The methods to define the boundaries include chemistry treatment with microfluidic patterning (e.g. using laminar flows of octadecyl trichlorosilane (OTS) [11, 12]), or patterning a pre-deposited metal layer, which can be treated hydrophobic, on the substrates [114-116]. In the following chapters of this report, the definition of interfacial fabrication could be extended to: using a laminar aqueous flow to interact with another immiscible phase (e.g. liquid crystal) to create an interface for sensing.

Surface micromachining, as a standard process for fabrication of traditional MEMS systems, generally builds microstructures by deposition and etching of different structural layers on top of the substrate [117]. Our micromachining starts with a glass substrate and deposit layers of metal or other materials on the top. Patterns are defined by photolithography, and transferred by either a wet etch involving an acid or a dry etch involving an ionized gas, and/or plasma. Though modern integrated circuit fabrication using this technique can use dozens of layers, approaching 100, our micromachining is much simpler with maximum 10 layers. Surface micromachining is a relatively sophisticated fabrication technology with long-time standardization. It has certain advantages such as high precision and accuracy and compatible to microelectronics fabrication processes.

For system parts with a dimension of several millimeters to hundreds of millimeters, conventional machining with drills, mills and lathes is utilized. These sophisticated fabrication tools are accurate enough and easy to control for some systems. For processing of materials with great hardness, such as glass, diamond bits are utilized, while for processing with metals and polymers, standard steel bits are used.

1.4 Chapter overview

In this work, 3 different analytical microfluidic/optofluidic systems are first presented, each of which can be considered as an important component of a whole LoC system. By designing and implementing those analytical microfluidic/optofluidic systems, different applications were demonstrated, from aerosolized sample collecting by air-liquid interface, to biochemical sensing by liquid crystal-aqueous phase interface, then to fluorescence signal enhancement by tunable microlenses array. Then a novel liquid-crystal-elastomer opto-thermo-mechanical actuator which responses to broadband white light is investigated and characterized. Instead of immediately integrate it into MFSs, its application in an artificial heliotropism photovoltaic energy harvesting system was first demonstrated. The principle of operation, fabrication and testing of these actuators and systems are described.

Chapter 2 [5] focuses on the creation of gas-liquid interfaces with large SAV ratio in microfluidic structures so that they can be used for collection of gaseous and aerosolized samples. Two structures are demonstrated. In one structure, hydrophobic/hydrophilic boundaries created a channel of liquid confined by gas/liquid interfaces in which analytes were collected, similar to the "virtual walls" method. In another structure, circular air pillars within microfluidic channels were created by surface tension for analytes collection. The former structure has the capability to be simply stacked so as to form a multi-leveled structure, enabling it to collect and separate multiple analytes at a time. The sample acquisition capabilities of the devices were demonstrated by extensive testing with gaseous NH_3 using Nessler's Reagent as the collecting fluidic stream, and with aerosolized Kool-Aid® particles using de-ionized (DI) water as the collecting fluidic stream. Real-time analysis potential was also demonstrated.

In Chapter 3 [106], design and *in situ* realization of a LoC system employing LC thin film for biochemical sensing has been demonstrated. Shear forces generated by the laminar flow of aqueous liquid within a microfluidic channel are utilized to create liquid crystal thin films/ aqueous phase interfaces stabilized within microfabricated structures, which is an autonomous and highly reproducible method to create uniform LC thin film on treated substrate. With the formation of a high quality LC thin film, the orientational response of the LC thin films to targeted analytes in aqueous phases at the autonomous formed interface was thus transduced to and amplified by the optical birefringence of the LC thin films. The biochemical sensing ability of the sensing devices was demonstrated through experiments employing two chemical systems: dodecyl trimethylammonium bromide (DTAB) dissolved in aqueous solution, and the hydrolysis of phospholipids by the enzyme phospholipase A_2 (PLA_2).

Chapter 4 [6] focuses on *in situ* formed tunable liquid microlenses and their applications for dynamic lab-on-a-chip applications, such as enhancing fluorescence emission in laminar fluid flows. The de-ionized water microlenses are intrinsically formed via air-liquid interfaces of liquid droplets, whose positions are precisely controlled by air/liquid injection and pinned at T-shaped junctions of octadecyltrichlorosilane(OTS) treated polymerized isobornyl acrylate [poly(IBA)] microchannels. By pneumatic manipulation inside the channel, the microlenses can be separately tuned in focal lengths along the microchannels parallel to the substrate. Then via the tunable microlenses, excitation light is dynamically focused onto fluorescent fluidic samples, and thus the fluorescence emission signal for detection is significantly increased compared to the case without the microlenses, as a result of the enhancement of the fluorescence excitation. A simulation regarding the surface geometry of the microlenses in the channel is developed, as well as a ray-tracing model regarding the shape and properties of the liquid lenses.

In Chapter 5 [118], we present a novel single-wall carbon nanotube (SWCNT) incorporated liquid crystal elastomer (LCE) nanocomposites that demonstrate strong, reversible photo-actuation. The matrix nematic LCE material possesses reversible thermal deformation, while SWCNTs perform photothermal energy conversion and local heat dissipation upon irradiation.

The resultant SWCNT–LCE nanocomposites exhibit effective photoactuation not only by infrared (IR) irradiation, but also white light with an intensity on the order of 100 mW/cm^2. Rapid and reversible photo-induced strain was observed. The nanocomposite films contracted up to one third of the original length in several seconds under the irradiation of white light, and recovered to the original length in several seconds after the light source was switched off. Moreover, the nematic–isotropic transition temperatures of the SWCNT-LCE nanocomposites were evidently lower than that of the blank LCE by up to 19° C.

Chapter 6 [119] describes an enhancement by adding an "artificial heliotropism" feature into a conventional photovoltaic energy harvesting system utilizing the SWCNT/LCE actuator described in chapter 5. Heliotropism, or conventionally known as solar tracking, is an intriguing attribute possessed by some plants whose leaves or flowers can follow the sun for increased light interception. Inspired by nature, we have demonstrated prototype devices that can self-adaptively track the movements of the sun to significantly enhance the photocurrent output of solar cells. Utilizing the SWCNT-LCE actuators for efficient opto-thermal-mechanical coupling, our mechanism of artificial heliotropism is realized via direct photomechanical response of the actuators to the sunlight, eliminating the need for complicated electro-mechanical system and additional energy consumption. Our prototype devices showed full-range artificial heliotropism and as a result, large increase in photocurrent output from solar cells, in both laboratory and in-field tests.

Chapter 7 summarizes the conclusion of the studies and provides insight into possible future works.

1.5 References

[1] G.M. Whitesides, *Nature*, vol. 442, pp. 368-373 (2006).

[2] Y. Fainman, and P. Demetri, *McGraw Hill Professional*, 2009.

[3] D. Psaltis, S. R. Quake, and C. Yang, *Nature*, vol. 442, pp.381-386 (2006).

[4] B. Zhao, N.O.L. Viernes, J.S. Moore, and D.J. Beebe, *Journal of the American Chemical Society*, vol. 124, pp. 5284-5285 (2002).

[5] J. Greenwood*, Y. Liu*, D. Busacker, D. Cheng and H. Jiang, *IEEE Sensors Journal,* vol. 10, pp. 952-959 (2010). *-equal contribution.

[6] Y. Liu, B. Aldalai, and H. Jiang, *IOP Journal of Micromechanics and Microengineering*, in press.

[7] L. Dong and H. Jiang, *IEEE/ASME Journal of Microelectromechanical Systems,* vol. 17, pp. 381-392 (2008).

[8] M. Prakash and N. Gershenfeld, “Microfluidic bubble logic,” *Science*, vol. 315, pp. 832-835 (2007).

[9] M. J. Fuerstman, P. Garstecki, and G. M. Whitesides, *Science*, vol. 315, pp. 828-832 (2007).

[10] J. Atencia and D. J. Beebe, *Nature*, vol. 437, pp. 648-655 (2005).

[11] B. Zhao, J. S. Moore, and D. J. Beebe, *Science*, vol. 291, pp. 1023-1026 (2001).

[12] B. Zhao, J. S. Moore, and D. J. Beebe, *Analytical Chemistry,* vol. 74, pp. 4259-4268 (2002).

[13] L. Dong, A.K. Agarwal, D.J. Beebe, and H.R. Jiang, *Nature*, vol. 442, pp. 551-554 (2006).

[14] L. Dong and H. R. Jiang, *Applied Physics Letters*, vol. 89, pp. 211120 (2006).

[15] L. Dong, A.K. Agarwal, D.J. Beebe, and H.R. Jiang, *Advanced Materials*, vol. 19, pp. 401-405 (2007).

[16] H. Xiao, D. Liang, G.C. Liu, M. Guo, W.L. Xing, and J. Cheng, *Lab on a Chip*, vol. 6, pp. 1067-1072 (2006).

[17] S.S. Sridharamurthy and H. Jiang, *IEEE Sensors Journal*, vol. 7, pp. 1315-1316 (2007).

[18] X. Zeng and H. Jiang, *Applied Physics Letters*, vol. 93, 151101 (2008)

[19] M. Kakuta, F.G. Bessoth, and A. Manz, *Chemical Record,* vol. 1, pp. 395-405 (2001).

[20] A.J. deMello, “Control and detection of chemical reactions in microfluidic systems,” *Nature*, vol. 442, pp. 394-402 (2006).

[21] M.R. Bringer, C.J. Gerdts, H. Song, J.D. Tice, and R.F. Ismagilov, *Philosophical Transactions of the Royal Society of London Series a-Mathematical Physical and Engineering Sciences*, vol. 362, pp. 1087-1104 (2004).

[22] H. Song and R.F. Ismagilov, *Journal of the American Chemical Society*, vol. 125, pp. 14613-14619 (2003).

[23] A.K. Agarwal, S.S. Sridharamurthy, D.J. Beebe, and H.R. Jiang, *IEEE/ASME Journal of Microelectromechanical Systems*, vol. 14, pp. 1409-1421 (2005).

[24] A.T. Wooley and R.A. Mathies, *Proceedings of the National Academy of Sciences, USA,* vol. 1994, pp. 11348-11352 (1994).

[25] M. Burns, C. Mastrangelo, T. Sammarco, F. Man, J. Webster, B. Johnson, B. Foerster, D. Jones, Y. Fields, A. Kaiser, and D. Burke, *Proceedings of the National Academy of Sciences, USA,* vol. 93, pp. 5556-5561 (1996).

[26] M.U. Kopp, A.J. deMello, and A. Manz, *Science*, vol. 280, pp. 1046–1049 (1998).

[27] Z. Ronai, C. Barta, M. Sasvari-Szekely, and A. Guttman, *Electrophoresis*, vol. 22, pp. 294-299 (2001).

[28] J. Khandurina, T.E. McKnight, S.C. Jacobson, L.C. Waters, R.S. Foote, and J.M. Ramsey, *Analytical Chemistry,* vol. 72, pp. 2995-3000 (2000).

[29] K. Sato, A. Hibara, M. Tokeshi, H. Hisamoto, and T. Kitamori, *Advanced Drug Delivery Reviews*, vol. 55, pp. 379-391 (2003).

[30] M. Tokeshi, T. Minagawa, K. Uchiyama, A. Hibara, K. Sato, H. Hisamoto, and T. Kitamori, *Analytical Chemistry*, vol. 74, pp. 1565-1571 (2002).

[31] R.M. Atlas, *Current Opinion in Biotechnology*, vol. 16, pp. 239-242 (2005).

[32] M.A. Hamburg, *Trends in Biotechnology*, vol. 20, pp. 296-298 (2002).

[33] N.J. Mantis, *Advanced Drug Delivery Reviews*, vol. 57, pp. 1424-1439 (2005).

[34] C. Haber, *Lab on a Chip*, vol. 6, pp. 1118-1121 (2006).

[35] D. Zhang, V. Lien, Y. Berdichevsky, J. Choi, and Y.-H. Lo, *Applied Physics Letters*, vol. 82, pp. 3171-3172 (2003).

[36] S. Kuiper and B.H.W. Hendriks, *Applied Physics Letters*, vol. 85, pp. 1128-1130 (2004).

[37] J.T. Santini, A. C. Richards, R. Scheidt, M. J. Cima, and R. Langer, *Angewandte Chime*, vol. 39, pp. 2396-2407 (2000).

[38] S. Brahim, D. Narinesingh, and A. Guiseppi-Elie, *Biosensors and Bioelectronics*, vol. 17, pp. 973-981 (2002).

[39] D.T. Eddington and D.J. Beebe. *Advanced Drug Delivery Reviews*, vol. 56, pp. 199-210 (2004).

[40] D.T. Eddington and D.J. Beebe, *IEEE/ASME Journal of Microelectromechanical Systems*, vol. 13(4), pp. 586-593 (2004).

[41] D. Kim, S.K. Mohanty, and D.J. Beebe, *Proceedings of Micro Total Analysis Systems Symposium*, September 26-30, Malmö, Sweden: pp. 36-38 (2004).

[42] B. He, L. Tan, and F. Regnier, *Analytical Chemistry*, vol. 71(7), pp. 1464-1468 (1999).

[43] J. Moorthy and D.J. Beebe, *Lab on a chip*, vol. 3(2), pp. 62-66 (2003).

[44] J. Moorthy, G.A. Mensing, D. Kim, S. Mohanty, D.T. Eddington, W.H. Tepp, E.A. Johnson, and D.J. Beebe, *Electrophoresis*, vol. 25(10-11), pp. 1705-1713 (2004).

[45] J. Gao, J. Xu, L.E. Locascio, and C.S. Lee, *Analytical Chemistry,* vol. 73(11), pp. 2648-2655 (2001).

[46] C.J. Campbell and B.A. Grzybowski, *Philosophical Transactions: Mathematical, Physical and Engineering Sciences*, May 15, vol. 362, pp. 1069-1086 (2004).

[47] N.-T. Nguyen, X. Huang, and T. K. Chuan, *Journal of Fluids Engineering*, vol. 124, pp. 384-392 (2002).

[48] E.T. Lagally, P.C. Simpson, and R.A. Mathies, *Sensors and Actuators B*, vol. 63, pp. 138-146 (2000).

[49] D. Kim and D.J. Beebe, *Sensors and Actuators A: Physical*, vol. 136(1), pp. 426–433 (2007).

[50] M.A. Unger, H.P. Chou, T. Thorsen, A. Scherer, and S.R. Quake, *Science*, vol. 288(5463), pp. 113-116 (2000).

[51] F.K. Balagadde, L.C. You, C.L. Hansen, F.H. Arnold, and S.R. Quake, *Science*, vol. 309(5731), pp. 137-140 (2005).

[52] A. Richter, D. Kuckling, S. Howitz, T. Gehring, and K.F. Arndt, *Journal of Microelectromechanical Systems*, vol. 12(5), pp. 748-753 (2003).

[53] A. Baldi, Y.D. Gu, P.E. Loftness, R.A. Siegel, and B. Ziaie, *Journal of Microelectromechanical Systems*, vol. 12(5), pp. 613-621(2003).

[54] R.H. Liu, Q. Yu, and D.J. Beebe, *Journal of Microelectromechanical Systems,* vol. 11(1), pp. 45-53 (2002).

[55] Q. Yu, J.M. Bauer, J.S. Moore, and D.J. Beebe, *Applied Physics Letters*, vol. 78(17), pp. 2589-2591 (2001).

[56] D.J. Beebe, J.S. Moore, J.M. Bauer, Q. Yu, R.H. Liu, C. Devadoss, and B.H. Jo, *Nature*, vol. 404(6778), pp. 588-590 (2000).

[57] D. Kim and D.J. Beebe, *Lab on a Chip*, vol. 7(2), pp. 193-198 (2007).

[58] D. Kim and D.J. Beebe, S*ensors and Actuators a:Physical*, vol. 136, pp. 426-433 (2007).

[59] D.T. Eddington and D.J. Beebe, *Advanced Drug Delivery Reviews,* vol. 56(2), pp. 199-210 (2004).

[60] D.T. Eddington, R.H. Liu, J.S. Moore, and D.J. Beebe, *Lab on a Chip*, vol. 1(2), pp. 96-99 (2001).

[61] M. Lei, B. Ziaie, E. Nuxoll, K. Ivan, Z. Noszticzius, and R.A. Siegel, *Journal of Nanoscience and Nanotechnology*, vol. 7(3), pp. 780-789 (2007).

[62] E.H. Yang, C. Lee, J. Mueller, and T. George, *IEEE/ASME Journal of Microelectromechanical Systems*, vol. 13(5), pp. 799-807 (2004).

[63] D.C. Roberts, H.Q. Li, J.L. Steyn, O. Yaglioglu, S.M. Spearing, M.A. Schmidt, and N.W. Hagood, *IEEE/ASME Journal of Microelectromechanical Systems*, vol. 12(1), pp. 81-92 (2003).

[64] D.J. Laser and J.G. Santiago, *Journal of Micromechanics and Microengineering*, vol. 14(6), pp. R35-R64 (2004).

[65] H.-P. Chou, M.A. Unger, and S.R. Quake, *Biomedical Microdevice*, vol. 3(4), pp. 323-330 (2001).

[66] J. Dopper, M. Clemens, W. Ehrfeld, S. Jung, K.P. Kamper, and H. Lehr, *Journal of Micromechanics and Microengineering*, vol. 7(3), pp. 230-232 (1997).

[67] G. T. Kovacs, *Micromachined Transducers Sourcebook* , New York: McGraw-Hill, 1998.

[68] V. Balzani, A. Credi, F. M. Raymo and J. F. Stoddart, *Angewandte Chemie International Edition, vol.* 39 pp. 3348 (2000).

[69] T. Hugel, N. B. Holland, A. Cattani, L. Moroder, M. Seitz and H. E. Gaub, *Science,* vol. 296, pp. 1103 (2002).

[70] K. Takagi, S. Kikuchi, J.-F. Li, H. Okamura, R. Watanabe and A. Kawasaki, *Journal of the American Ceramic Society,* vol.87, pp. 1477 (2004).

[71] P. Poosanaas, K. Tonooka and K. Uchino, *Mechatronics,* vol. 10, pp. 467 (2000).

[72] P. Krecmer, A. M. Moulin, R.J. Stephenson, T. Rayment, M. E. Welland and S. R. Elliott, *Science,* vol. 277 pp. 1799 (1997).

[73] H. Finkelmann, E. Nishikawa, G. G. Pereira and M. Warner, *Physical Review Letters,* vol. 87, 015501, (2001).

[74] P. M. Hogan, A. R. Tajbakhsh and E. M. Terentjev, *Physical Review E,* vol. 65, 041720 (2002).

[75] P. G. Datskos, S. Rajic and I. Datskou, *Applied Physics Letters,* vol. 73, pp. 2319 (1998).

[76] J. Suski, D. Largeau, A. Steyer, F. C. Van and F. R. Blom, *Sensors Actuators A,* vol. 24, pp. 221 (1990).

[77] M. Sulfridge, T. Saif, N. Miller and K. Ohara, *IEEE/ASME Journal of Microelectromechanical Systems*, vol. 11, pp. 574 (2002).

[78] H. Koerner, G. Price, N. A. Pearce, M. Alexander and R. A. Vaia, *Nature Materials,* vol. 3, pp. 115 (2004).

[79] B. E. Jones and J. S. McKenzie, *Sensors Actuators A,* vol. 37/38, pp. 202-207 (1993).

[80] J. M. Zanardi *et. al., Microelectronic Engineering,* vol. 73/74, pp. 429 (2004).

[81] M. Warner and E. M. Terentjev, *Liquid Crystal Elastomers,* Oxford University Press, Oxford, 2003.

[82] J. Kupfer and H. Finkelmann, *Makromolekulare Chemie, Rapid Communications,* vol. 12, pp.717-726 (1991).

[83] H. Finkelmann, E. Nishikawa, G. G. Pereira and M. Warner, *Physical Review Letters*, vol. 87, 015501 (2001).

[84] Y. L. Yu, M. Nakano and T. Ikeda, *Nature*, vol. 425, pp. 145 (2003).

[85] M. Camacho-Lopez, H. Finkelmann, P. Palffy-Muhoray and M. Shelley, *Nature Materials,* vol. 3, pp. 307-310 (2004).

[86] M. Yamada, M. Kondo, J. I. Mamiya, Y. L. Yu, M. Kinoshita, C. Barrett and T. Ikeda, *Angewandte Chemie International Edition*, vol. 47, pp. 4986-4988 (2008).

[87] S. Xu, H. W. Ren, Y. J. Lin, M. G. J. Moharam, S. T. Wu and N. Tabiryan, *Optics Express*, vol. 17, pp. 17590-17595 (2009).

[88] F. T. Cheng, R. Y. Yin, Y. Y. Zhang, C. C. Yen and Y. L. Yu, *Soft Matter*, vol. 6, pp. 3447-3449 (2010).

[89] S. Iijima, *Nature*, vol. 354, pp. 56–58 (1991).

[90] S. N. Kim, J. F. Rusling and F. Papadimitrakopoulos, *Advanced Materials,* vol. 19, pp. 3214–3228 (2007).

[91] W. Y. Zhou, X. D. Bai, E. G. Wang and S. S. Xie, *Advanced Materials,* vol. 21, pp. 4565–4583 (2009).

[92] M. A. Hamon, M. E. Itkis, S. Niyogi, T. Alvaraez, C. Kuper, M. Menon and R. C. Haddon*, Journal of the American Chemical Society,* vol. 123, pp. 11292–11293 (2001).

[93] J.A. Paradiso, "Energy scavenging for mobile and wireless electronics", *IEEE Pervasive Computing Magazine*, vol. 1, pp. 18-27 (2005).

[94] J. M. Donelan, Q. Li, V. Naing, J. A. Hoffer, D. J. Weber and A. D. Kuo, *Science*, vol. 319(5864), pp. 807-810 (2008).

[95] G.K. Ottman, *IEEE Transactions on Power Electronics*, vol. 17(5), pp. 669 – 676 (2002).

[96] K. W. J. Barnham, M. Mazzer and B. Clive, *Nature Materials*, vol. 5, pp. 161 (2006).

[97] D. Kraemer *et. al.*, *Nature Materials,* vol. 10, pp. 532 (2011).

[98] B. O'Regan, M. Grätzel, *Nature,* vol. 353, pp. 737 (1991).

[99] H.-Y. Chen *et. al.*, *Nature Photonics,* vol. 3, pp. 649 (2009).

[100] K. Araki *et. al.*, *Progress in Photovoltaics: Research and Applications,* vol. 13, pp. 513 (2005).

[101] J. Yoon *et. al.*, *Nature Communications,* vol. 2, pp. 343 (2011).

[102] M. J. Currie, J. K. Mapel, T. D. Heidel, S. Goffri, M. A. Baldo, *Science,* vol. 321, pp. 226 (2008).

[103] M. R. Lee *et. al.*, *Science,* vol. 324, pp. 232 (2009).

[104] J. W. Schwede *et. al.*, *Nature Materials,* vol. 9, pp. 762 (2010).

[105] H. Mousazadeh *et. al.*, *Renewable & Sustainable Energy Reviews,* vol. 13, pp. 1800 (2009).

[106] Y. Liu, D. Cheng, I.-H. Lin, N.L. Abbott, and H. Jiang, *Lab on a Chip*, in press.

[107] D. J. Beebe, J. S. Moore, Q. Yu, R. H. Liu, M. L. Kraft, B. -H. Jo, and C. Devadoss, *Proceedings of the National Academy of Sciences, USA,* vol. 97, pp. 13488-13493 (2000).

[108] A. K. Agarwal, D. J. Beebe, and H. Jiang, *Journal of Micromechanics and Microengineering,* vol. 16, pp. 332–340 (2006).

[109] G.M. Whitesides, *Abstracts of Papers of the American Chemical Society*, vol. 212, pp. 31-Inor (1996).

[110] A.K. Agarwal, S.S. Sridharamurthy, T.M. Pearce, G.A. Mensing, D.J. Beebe, and H. Jiang, P*roceedings of Hilton Head: A Solid State Sensor, Actuator, and Microsystem Workshop*, June 6-10, Hilton Head Island, SC, USA: pp. 121-124 (2004).

[111] A.K. Agarwal, J. Atencia, D.J. Beebe, and H. Jiang, *Proceedings of the 1st International Workshop on Networked Sensing Systems*, June 22-23, Tokyo, Japan: pp. 51-55 (2004).

[112] A.K. Agarwal, S.S. Sridharamurthy, D.J. Beebe, and H. Jiang, *Proceedings of the 13th International Conference on Solid-State Sensors, Actuators, and Microsystems*, June 5-9, Seoul, South Korea (2005).

[113] D. Cheng, Y.P. Choe, and H. Jiang, *Proceedings of IEEE Sensors Conference*, pp. 1044-1047 (2007).

[114] Y.N. Xia, E. Kim, M. Mrksich, and G.M. Whitesides, *Chemistry of Materials*, vol. 8(3), pp. 601-603 (1996).

[115] E. Hoque, J.A. DeRose, P. Hoffmann, B. Bhushan, and H.J. Mathieu, *Journal of Chemical Physics*, vol. 126(11), pp. 114706 (2007).

[116] B.H. Clare and N.L. Abbott, *Langmuir*, vol. 21 (14), pp. 6451-6461 (2005).

[117] Bustillo, J.M.; R.T. Howe and R.S. Muller, *Proceedings of the IEEE,* vol.86(8), pp.1552–1574 (1998).

[118] C. Li*, Y. Liu*, C.-W. Lo, and H. Jiang, *Soft Matter*, vol. 7(16), pp. 7511-7516 (2011). *:equal contribution.

[119] C. Li*, Y. Liu*, X. Huang, H. Jiang, *Advanced Functional Materials*, in press. *: equal contribution (2012).

Chapter 2. Collection of Gaseous and Aerosolized Samples Using Microfluidic Devices with Gas-Liquid Interfaces

(Parts of the contents in this chapter have been published as:

J. Greenwood*, Y. Liu*, D. Busacker, D. Cheng and H. Jiang, "Collection of gaseous and aerosolized samples using microfluidic devices with gas-liquid interfaces," ***IEEE Sensors Journal*****, vol. 10, no .5, pp. 952-959, 2010. *:equal contribution.)**

In this chapter, we demonstrated methods for collecting gaseous samples and aerosolized particles into microfluidic channels. Gas-liquid interfaces created by surface tension permit analytes to transfer from the environment into a microfluidic channel. In one structure of our design, hydrophobic/hydrophilic boundaries created a channel of liquid confined by gas/liquid interfaces in which analytes were collected. In another structure, circular air pillars within microfluidic channels were created by surface tension forces for analytes collection. A multi-leveled structure could be formed by the air pillar design with a simple process, enabling it to collect and separate multiple analytes at a time. Both structures were tested with ammonia as a gaseous sample and Kool-Aid® as aerosolized particles. The sample acquisition capabilities of the devices were demonstrated by extensive testing with gaseous NH_3 using Nessler's Reagent as the collecting fluidic stream, and with aerosolized Kool-Aid® particles using de-ionized (DI) water as the collecting fluidic stream. Increasing the exposed fluidic surface area to the environment effectively increased collection efficiency of the devices. This was confirmed by a resistance study between different sets of designs of both structures. Real-time analysis potential was also demonstrated through measurement of DI water resistance by collecting varying concentrations of gaseous NH_3.

2.1 Introduction

Collection and real-time monitoring of airborne and gaseous samples such as explosives, drugs, dioxins and bacteria have become an important issue for homeland security, air-pollution monitoring, and medical diagnosis [1-3]. Although the substance of interest is usually airborne, analysis of liquid aggregates is the most common method for chemical and biology analysis. As a result, sample to liquid interfacing is demonstrated to be an efficient method of collecting and delivering gaseous samples and aerosolized particles, and also shows the potential to be a part of certain diagnosis systems—for example, to observe ammonia levels in air exhaled by the patient [4], and to be a part of chemical/biological sensors—for example, to acquire toxic bacterial spore particles by dissolving them in a liquid [5]. To enable gas-liquid interactions, capillary action [6] and surface chemistry [1] have been utilized previously. Sridharamurthyet.al. reported an interesting surface-tension-held gas-liquid interface pinned at hydrophilic/hydrophobic polymer/glass interface for sample collection with a relatively simple fabrication process [7]. Although these methods are effective and point out the direction for novel designs, there still exist issues such as requirement of relatively complicated fabrication processes or polymer swelling problems during operation. We previously presented a preliminary study of the method of creating microfluidic channel with gas-liquid interface by hydrophobic self-assembled monolayer (SAM) on gold surfaces [8]. Here, we present an expanded study of such devices (called channel devices) and recently-developed air pillar devices utilizing relatively simple fabrication processes and low cost materials, while showing good collecting performance.

Gas-liquid interfaces can be created using various methods. One prevailing method is to create hydrophobic/hydrophilic interfaces so aqueous liquids can be pinned by surface tension at the interfaces [9][10]. Current processes for creating such hydrophobic/hydrophilic interfaces usually involves the usage of octadecyltrichlorosilane (OTS) to create a SAM on the glass surface [11][12], which is relatively complicated [13]. This complication in hydrophobic surface formation requires additional consideration in device design and fabrication. A previous study of our group has demonstrated that patterned isobornyl acrylate (IBA) is an easier and more efficient way to create the hydrophobic/ hydrophilic boundary [7]. However, IBA might swell when interacting with certain solvents, limiting the lifetime of the devices and introducing uncertainties during their operation.

To overcome this problem, we have demonstrated gas-liquid interface channel devices in which the hydrophilic/hydrophobic interfaces are formed by the self-assembly of alkanethiol monolayers on gold surface, instead of IBA. Comparing to previous devices created by flushing OTS into complicated microfluidic networks [14], our channel devices have simpler fabrication procedures and better compatibility with lab-on-a-chip applications since only gold and glass have been used as the bulk material [Figure 2-1].

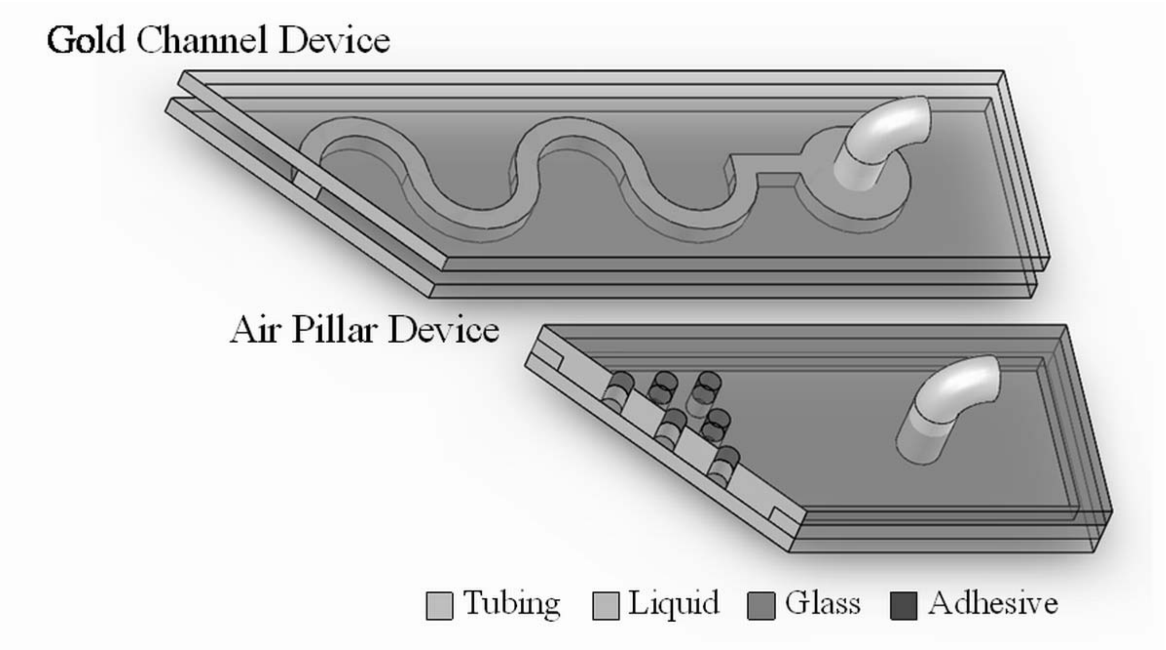

Figure 2-1. 3D rendition of a channel device (top) and an air pillar device (bottom).

The SAM worn-out problem on the device might be a concern for such device. To eliminate the need of SAM and prolong the device shelf life, we reveal an alternative way to form the hydrophilic/hydrophobic interface by constructing air-pillar structures from pre-drilled holes in glass pinning the liquid at interface. For such devices, the fabrication process is straightforward, very low-cost, and showed improvement of robustness and performance over other comparable designs. We also demonstrated multi-level air pillar devices with a relatively simple fabrication process, in which each level could be occupied by a specific collecting liquid stream. This design allows for multiple streams to be simultaneously exposed to the environment. Each stream could potentially contain agents (e.g. antibodies) that specifically bind with one type of gaseous/aerosolized analyte, while other analytes unbound are flushed away. Therefore, this design could realize not only sample collection but also sample constituent separation, and would be of great benefit to high-throughput detection.

2.2 Principles of operation

2.2.1 Formation of hydrophobic-hydrophilic interfaces

Hydrophobic SAM of alkanethiol formed on the surface of a copper or gold layer has been reported [15], [16], and such monolayer hardly forms on a glass surface, which has been further demonstrated in Figure 2-2. Hence, the wettability will change abruptly at the interface of an alkanethiol-treated gold surface and a treated glass surface, thus forming a hydrophobic-hydrophilic boundary. Utilizing this method, two glass slides with patterned gold-coating films and alkanethiol treatment are aligned and stacked "face to face" to form our channel device, as shown in Figure 2-3. The glass slides are separated by adhesive tape spacers by ~60μm at the corners with no confinement at the lateral and transverse directions. When an aqueous liquid is flowed through, the surface tension will balance the pressure difference between the liquid and the atmosphere and pin the lateral surface of the fluid stream at the glass/gold hydrophilic/hydrophobic interface. As a result, the liquid stream is confined in the glass section of the surfaces of the slides by a "wall" of surface tension as long as the pressure difference does not exceed a critical value, and the airborne analytes can enter the device from the lateral direction and be collected dynamically by the fluid stream.

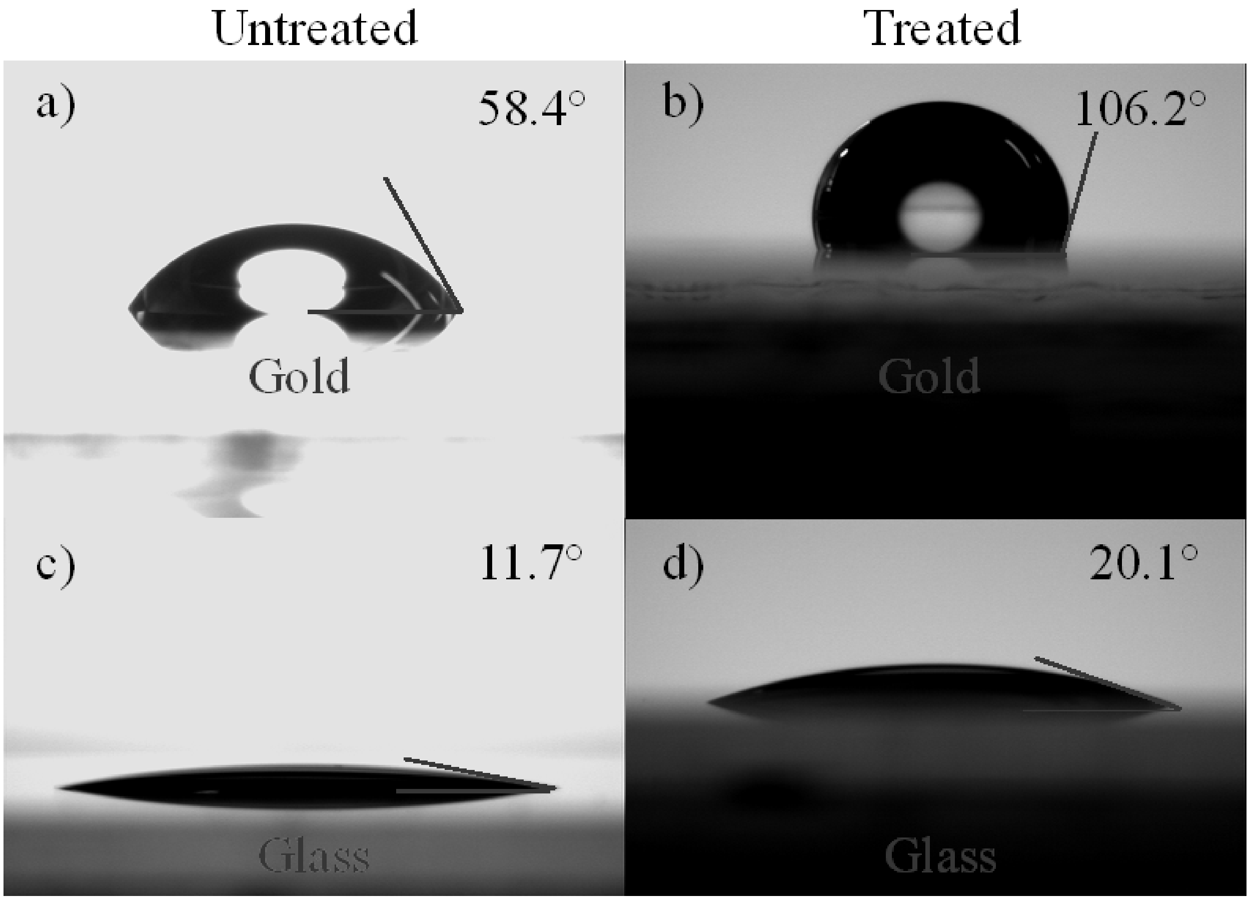

Figure 2-2. Contact angle profile of a droplet on alkanethiol-treated gold (b) and glass slide surfaces (d) with comparison to untreated surfaces (a), (c). The profile pictures are taken with a goniometer.

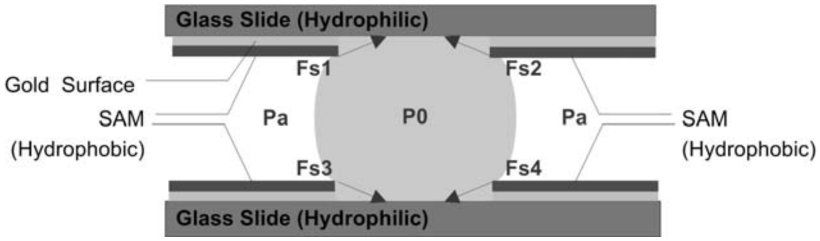

Figure 2-3. Diagram showing the forces involved in the hydrophobic- hydrophilic boundaries. The liquid is held in the channel by the surface tension of the liquid (Fs1, Fs2, Fs3 and Fs4) due to the abrupt wettability change at the Au/glass interface.

2.2.2 Air Pillar Structures for Airborne Analyte Collection

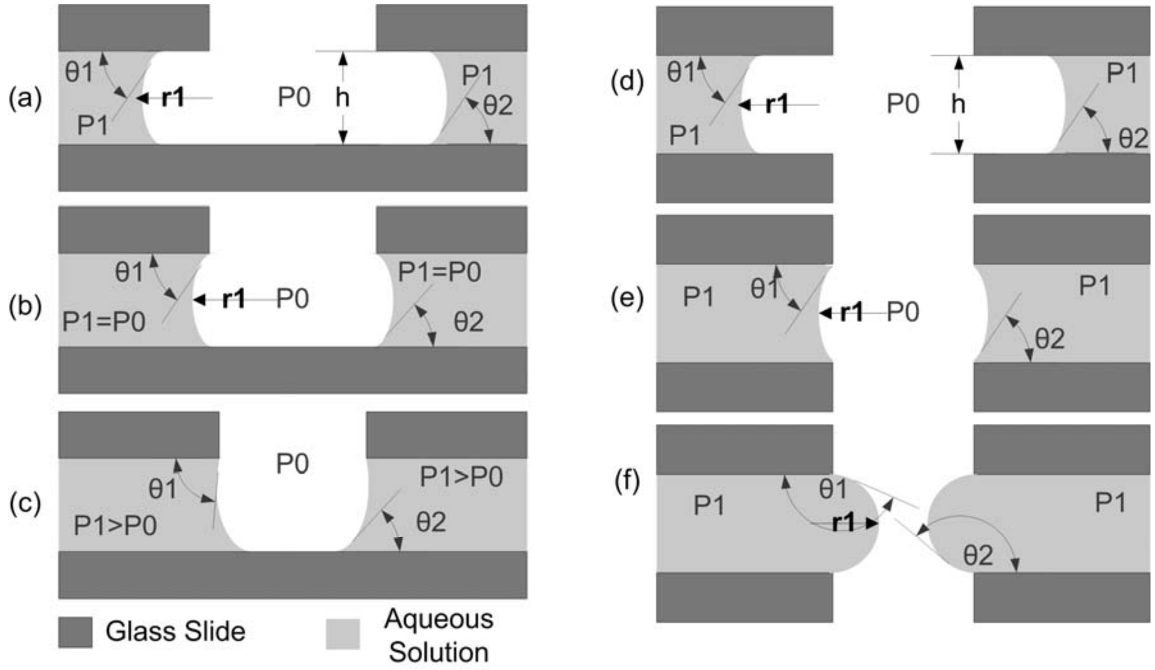

Figure 2-4. (a)-(c) Formation of air pillars with device structure case I, (d)-(f) Formation of air pillars with device structure case II. In (a) and (d), aqueous solution is still in the hydrophilic area; the liquid–air interface will maintain the same shape and move forward until arriving at the hole boundary. The pressure in the aqueous solution remains the same, P1. When the liquid–air interface arrives at the hole, it is pinned by the rough edge [(b) and (e)]. When the pressure of the aqueous solution increases, the interface will assume different shape. In case I, contact angle θ2 still approximately equals to θ hydrophilic, while θ1 can change continuously until the air pillar is filled (c). In case II, both θ1 and θ2 will change because the interface is pinned at both the top and bottom hydrophobic-hydrophilic boundaries, thus changing the meniscus of the liquid–air interface from concave ($r < 0$), to flat ($r = \infty$), and eventually to convex ($r > 0$) (f).

A glass microscope slide with pre-drilled hole-pattern, an inlet and an outlet is stacked on top of another patterned or un-patterned slide to form a single-level air pillar device as shown in Figure 2-1 (bottom), and the transverse and lateral directions are sealed by adhesive tapes. Air pillars can be formed with holes pre-drilled only on the top surface of the channel (i.e. the single level air pillar structure, case I), or with through holes pre-drilled on both the top and bottom of the glass surface (corresponding to one level in a multilevel air pillar device, case II). Figure 2-4 (a)-(c) depict the formation of air pillars in case I, while Figure 2-4 (d)-(f) illustrate the formation of air pillars in case II. In both cases, according to Young-Laplace equation [10], [17], we have:

$$\Delta P = P_1 - P_0 = \gamma_{LG}(\frac{1}{r}+\frac{1}{R}) \qquad \textbf{(1)}$$

where r and R are the radii of curvature in directions vertical and parallel to the liquid stream, and γLG is the surface tension. The dimension along the boundary is much larger than the channel height in our microfluidic devices. Thus, the radius parallel to the liquid stream R approaches ∞, so equation (1) is reduced to (h is the height of the channel):

$$P_1 - P_0 = \frac{\gamma_{LG}}{r}\text{; where } r = \frac{h}{2\cos(180^\circ - \theta_1)}$$

$$\text{Hence, } P - P_0 = \frac{2\gamma_{LG}}{h}\cos(180^\circ - \theta_1) \qquad (2)$$

In both cases, when an aqueous liquid is flowed in the channel [Fig.4 (a), (d)] but has not reached the hole, the liquid–air interface forms a meniscus with a fixed contact angle at the top and bottom surfaces of the channel, θ_1, which is equal to the contact angle formed by a drop of the same aqueous solution on the same hydrophilic glass surface, θhydrophilic [10]. Because in the hydrophilic side of the channel, $\theta_1 < 90^\circ$, r_1 is negative, and P_1 is smaller than P_0. Therefore, the liquid–air interface moves toward the hydrophobic–hydrophilic boundary with a fixed shape of meniscus.

In both cases, after the aqueous liquid arrives at a boundary of a hole, the liquid–air interface is pinned by the rough edge of the hole. In case I, only the top contact line of the interface is pinned, In case II, both contact lines of the liquid–air interface with the top and bottom surfaces of the channel are pinned [Figure 2-4(b), (e)].

In case I, keeping increasing the fluid pressure (by introducing the aqueous solution the channel) has very little affect on the contact angle at the free contact line, θ_2. Since the bottom contact line of the interface is not pinned, the meniscus will always remain concave [Figure 2-4(c)]. In case II, however, increase in the fluid pressure will introduce change in both θ_1 and θ_2 because the interface is pinned at both the top and bottom contact lines, thus changing the meniscus of the liquid–air interface from concave ($r < 0$), to flat ($r = \infty$), and eventually to convex ($r > 0$) [Figure 2-4 (f)]. According to previous study by Cheng et. al. [18], the contact angle between the liquid–air interface and the channel surface, θ, increases from $\theta_{1,2}$ to θ_{max}, where θ_{max} is the maximum contact angle that can be sustained by the boundary. To our observation, θ_{max} is related to both the interfacial energy of the solid surface contacting the aqueous solution and the roughness of the edge. Further increase in the liquid pressure will result in a large pressure difference that breaks the force balance at the pinned surface. As a result, the air pillars will disappear in both cases.

2.3 Device fabrication

2.3.1 Channel device with hydrophobic-hydrophilic interface

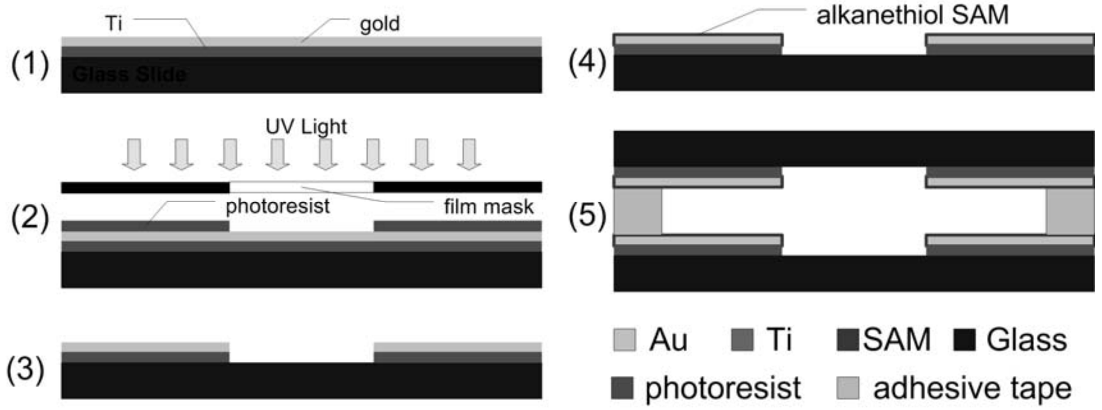

Figure 2-5. Fabrication process of the channel device. 1) Au/Ti coated glass slide. 2) Single mask photolithography to define the geometry of the gas/liquid interface and the channel. 3) Etching Au and Ti, then removing photoresist. 4) SAM surface treatment. 5) Bonding two slides "face to face" together using adhesive tape at each corner of the slides.

As shown in Figure 2-5, microscope slides pre-coated with Ti and Au (50Å and 1000Å, respectively) were obtained from Metal Films Co. Ltd. A single mask photolithography process was then preformed to pattern the Au/Ti film on the glass slide using positive photoresist (AZ4620). The exposed gold layer was removed with gold etchant, and then a short submersion in hydrofluoric acid removed the thin Ti layer, exposing the glass surface. This defined the channel geometry, which in our experiment is serpentine (larger gas/liquid interface area) or straight (smaller area). The process was repeated to obtain another Au/Ti coated microscope slide with an identical pattern. Through holes were drilled into one of the two slides at opposing ends of the channel as the inlet and outlet. Both slides were then placed in a solution of 1mM hexadecanethiol (Acros Organics, Fair Lawn, NJ, USA) diluted with 200ml of ethanol for two hours. They were then rinsed with ethanol and allowed to dry, forming a hydrophobic SAM layer on top of the Au [Figure 2-5 (4)]. Finally, the two slides are aligned and bonded using 60µm thick double sided adhesive tape (3M, St. Paul, MN, USA), forming the final device.

2.3.2 Single- and multi-level air pillar device

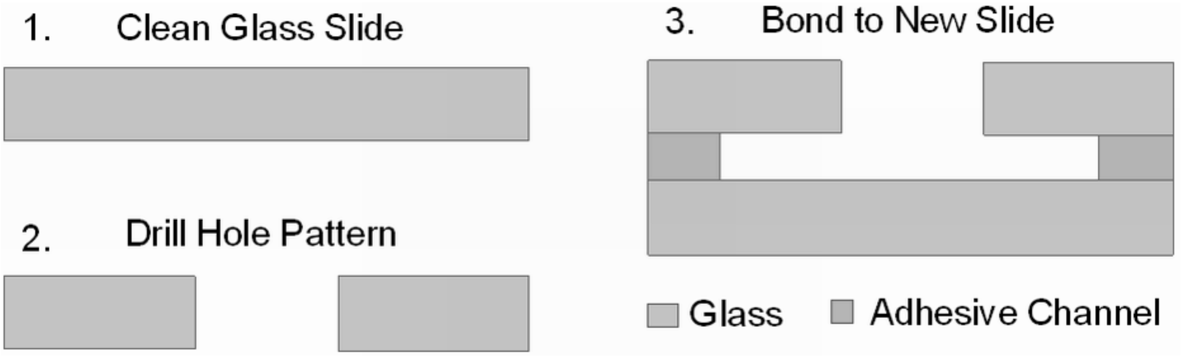

Figure 2-6. Fabrication of a multi-level air pillar device. 1) Inspect glass slides for defects. 2) Drill aligned hole-patterns in glass slides. 3) Stack, align and bond hole-patterned glass slides to a new clean slide using double sided adhesive tape to create the device.

For a single level air pillar device, through holes are drilled on the top glass microscope slide, forming a specific hole-pattern. Inlet and outlet holes were drilled on opposing ends of the pattern and connected with ethyl vinyl acetate microbore tubing. The patterned slide was bonded to another clean microscope slide (hole-patterned or not patterned) using double sided adhesive tape of a desired thickness (3M, St. Paul, MN, USA), forming a channel.

For a multi-level air pillar device, an identical through-hole pattern was drilled into two or more slides. Inlet and outlet holes were drilled at arbitrary locations on opposing ends of each hole-patterned slide. Tubing was inserted for open access to each level. The patterned slides were aligned vertically and bonded to another clean microscope slide using double sided adhesive tape with a desired thickness (3M, St. Paul, MN, USA) forming channels at each level [Figure 2-6].

2.4 Design considerations

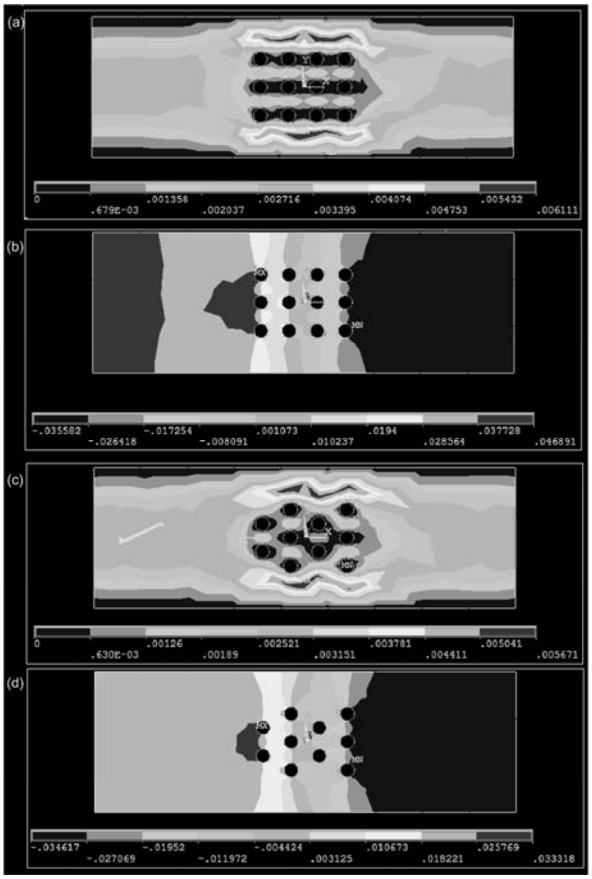

Figure 2-7. Flow rate and pressure simulations of different air pillar hole-patterns using Ansys®. a) Flow rate profile of an aligned "holes matrix" pattern. b) Pressure profile on an aligned "holes matrix" pattern. c) Flow rate profile of on an offsetting holes pattern. d) Pressure profile on an offsetting holes pattern. The aqueous fluid (water) flows in the device with a velocity of 3mm/s from the left edge of the layer and flows out from the right edge with a velocity of -3mm/s, and the fluid velocity at the lateral walls are set to 0; fluid velocity components in directions normal to the circumferences of the air-pillar openings are also set to 0. Pressures at the openings are all set to be equal to a standard air pressure.

For air pillar devices, different hole-patterns were considered before the final layout was chosen. Figure 2-7 shows the flow and pressure analysis of two different layout methods: aligned “hole matrix” [Fig.7 (a), (b)] and offsetting hole arrays [Fig.7 (c),(d)]. The simulation creates a simplified 2-D model for the collecting fluid level with air pillars with exactly the same dimensions as the device. We use FLUID141 (2-D fluid-thermal) as the element type for modeling with ANSYS® (ANSYS Inc. Canonsburg, PA 15317, USA). The property of the fluid material is set according to the properties of de-ionized water [i.e. density= 1 kg/m^3, dynamic viscosity= 1.002×10^{-3} (N*s/m^2), kinematic viscosity=1.004×10-6 (m^2/s)]. The environmental air pressure is set to 1 atm. The environmental temperature is set to be 300K. The boundary conditions are applied as follows: 1) The aqueous fluid (water) flows into the device with a velocity of 3mm/s (left edge) and flows out of the device (right edge) with a velocity of 3mm/s while the fluid velocity at the lateral walls (top and bottom edges) are set to 0mm/s; 2) Pressures at the air pillar openings are all set to 1 atm.; 3). The fluid velocity components normal to the air pillar opening circumferences are all set to zero. Figure 2-7(a) and (c) show the solved flow rate profiles for devices with different hole-patterns while Figure 2-7(b) and (d) show the solved pressure profiles. The color bar under the 2D model shows the scale of the relative physical quantities.

Fig.7 (a), (b) shows that higher flow rates can be achieved in the channel with the aligned air pillar design. This would allow higher collection rates and rapid flushing of the system for subsequent experiments. A major disadvantage of this design is the dead spots [dark blue area in Fig.7 (a) where flow rate is zero] that occur between adjacent pillars. Analytes could be trapped between these two pillars, reducing collection efficiency and preventing analyte residues to be flushed out. Moreover, higher pressure on the inlet of the device might imply higher risk to reach the critical pressure difference [Red area in Fig.7 (b)]. This is the point at which the balance held by surface tension is broken, driving the fluid to occupy the space of the air pillars.

The offsetting pillar pattern [Figure 2-7 (c), (d)] shows that there exists a detectable flow rate through the entire pillar section of the channel. This flow would help optimize the performance of both the collection mechanism and flushing of the system. Hence, we choose the offsetting holes pattern for our device fabrication.

2.5 Experiment Setup and Results

2.5.1 Nesslar's Reagent and Aerosolized Particles

2.5.1.1 Air Pillar Device

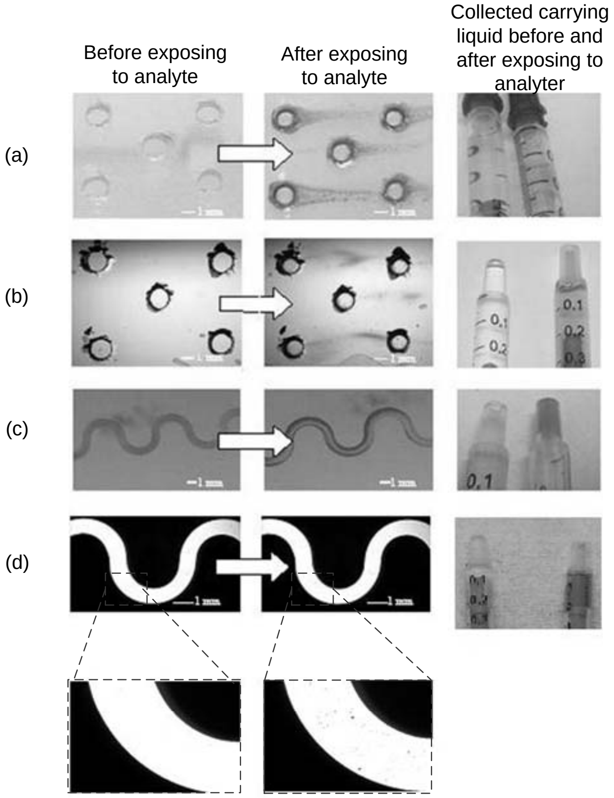

Figure 2-8. Responses of collection devices to analytes, as well as collected liquid (in syringes) before (left) and after (right) exposure: a) Air pillar device with Nessler's reagent

(NR) flowing through the channel. It was then exposed to ammonia, and a color change from no color to rust brown occurred only a few seconds later. b) Air pillar design with DI water flowing through the channel. The device was then exposed to aerosolized Kool-Aid®. Color change to purple in the channel was observed. And the color change is more obvious by comparing the collected liquids. c) Serpentine channel device with NR flowing through. Color in the channel changed to rust brown when the channel was exposed to gaseous ammonia. d) Channel device with DI water flowing through the channel. The device was then exposed to aerosolized Kool-Aid®. As shown in the zoomed-in area, particles appears in the flow after exposing to the analyte, and the color changed to purple, as shown in the syringe containing the collecting liquids.

A single-level air pillar microfluidic channel device was placed in a sealed container with an inlet and an outlet for ammonia to provide the operation environment for the device. Nessler's Reagent (NR), an aqueous liquid with no color, was infused at a rate of 15μL/min through the channel of the air pillar device [Figure 2-8(a)]. A 30% ammonia solution was aerosolized by a nebulizer and the vaporized NH_3 gas was pumped into the container. When NH_3 came in contact with NR, a rust brown substance, NH_4OH, was produced, indicating that NH_3 was collected into the channel at the gas-liquid interfaces of the air pillars [Fig 8 (a)]. Syringes were connected to the outlet of the air pillar device during the whole ammonia application to collect the analyte-containing fluid for analysis afterwards.

After that, Kool-Aid®, a water soluble food product, was selected for the aerosolized particle test because of its ease of use and safety. The single-level air pillar device was filled with DI water (as the collecting liquid) at a rate of 15μL/min [Fig 8 (b)]. Kool-Aid® was aerosolized with a nitrogen air gun and blown laterally over the device, allowing the particles to permeate the air pillar gas-liquid interfaces. The particles were collected by the dynamic DI water flow in the channel. These experiments show that with properly chosen collecting fluids, the device was able to collect both gaseous samples and solid particles.

2.5.1.2 Channel device

As shown in the Figure 2-8 (c), the channel is flushed with NR at a rate of 15μL/min after being placed in an open container. NH_3 from 30% ammonia solution was then vaporized into the container with a nebulizer. The color of the NR stream in the device then began to change to rust brown, from the side walls of the collecting fluid stream to the center of the stream.

Then the same device was placed under a stereoscope and flushed with DI water at a rate of 15μL/min [Figure 2-8 (d)]. Kool-Aid® was aerosolized and blown laterally towards the stream. The images in Figure 2-8 (d) show how particles were collected within the stream, proving that the device was able to collect both gaseous samples and aerosolized particles with proper collecting fluids.

2.5.1.3 Multi-level air pillar device

A 2-level air pillar device was placed in a sealed container with 2 inlets and an outlet. Figure 2-9 shows a scheme of the device, indicating that different collecting fluid can be used in different levels for different analytes. In the experiment, the upper fluid level was NR and the lower level was DI water, and both were infused at a rate of 15μL/min. Kool-Aid® was introduced first and blown laterally with respect to the air pillars. The device response in Fig 10 (b) shows that both fluid had the capacity to collect aerosolized particles. Then, NH_3 was vaporized by a nebulizer from 30% ammonia solution and introduced into the container through another inlet. The NH_3 reacted with the NR in the upper level to create the rust brown NH_4OH, as shown in Figure 2-10 (c). The collection process continued for 5 minutes and adequate samples were gathered into syringes, as shown in Figure 2-10 (d).

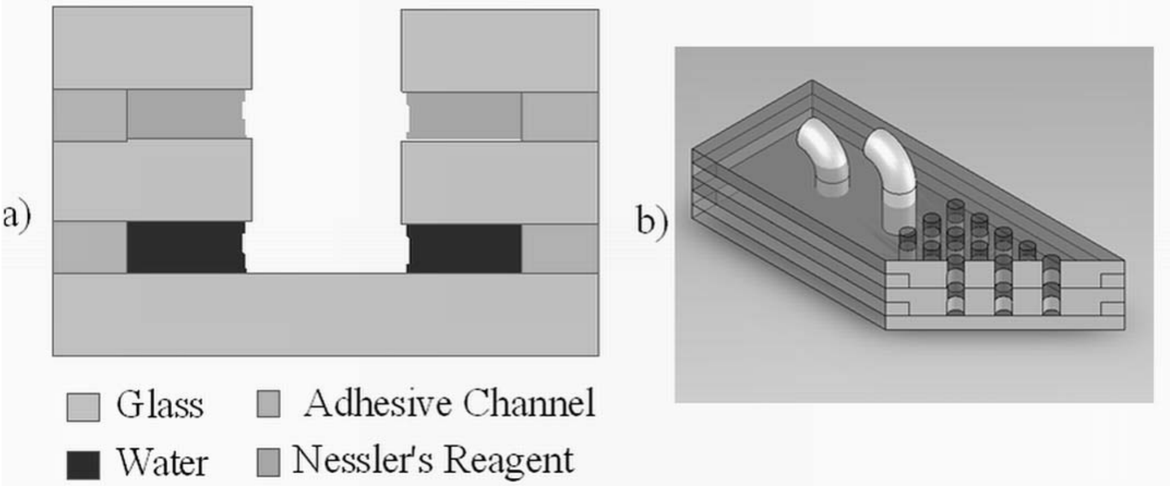

Figure 2-9. A scheme of two-layer air pillar device design. a) Cross-sectional diagram of the two-layer device with aligned air pillars. b) 3D rendering of a multilayer air pillar device.

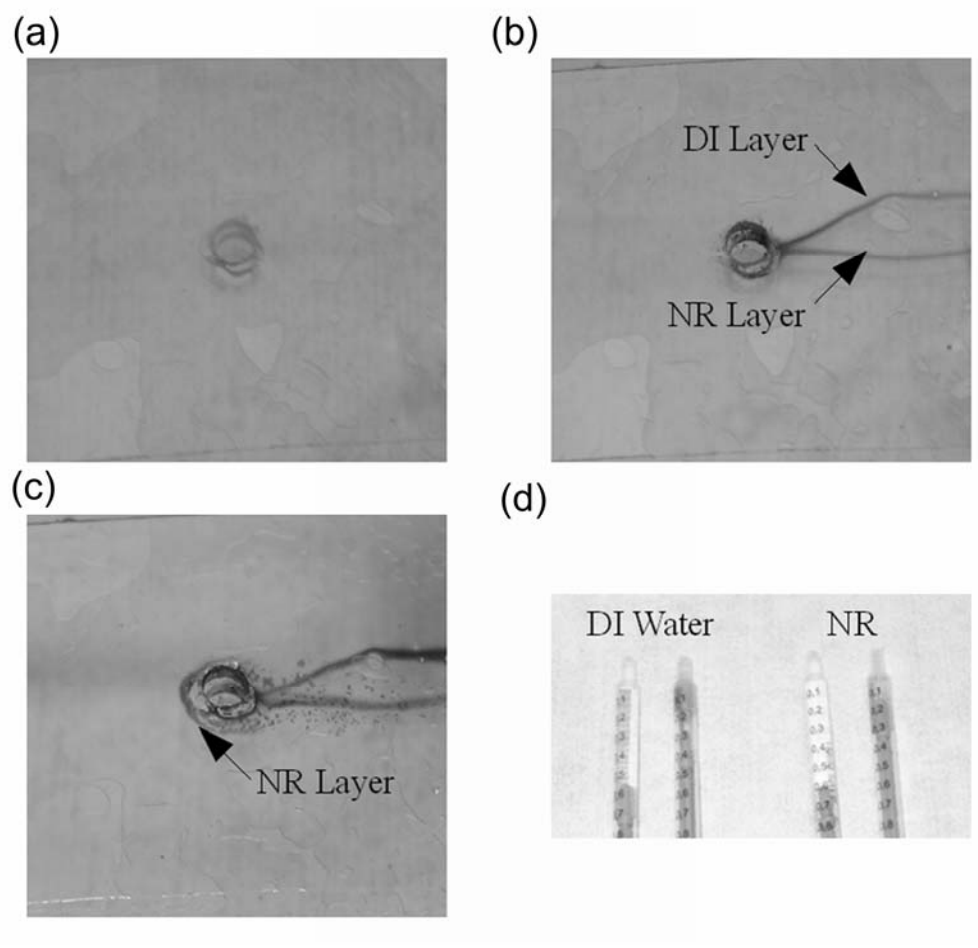

Figure 2-10. Response of a two-layer air pillar device to different analytes: a) Image of two-level design with both DI water and NR (both limpid liquids) flowing through the system as the collection solvent. b) The device was first exposed to the aerosolized Kool-Aid®, which introduce a color change in both the DI water layer and the NR layer. c) The device was then exposed to aerosolized ammonia from a nebulizer which caused the rust brown substance only in the NR layer. d) Collected analyte-carrying collecting fluid from both layers: left: pre-exposure samples; right: post-exposure samples.

2.5.2 Optimization of Collection Devices

To further increase the sensitivity of our devices, a straight forward method might be increasing the area of the gas/liquid interface. This optimization is expected to allow more analyte to be collected at a fixed time period, provided the same properties of the devices and the collecting liquid stream.

2.5.2.1 Channel device

Two devices with different channel geometries were tested at the same time for a comparison. One channel design is a straight line with inlets at one end and outlets at the other; the other channel bears a design of a serpentine structure with 5 semicircle turns as shown in Figure 2-1(top), which has a larger exposed surface area because of the increased channel length. Both devices were placed in a sealed container with an air inlet, an outlet and an internal circulating fan. The container was then flushed with nitrogen to ensure an inertia pre-testing environment. The devices were then infused with de-ionized water at a fixed rate of 10μL/min, which was previously determined in order to prevent the balance of forces at the lateral gas/liquid interface from breaking. After the whole DI-water fluid channel was formed and confined by surface tension, a nebulizer was used for vaporizing from ammonia solution for 5 seconds, and then both the inlet and outlet were sealed and the circulating fan turned on to enhance a uniform distribution of the gaseous NH_3. The NH_3 concentration in ammonia solution was carefully determined, so the amount of gaseous NH_3 was large enough to prevent the competition between the two devices, and small enough so the NH_3 concentration in the collecting DI-water stream did not exceed the saturation concentration limit during the collecting process. Liquid streams carrying analyte were then conducted out from the outlet of the devices and then collected in 1mL syringes for subsequent analysis.

The collected DI-water liquid stream samples were then injected into ethyl vinyl acetate microbore tubings with a 1.5mm diameter and a length of 7.5cm. 2mm 76-gauge magnet wires were then inserted into each end of the tubing as probe tips, and the resistance is measured by a bench resistance meter. With the controlled amount of NH_3, higher concentrations of ions in the analyte-collecting liquid streams should result in higher conductivities, i.e. lower resistances.

The experimental results are shown in Table 1. As we expected, since the serpentine channel design has an exposed gas/liquid interface area almost 4 times larger than the simple straight design, the analyte-carrying DI-water collected from the serpentine device has a lower resistance, indicating that it collects more analyte in a fixed time period comparing to the straight channel device.

2.5.2.2 Air pillar device

The air pillar devices were tested using the similar method as the channel devices. The only difference is that the flow rates of the air pillar design were able to be slightly higher, 15µL/min, due to the robustness of the pinning effect at the edge of the holes.

A one-air pillar device, a five-air-pillar device and a nine-air-pillar device were tested simultaneously. As expected, more air pillars imply larger gas/liquid interface area, thus larger ion collecting rate, and thus lower resistance.

Table 2-1. Resistance of DI-water in various collection devices after exposure to gaseous NH3 and the area of gas-liquid interface in different devices. DI water, with an impedance of 1.4GΩ, was flowed through each device at a constant rate. Different devices were then exposed to vaporized NH3 for several minutes at various concentration levels.

Aqueous NH_3 Concentration	**Conductance Measurements Comparison**		
	Device Type	***Surface Area(mm^2)***	***Resistance***
30%	1 Hole Air Pillar Device	0.12	60 MΩ

Aqueous NH$_3$ Concentration	**Conductance Measurements Comparison**		
	Device Type	***Surface Area(mm^2)***	***Resistance***
30%	5 Hole Air Pillar Device	0.53	51 MΩ
30%	9 Hole Air Pillar Device	0.95	44 MΩ
30%	Straight Gold Device	5	53 MΩ
30%	Serpentine Gold Device	9.5	46 MΩ
3.65%	1 Hole Air Pillar Device	0.12	240 MΩ
3.65%	5 Hole Air Pillar Device	0.53	191MΩ
3.65%	9 Hole Air Pillar Device	0.95	137 MΩ
3.65%	Straight Gold Device	5	173 MΩ
3.65%	Serpentine Gold Device	9.5	156 MΩ

2.5.2.3 Real-time sensing (conductance measurement) using air pillar device

A 5-hole air pillar device was fabricated and then two 2mm wire probes were inserted directly into the channel through the device inlet and outlet. The whole device was then placed in a fume hood and the probes were connected to a bench top resistance meter, measuring resistance of collecting fluid stream dynamically. DI water, the collecting liquid, was infused liquid, was infused through the device at a fixed rate of 15µL/min during the experiment. Gaseous NH$_3$ was introduced using a nebulizer and further distributed by a circulating fan in the chamber and the upstream of air flow from the fume hood. This environment allowed for constant flow of air over the device and provided a mimic of real world scenarios. After the device was flushed with DI water for 5 minutes, a baseline measurement was taken, and a baseline liquid resistance of ~46±0.5 MΩ is obtained. Then the device is exposed to NH_3 vaporized from 30% ammonia solution. The transient change of resistance was recorded each 15 seconds until a quasi-static state was reached. Similar experiment was conducted for 15% and 7.5% NH_3. Between each experiment, the residue NH_3 was completely vented away and the collecting liquid residue in the device was flushed by DI-water for 5 minutes.

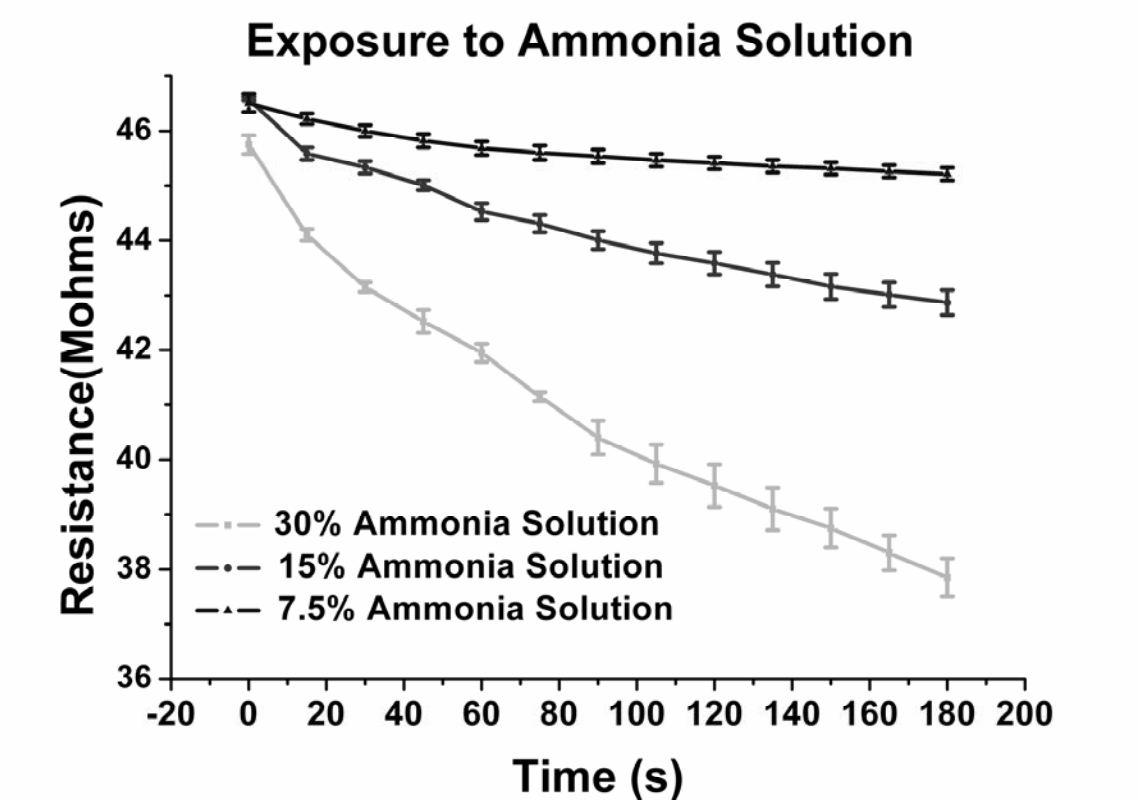

Figure 2-11. Response of the air pillar collecting device exposing to gaseous NH3. The 5-hole air pillar device was infused with DI-water stream at a rate of 15µL/min and then exposed to different concentrations of ammonia solution. NH3 was vaporized by a nebulizer at time 0 for each concentration.

Figure 2-11 shows how the device acted in response to the NH_3 concentration in environment. Decreasing the NH_3 by half would result in roughly a linear response of the resistance of the collecting liquid stream in the device. This demonstrates that the device is able to detect different concentrations of NH_3 in real time. The error bars on the detection curves demonstrate the reliability of the device. Only a simple and short discarding step is needed to prepare it for re-acquisition and measurement.

2.6 Conclusion

We have created devices with reliable liquid–air interfaces for aerosolized particle and gas collection (and detection) using different methods. The simplistic and inexpensive fabrication of these devices provides robustness and the potential to integrate them into practice detection systems. With liquid–air interfaces pinned at hydrophilic/hydrophobic SAM-gold/glass interfaces, we have demonstrated channel devices with lateral gas-liquid interfaces, and further optimized the channel structure to increase the exposing interface area to the environment analytes. We also demonstrated collecting devices utilizing air pillar structure to pin the liquid–gas interface at the edge of patterned holes. Because of the much simpler fabrication process and robust materials (i.e. no SAM thin film), these devices have much longer shelf life, lower cost and better compatibility. Moreover, the capability of collecting different analytes in the environment simultaneously with different levels has been demonstrated by multi-level air pillar devices.

2.7 References

[1] B. Zhao, N. O. L. Viernes, J. S. Moore, and D. J. Beebe, *Journal of the American Chemical Society*, vol. 124(19), pp. 5284-5285 (2002).

[2] J. Atencia and D. J. Beebe, *Nature*, vol. 437, pp. 648-655 (2005).

[3] C. A. Pope, *The New England Journal of Medicine*, vol. 351, pp.1132-1134 (2004).

[4] B. H. Timmer, K. M. van Delft, W. W. Koelmans, W. Olthuis, and van den Berg, *IEEE Sensors Journal*, vol. 6(3), pp.829–835 (2006).

[5] E. D. Lester and A. Ponce, *IEEE Engineering in Medicine and Biology Magazine*, vol. 21, pp. 38–42 (2002).

[6] T. Frisk, D. Rönnholm, W. V. D.Wijngaart, and G. Stemme, *Lab on a Chip*, vol. 6, pp.1504–1509 (2006).

[7] S. S. Sridharamurthy and H. Jiang, *IEEE Sensors Journal*, vol. 7(9), pp. 1315-1316 (2007).

[8] J. Greenwood, D. Cheng, Y. Liu, H. Jiang, *Proceeding of IEEE Sensors*, pp. 720-723, 2008.

[9] B. Zhao, J. S. Moore, and D. J. Beebe, *Analytical Chemistry,* vol. 74, pp. 4259-4268 (2002).

[10] B. Zhao, J. S. Moore, and D. J. Beebe, *Science*, vol. 291, pp. 1023-1026 (2001).

[11] A. Hibara, S. Iwayama, S. Matsuoka, M. Ueno, Y. Kikutani, M. Tokeshi, and T. Kitamori, *Analytical Chemistry,* vol. 77, pp. 943- 947 (2005).

[12] G. M.Whitesides, E. Ostuni, S. Takayama, X. Jiang, and D. E. Ingber, *Annual Review of Biomedical Engineering*, vol. 3, pp. 335-373 (2001).

[13] D. Ryan, B. A. Parviz, V. Linder, V. Semetey, S. K. Sia, J. Su, M. Mrksich, and G. M. Whitesides, *Langmuir*, vol. 20, pp. 9080-9088 (2004).

[14] G.T. Roman, M. Wang, K. N. Shultz, C. Jennings and R. T. Kennedy, *Analytical Chemistry,* vol 80, pp. 8231–8238 (2008).

[15] Y. N. Xia, E. Kim, M. Mrksich, and G. M. Whitesides, *Chemistry of Materials*, vol. 8, pp.601-603 (1996).

[16] C.D. Bain, G.M. Whitesides, *Journal of the American Chemical Society*, vol. 110 (11), pp. 3665–3666 (1988).

[17] Y. Y. Feng, Z. Y. Zhou, X. Y. Ye, and H. J. Xiong, *Sensors and Actuators A: Physics*, vol. 108(1), pp. 138–143 (2003).

[18] D. Cheng, Y.-J. P. Choe, and H. Jiang, "Controlled Liquid–Air Interfaces and Interfacial Polymer Micromembranes in Microfluidic Channels," *IEEE/ASME Journal of Microelectromechanical Systems*, vol. 17(4), pp. 962-973, 2008.

Chapter 3. Microfluidic sensing devices employing *in situ*-formed liquid crystal thin film for detection of biochemical interactions

(Parts of the contents in this chapter have been published as:

Y. Liu, D. Cheng, I-H. Lin, N. L. Abbott and H. Jiang, "Microfluidic sensing devices employing in situ-formed liquid crystal thin film for detection of biochemical interactions," Lab on a Chip, 2012, DOI: 10.1039/c2lc40462a)

In this chapter, we demonstrated *in situ*-formed sensing devices which employ thermotropic nematic liquid crystal (LC). Highly reproducible methods to create uniform LC thin film on treated substrate is critical for utilizing LCs for sensing purposes. Although biochemical sensing using liquid crystals (LC) has already been demonstrated, relatively little attention has been paid towards the fabrication of *in situ*-formed LC sensing devices. Herein, we demonstrate a highly reproducible method to create uniform LC thin film on treated substrates, as needed, for LC sensing. We use shear forces generated by the laminar flow of aqueous liquid within a microfluidic channel to create LC thin films stabilized within microfabricated structures. The orientational response of the LC thin films to targeted analytes in aqueous phases was transduced and amplified by the optical birefringence of the LC thin films. The biochemical sensing capability of our sensing devices was demonstrated through experiments employing two chemical systems: dodecyl trimethylammonium bromide (DTAB) dissolved in an aqueous solution, and the hydrolysis of phospholipids by the enzyme phospholipase A_2 (PLA_2).

3.1 Introduction

Highly sensitive, portable and cost-effective bio/chemical sensors are critical elements for various applications, such as chemical warfare agent detection and point-of-care diagnostics [1, 2]. Recently, the long-range orientational ordering of LCs has been demonstrated to provide one effective approach for the implementation of such sensors [3-5] particularly based on the effects of interfacial binding of biomolecules [6-9]. Due to the high sensitivity of LCs to the target and absence of the need for a label, this approach has been demonstrated to be an effective method for real-time, label-free and high sensitivity sensing. For example, vapor-phase analyte concentrations in the parts-perbillion range have been successfully detected [5, 10]. LC has also been exploited to report the reorganization of lipid monolayers driven by specific lipid-protein binding events [11]. Other materials, such as functional pH-dependent amphiphilic polymers, have also been combined with LCs to transduce the environmental information into optical signals [12]. In order to transduce and amplify interfacial molecular interactions into optical signals utilizing LCs, one of the essential steps is to create a stable LC thin film, which is supported on a solid surface to provide a pre-defined alignment to the LC. Because the alignment of LC is fixed at the solid-LC interface, changes in the ordering of the LC within the thin film can be attributed to interactions between the LC film and targeted analytes at the free-LC film interface. Changes in the ordering of the LC molecules lead to changes in the optical properties of the LC film, which are easily transduced via the transmission of polarized light through the LC film. However, such LC thin films need to be "open", i.e. have free surfaces that can be exposed to and interact with analytes. Thus, fabrication methods for conventional LC devices, though relatively mature, (for example, LC vacuum injection for LC display manufacturing) are not applicable for LC sensing devices. Current effective approaches to form LC thin films for sensing include manually pipetting LC into the square openings of a transmission electronic microscopy (TEM) grid [8, 9] or using arrays of microfabricated pillars to stabilize thin LC film [5]. Those approaches, though producing high-quality LC thin films, require manual handling of LCs, and are time consuming and require skilled personnel. Processes that lead to uniform and reproducible LC thin films are still sought, particularly *in situ* forming schemes, which do not rely on manual procedures.

A preliminary study of *in situ*-formed LC thin films in microfluidic devices was conducted and reported by D. Cheng, *et. al.* [13]. Herein, a more detailed study of this approach is conducted and represented. The *in situ* preparation of the LC thin film as well as the sensing process of the devices is driven by laminar flows in the microchannel, which can be precisely controlled by pre-defined flow rates of the laminar flows with a programmable syringe pump. Thus, the need for manual handling is eliminated. In particular, after filling the channel with LC, the laminar flow of the aqueous target phase is introduced into the channel at a high flow rate. The shear force of the laminar flow removes the bulk LC in the micro-sensing channel, and creates LC thin films in a supporting structure. The birefringence of the LC thin film can then be monitored by polarized optical microscopy (POM). The thickness and quality of the LC thin film were calculated by a computational fluid dynamics (CFD) simulation and then demonstrated by subsequent testing with two model chemical systems. One of the model systems reported the existence of dodecyl trimethylammonium halide (DTAB) in the de-ionized (DI) water phase [14, 15]. The second system involved binding of phospholipase A_2 (PLA_2) to a monolayer of phospholipids hosted at the LC-aqueous interface [8, 16] and subsequent enzymatic hydrolysis of the phospholipid.

3.2 Chemical and hardware materials

Liquid crystal, 5CB and 1-Decanethiol [$CH_3(C_9H_{18})SH$], 96%, L-α-dilauroyl phosphatidylcholine (L-DLPC), N,N-dimethyl-N-octadecyl-3-amino-propyltrimethoxysilyl chloride (DMOAP) and phospholipase A_2 (PLA_2) from naja mossambica mossambica were purchased from Sigma-Aldrich (St. Louis, MO, USA). N- hexadcyl mercaptan [$CH_3(C_{15}H_{30})SH$], 92% was purchased from Acros Organics (Geel, Belgium). Glass slides were purchased from Fisher Scientific (Pittsburg, PA, USA). Microfab NI 100 make-up solution and Microfab NI 100 wetting agent were purchased from Enthone-OMI (West Haven, CT, USA). High purity Ni gauze, #39704 was purchased from Alfa Aesar (Ward Hill, MA, USA). Positive photoresist (PR), AZ P4620, was purchased from Clariant Corporation (Somerville, NJ, USA). Double adhesive spacer (250-µm-thick) was acquired from 3M Co. (St. Paul, MN, USA). Ethyl vinyl acetate microbore tubings were purchased from Cole Parmer Co. (Vernon Hills, IL, USA).

3.3 Principles of Device Preparation and Operation

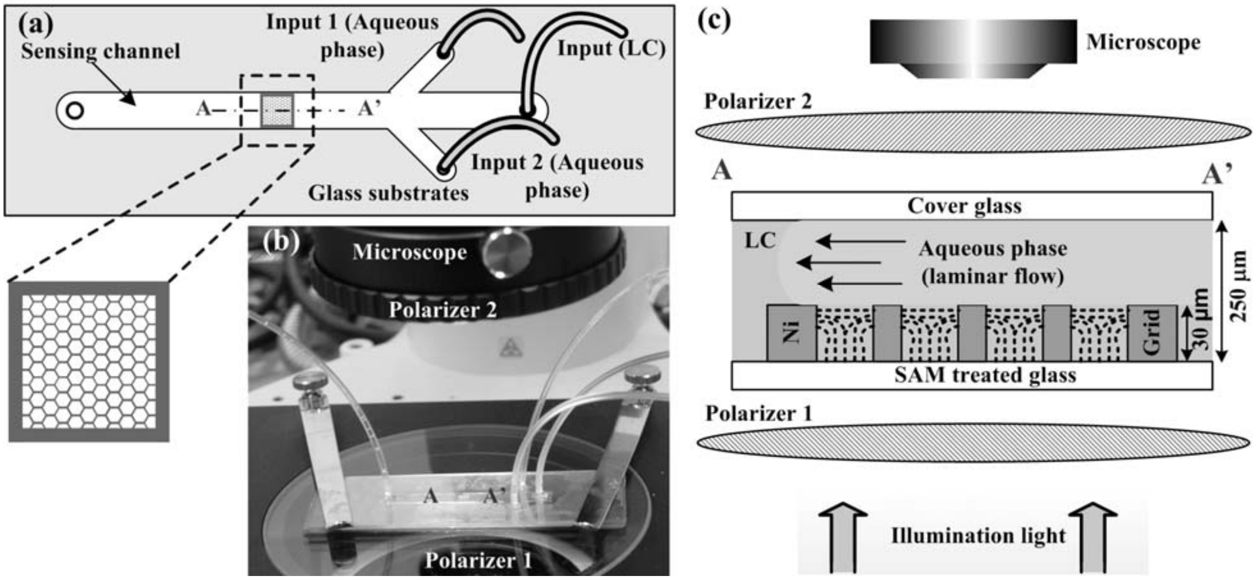

Figure 3-1. Schematic illustration and photographs of the sensing device. (a) Top view of the device structure. The square structure with hexagonal grid is electroplated on the substrate. The microfluidic channel is created on a glass substrate with a 250 mm thick adhesive spacer. (b) Images of the device mounted on a POM. (c) Schematic of the sensing setup. The figure portion in the middle shows the side view of the device along AA'. Pre-filled 5CB in the sensing channel is pushed away by the laminar flow of aqueous liquid. The shear force of the flow forms LC-aqueous interface at the top of the grid structure. The device is placed between two crossed polarizers and illuminated from the bottom.

The concept and structure of the sensing device is shown in Figure 3-1. As shown in Figure 3-1(a), an LC supporting structure is integrated into a microfluidic sensing channel. The supporting grid structure consists of hexagonal cells separated by Ni bars, as shown in the blow up image. The height of the Ni grid is ~30 μm, and the diameter of a single hexagonal cell is ~0.3 mm. The hexagonal cell array is confined by 0.3 mm width Ni lines in a 3 mm × 3 mm square area. The dimensions listed above are so chosen as to provide the required LC film thickness and lead to uniform orientation of the LC (as the exposing area of each cell is small). The microchannel has one inlet for LC, one inlet for an aqueous target phase and one inlet for another aqueous target phase. The whole device is positioned between two crossed linear polarizing filters, with a white light source illuminating from bottom. Thus, the birefringence of the LC thin film can be monitored by a microscope [Figure 3-1(b)]. As described above, for effective sensing with LC thin films, we need to: first, pre-treat the supporting substrate so that the substrate-LC interface provides a pre-defined alignment/orientation to the LC; second, limit the thickness of the LC film below 100 mm (as described in past studies [5, 10]) so that the interfaces of the LC will control the orientation of the entire LC film. Thus, the optical properties of the LC thin film will be solely determined by the LC orientation at the LC-aqueous target phase interface.

Deposition of self-assembled monolayers (SAMs) on a substrate is an effective way to anchor the orientation of LC at a substrate¨CLC interface [17, 18]. By depositing a 20 nm layer of gold and applying a mixture of alkanethiols, a mixed alkanethiol SAM is formed on the substrate such that the LC mesogens contacting the SAM assume a homeotropic alignment. The requirement for the semi-transparent gold layer, however, complicates the fabrication process and increases the cost. Moreover, the transmittance of the gold layer in the visible light region is less than 50% [18].

DMOAP, in contrast, is an alkoxysilane surfactant used commonly for treating metal-oxide/glass so that the LC at the interface assumes homeotropic alignment [19, 20, 21]. After a simple dipping and rinsing process, a silane layer applied to the glass substrate is permanently bonded to the substrate in such a manner that the orienting groups of the silane coupling agent molecules are free to interact with and align neighboring LC molecules [22]. Moreover, the monolayer of DMOAP does not significantly reduce the transmittance of visible light. Guided by the above observation, we fabricated sensing devices functionalized using both gold/alkanethiol SAMs and DMOAP coatings, and demonstrated that they exhibit similar performances. This way, we also demonstrated that our sensing device is compatible with multiple coating methods. Thus, if a target analyte interacts with alkanethiols, we can alternatively use alkoxysilane coating on our device, and vice versa.

Due to the small dimension of the microfluidic channel (~4 mm × 3 mm × 0.25 mm), the behaviour of the infusing liquid usually falls into the laminar flow regime. Thus, phenomena associated with the laminar flow can be used to create the LC thin film as well as the LC-target phase interface. As shown in the side view (middle image) in Figure 3-1(c), after filling the channel with LC, the flow of the aqueous target phase is introduced into the channel at a high flow rate. The shearing force of the laminar flow removes the bulk LC in the micro sensing channel, and leaves LC thin films in the supporting structure. The thickness of the LC thin film is about the height of the supporting Ni grid, i.e. ~30 μm.

3.4 Fabrication of the sensing devices

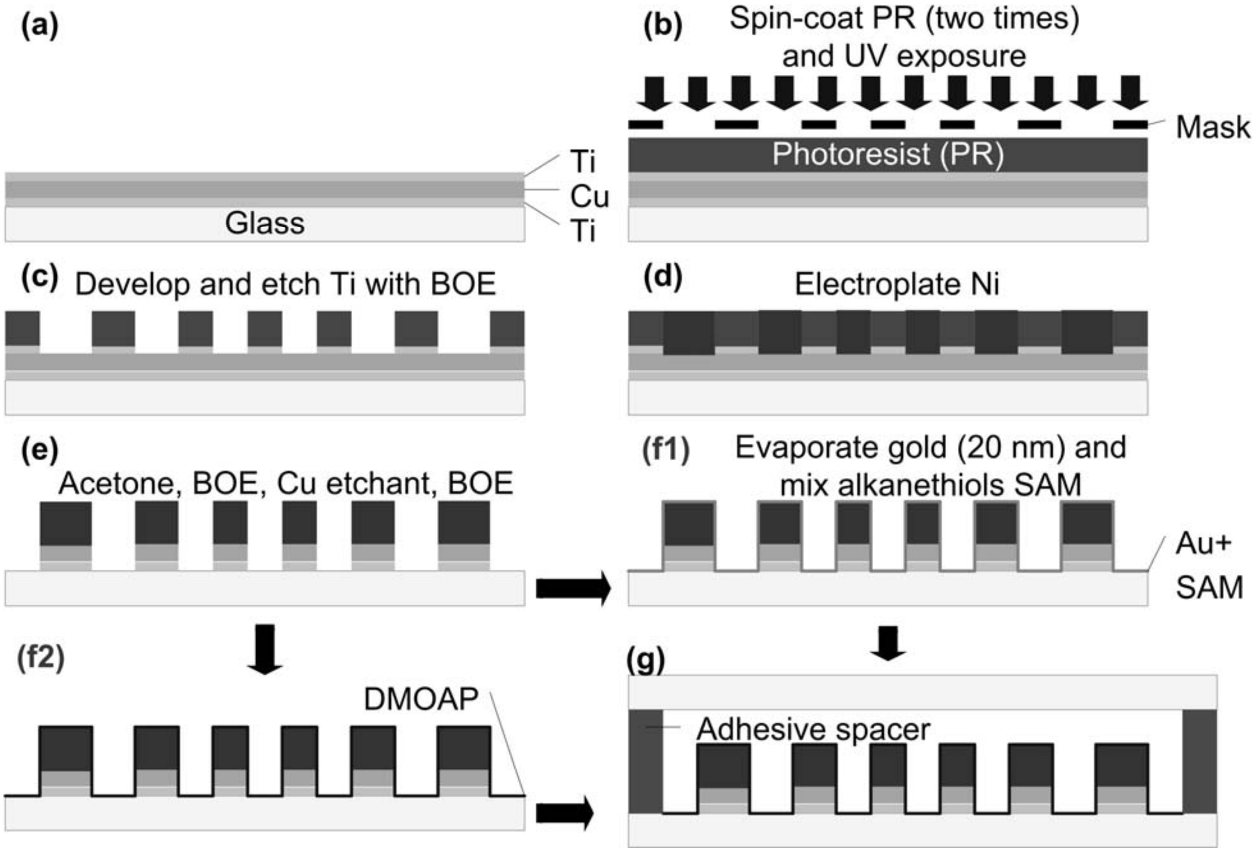

Figure 3-2. Fabrication process for the sensing devices. (a) The process starts from a glass substrate coated with Ti/Cu/Ti as seed layers for following electroplating; (b) Two layers of photoresist (PR) (~40 mm in thickness) are spin-coated on the seed layer and the pattern of the nickel grid is defined by UV exposure; (c) The pattern is then transferred by developing PR. Cu seed layer is exposed by etching Ti. (d) 30 µm of Ni is electroplated with photoresist as a mold; (e) Remove PR with acetone, followed by removal of the exposed seed layers with buffered oxide etchant (BOE) and Cu etchant; (f1) 20 nm translucent Au layer isevaporated on the structure. Mixed alkanethiol SAM is formed on top of the Au layer; or (f2) a layer of DMOAP is directly coated on the glass substrate; (g) The substrate with the structure is bonded with a cover glass slide using 250 µm adhesive spacers.

The fabrication process of the devices is illustrated in Figure 3-2. The process started from microscopy glass slides with seed layers of titanium/copper/titanium (Ti/Cu/Ti, 225/300/350 Å). The seed layers were coated using a CHA-600 e-beam evaporator (CHA Industris, Fremont, CA, USA). A photoresist (PR) mold was patterned on the Ti/Cu/Ti-coated glass slide to define the Ni-plated grid structure. Two layers of PR were spin-coated on top of the seed layers so that a 40 μm thick PR mold was formed. To pattern the PR, a printed transparent film (Imagesetter, Inc. Madison, WI, USA) was used as the mask. An ultraviolet (UV) lamp (OmniCure^{TM} Series 2000, EXFO Photonic Solutions Inc. Ontario, Canada) was used to expose PR at the intensity of 24.6 mW cm^{-2} for 80 s [Figure 3-2 (b)]. After PR patterning and developing, the top Ti layer that was not covered by PR was removed by buffered oxide etchant (BOE, 100:1), leaving Cu exposed [Figure 3-2 (c)]. The Ni electroplating bath, agitated at a constant 200 rpm, consisted of 1:0.01 Microfab NI 100 make-up solution and Microfab NI 100 wetting agent. The bath temperature, maintained at a temperature of 50 ± 1ºC, was continuously monitored by a type-K thermocouple probe (Omega HH506A, OMEGA Engineering, Inc, Stamford, CT, USA). Ni gauze was used as the Ni source (anode) for electroplating. Ni was electroplated onto the active sites on the glass slide (cathode; where Cu was exposed) at a rate of approximately 0.60–1.00 μm min^{-1} so that Ni structure with a thickness of 25–30 μm was achieved in ~30 min [Figure 3-2 (d)]. After the completion of Ni electroplating, the PR mold was removed by acetone. The Ti/Cu/Ti seed layers were removed by BOE (100:1) and Cu etchant, leaving Ni grid on a clear glass substrates [Figure 3-2 (e)].

The grid LC supporting structure was functionalized in two different methods so that 5CB was anchored homeotropically on the substrate. The first method is shown in Figure 3-2 (f1).

The glass substrate with Ni structure was covered with a thin film (~20 nm) of Au using an e-beam evaporator. The whole substrate was then immersed into an ethanol solution of mixed alkanethiols: $CH_3(C_{15}H_{30})SH$ and $CH_3(C_9H_{18})SH$ for 2 h followed by thoroughly rinsing with ethanol and drying with nitrogen stream. Thus a self-assembled monolayer (SAM) of mixed alkanethiols was formed on the Au layer. The second method, as shown in Figure 3-2 (f2), was directly applying a layer of DMOAP by immersing the glass slide into 1% v/v solution of DMOAP in DI-water, followed by rinsing with DI-water and drying with nitrogen.

As shown in Figure 3-2 (g), a 250 µm thick double adhesive spacer was cut and formed a channel structure, as shown in Figure 3-1(a). A clean glass slide with pre-drilled inlet/outlet holes was bonded on the functionalized glass substrate with the spacer and the channel was formed. Ethyl vinyl acetate microbore tubings were finally plugged into the inlet/outlet holes and were sealed by epoxy glue. Solutions were filled into separate syringes and introduced into the inlets of the channel by syringe pumps. The flow rate of each liquid phase was controlled by programming the syringe pump.

3.5 Simulation of the formation of the LC thin film

To further investigate the interaction between an aqueous solution and the LC in a microchannel during the shearing process, and to determine optimal flow conditions that lead to formation of the LC thin film (i.e., velocity and pressure limits of the cutting fluid), a transient simulation based on the volume of fluid (VOF) model was performed, using ANSYS Fluent®. The VOF model is based on the integral of a fluids characteristic function in a control volume (in our finite element analysis, each meshed cells in the fluid region), and thus it allows us to track the shape and position of the liquid-liquid interface, making it a suitable method for our simulation. To reduce the calculation time, a simplified 2D model was created based on the dimensions of the cross-section view of the actual devices. Since the Reynolds number of the aqueous “cutting” flow is small due to the small dimension of the microchannel, the flow can be safely considered as laminar flow, and the interaction between two supporting cells which is far away from each other can be neglected. Thus, it’s safe to further reduce the simulation load to investigate only 4 cells in the channel. Subsequently, the length of the channel in the simulation can be scaled to 4 mm. The distance of each cell was set at 0.3 mm. The heights of the Ni grids were fixed at 30 μm, while the height of the channel was fixed at 250 μm, consistent with the actual devices. The channel was assumed to be pre-filled with 5CB, and at time instant 0, “cutting fluid” (here, DI-water) was introduced into the channel through the inlet. The pressure at the outlet of the channel was assumed to be 1 atm. (open outlet). Since the experiments are conducted under a room temperature of ~27ºC and no local temperature increase is observed, the temperature dependency of surface tension and viscosity can be neglected. The interfacial tension at the nematic LC/water interface is set at ~5.5 dyne cm^{-1} [23]. The contact angle of water on the treated substrate in the 5CB media is assumed to be 130º, consistent with the static contact angle from experiment results [24]. At 27 ºC, nematic 5CB can be considered as a Newtonian fluid [25], and a constant viscosity of 30 mPa·s is utilized. The speed of the water flow was varied from 1 mm s^{-1} to 50 mm s^{-1}, in order to find an optimized solution for controlling the DI-water cutting and formation of the liquid crystal thin layer.

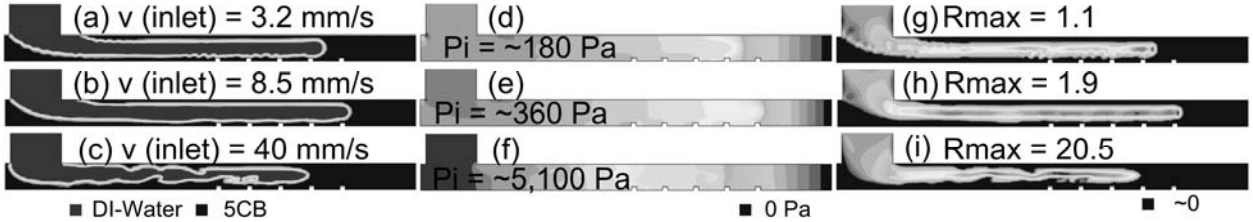

Figure 3-3. Behaviors of DI-water flows ‘‘cutting’’ into bulk 5CB in the channel with different velocities ((a) (b) (c)), pressure distributions in the channel corresponding to each cases ((d) (e) (f)), and local Reynolds numbers in the channel ((g) (h) (i)). The figures depict the situations when the DI-water flow is passing the 3rd and 4th cells. Pi indicates the maximum pressure in the device. Rmax indicates the maximum local Reynolds number in the channel.

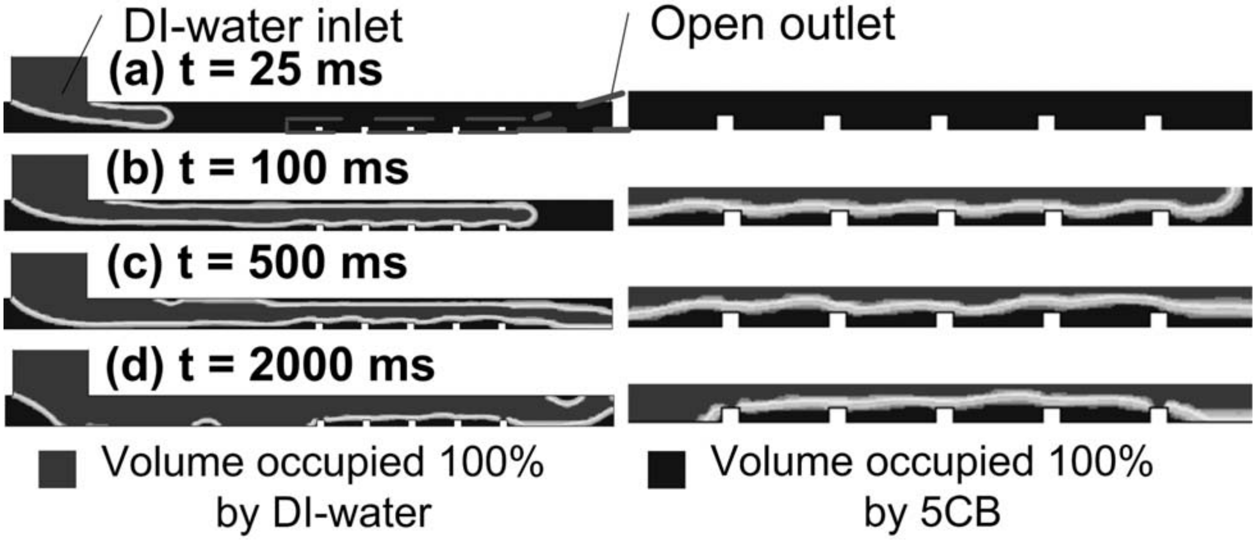

Figure 3-4. Distribution of DI-water and 5CB in the channel at different time instants, calculated from a volume of fluid (VOF) model. The distribution of DI-water and 5CB is represented by their “volume fraction” (i.e. the volume ratio of DI-water or 5CB to the total volume). The blow-up figures on the right depict the DI-water/5CB interface near the Ni grids. (a) At 25 ms, DI-water continues to flow into the channel at a velocity of 8 mm s^{-1}. (b) After 100 ms, the 5CB above the Ni grids is already pushed away by the water flow (i.e. the “cutting” process). (c) After 500 ms, DI-water reaches the outlet of the channel. (d) After 2000 ms of continuous water flow, only a thin layer of 5 CB is left near the region of Ni grids.

As shown in Figure 3-3, the pressure near the device inlet increased rapidly with the increasing of the cutting fluid velocity, assuming that the outlet was kept open. When the fluid velocity was not high (for example, 3.2 mm s^{-1}), the relative pressure inside the device was kept lower than 200 Pa [Figure 3-3 (d)], and the smooth movement of the fluid could be considered as a “plug” flow [Figure 3-3 (a)]. Though slowly, this plug flow was able to “cut” into the 5CB bulk without disturbance of the integrity of the 5CB/ aqueous interface. The cutting fluid maintained to possess the plug flow property until the velocity at the inlet increased to more than 8.5 mm s^{-1} and the maximum pressure in the device exceeded 360 Pa [Figure 3-3 (b), (e)]. These also demonstrated the feasibility of our devices as the pressure and fluid velocity needed for cutting were not high, and a simply-fabricated fluid channel or chamber could withstand it. Contour plots of the local Reynolds numbers in different locations in the channel are shown in Figure 3-3 (g) (h) (i). The maximum Reynolds numbers increase almost linearly with increasing flow rate at the inlet. The Reynolds numbers are kept below 35 during our simulation, thus we can safely consider our flow to be in the laminar regime. However, a further increase in the velocity would further increase the inner pressure of the device, and would cause circulations to appear in the flow. The former can cause leakage at the weak points of the devices (fragile points on the devices due to device structure, such as connectors at the inlets and outlets of the devices), while the latter may eventually disturb the integrity of the 5CB/aqueous interface which will result in the poor uniformity and poor quality of the LC films. Figure 3-3 (c) and (f) suggest these phenomena become evident with an initial cutting fluid velocity of ~40 mm s^{-1}.

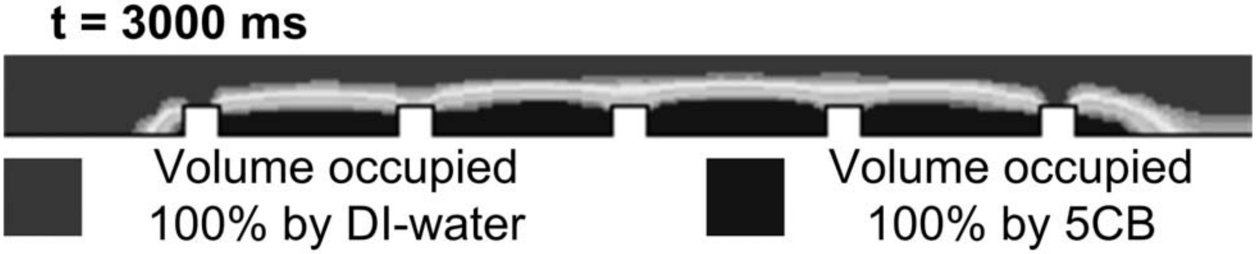

Figure 3-5. The interface between DI-water and 5CB at quasi-static state after the cutting process. The volume fractions of both liquids show an abrupt change at the interface (different colors corresponding to different volume fractions).

Figure 3-4 shows the distribution of DI-water and 5CB in the channel at different time instants, with an infusing water flow speed of 8 mm s^{-1} (i.e. volumetric flow velocity 400 μL s^{-1}, according to the dimension of the channel). The speed of the DI-water stream was then decreased to 0 abruptly after 2000 ms. The DI-water formed a "plug" flow which pushes away 5CB inside the channel. However, with the protection of Ni grids, a thin layer of 5CB liquid crystal was left, and the thickness of the layer was about 30 mm, the same as the thickness of the Ni grids. As shown in Figure 3-5, a figure of the 5CB/DI-water distribution near the Ni-grid area after 3000 ms depicts the simulated quasi-static status of the 5CB thin layer. Judging from the uniformity of the LC thin film, the operation time, and the stability of the thin film over the simulation time, this control profile (flow velocity: 400 μL min^{-1} for 2000 ms for "cutting" then 0 for 1000 ms to let the remaining LC settle) was an optimized solution, thus was used for subsequent experiments with adaptation to the dimensions of the real devices.

3.6 Creating LC thin film using laminar flow and sensing test with DTAB surfactant

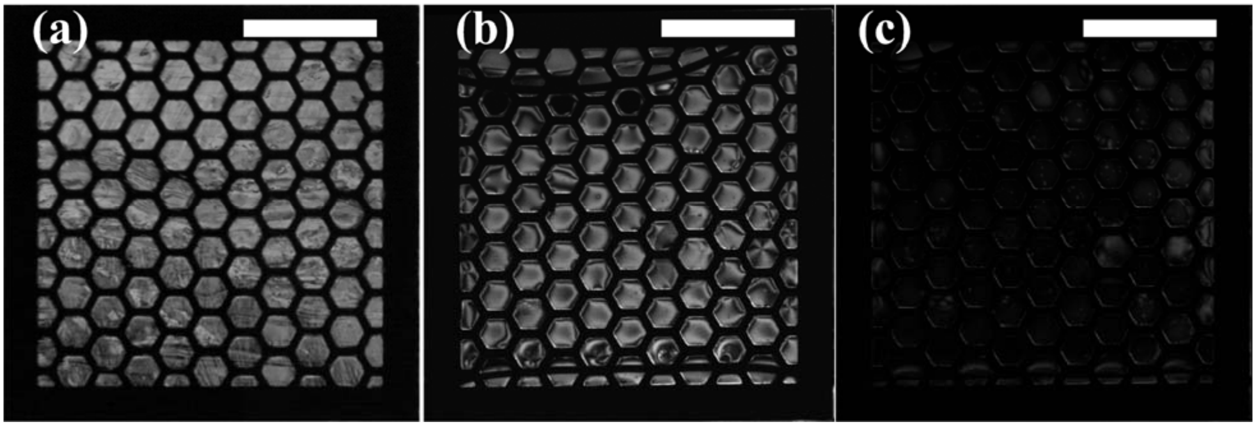

Figure 3-6. POM images of the sensing process for 10 mM DTAB surfactant with a gold/SAM coated device. (a) The sensing channel was filled with LC; (b) the sensing channel was flushed with DI-water, a LC thin film was created within the Ni grid structure at the bottom of the channel; (c) surfactant solution was introduced into the channel. The LC thin film responded to the surfactant and resumed a homeotropic alignment profile. Scale bar: 1 mm.

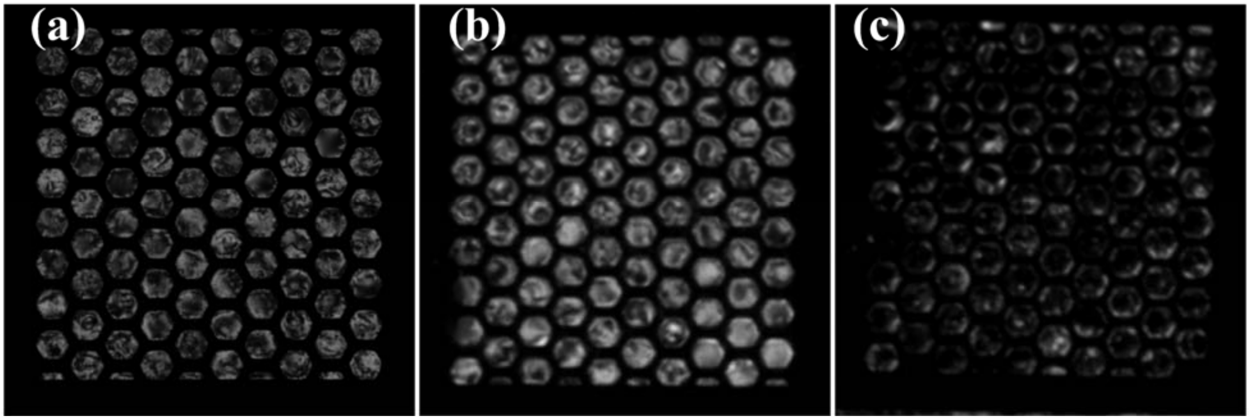

Figure 3-7. POM images of the sensing process for 10 mM DTAB surfactant with a DMOAP coated device. (a) The sensing channel was filled with LC; (b) the sensing channel was flushed with DI-water, a LC thin film was created within the Ni grid structure at the bottom of the channel; (c) surfactant solution was introduced into the channel. Scale bar: 1 mm.

Since the orientations of thermotropic LCs in contact with water are sensitive to the types and concentrations of surfactants present in the aqueous phase [15], a simple yet effective way to preliminarily test the sensing performance of our devices is to firstly form the LC thin film by DI-water cutting, then introduce surfactant solution into the microchannel and observe the interaction at the LC-aqueous interface. For easy preparation without losing generality, we chose DTAB (10 mM in DI-water) as our analyte for the sensing test [15].

Figure 3-6 and Figure 3-7 show the process of DTAB surfactant detection by our sensing devices with the gold/SAM coating and the DMOAP coating, respectively. For both devices, LC was first introduced by one of the syringe pumps and filled the Ni supporting grid as well as the rest of the space in the sensing channel. The thickness of LC in the sensing channel was ~250mm, through which the orientation of the LC mesogens could not be communicated. The LC mesogens, therefore, resumed a non-homeotropic orientational profile through the thickness of the sensing channel, which resulted in birefringence through the thickness of the LC film. Bright images of the 5CB in the grid structure, as shown in Figure 3-6 (a) and Figure 3-7 (a), were obtained under the cross-polar observation with the POM.

DI-water was then subsequently introduced into the sensing channel at a high flow rate of 400 μL min^{-1}, which corresponded to a linear velocity of 8 mm s^{-1}, given the dimension of the channel. As expected in previous simulation, this laminar flow cut and pushed away the 5CB above the grid structure, leaving only 5CB thin films supported by the grid. The resultant 5CB thin films possessed approximately the same thickness of the grid structure (~30μm). A horizontal LC-aqueous interface was thus automatically formed on top of the hexagonal cells. Because the bottom surfaces of the sensing channels were functionalized with mixed alkanethiol SAM or DMOAP, 5CB molecules at the bottom of the thin films were anchored homeotropically, i.e. perpendicular to the surface. At the same time, the orientation of the LC at the top surface of the thin films depends on the property of the contacting target phase or the analytes in that phase. The 5CB mesogens at the top surface possess planar alignment upon contact with DI-water. Therefore, a bend and splay deformation was formed in the 5CB thin film, i.e. from the homeotropic alignment at the bottom to the planar alignment at the top [14]. Under the cross-polar observation, 5CB thin film in the grid appeared bright and colorful, as shown in Figure 3-6 (b) and Figure 3-7 (b). A comparison of Fig. 6(b) with 6(a) reveals that the interference colors in Figure 3-6 (b) are lower order, consistent with a decrease in LC film thickness. In addition, within Figure 3-6 (b), the interference colors are consistent within the sample, indicating formation of a uniform film.

When 10 mM DTAB surfactant solution was introduced into the sensing channel, the 5CB molecules at the top surface assumed a homeotropic alignment, i.e. perpendicular with the LC-aqueous interface. The LC thin film thus had a uniform vertical molecular alignment profile through the thickness. Under this condition, the LC thin film does not possess optical birefringence. As a result, a dark image as shown in Figure 3-6 (c) and Figure 3-7 (c) was obtained under cross-polar observation. There are various methods to quantitatively evaluate the optical signals generated by the LC, for example, using an avalanche photodiode array to detect and measure the intensity of light coming out of each region of LC. Here, we analyzed the images of each cell in the device and calculated the intensity of light transmitted through crossed polarizers, quantified as the average luminance of the images, utilizing ImageJ (Open source image analysis software developed at the National Institutes of Health). The resulting average luminance of the LC region in Figure 3-7 (b) was 120, while in Figure 3-7 (c) , the average luminance was less than 30.

3.7 Characterizing interaction between phospholipase 2 (PLA_2) and phospholipids (L-DLPC)

Phospholipase A_2 hydrolyzes L-phospholipids to form fatty acid and lysophospholipid products. Phospholipases are involved in inflammatory responses and thus are widely investigated in a range of basic biological and medicinal contexts [26-28]. The characterization of phospholipase activity using a phospholipid monolayer self-assembled at the aqueous-LC interface was demonstrated to be an effective method of reporting the activity of PLA_2 [15]. The orientation of LCs is coupled to the presence of phospholipids, thus the enzymatic events occurring on the phospholipids can be clearly characterized by examine the optical property of the LCs. Thus, our LC thin film devices are expected to be an effective real-time label-free method for sensing/characterizing the PLA_2 binding/hydrolyzing event. The sensing results utilizing the gold/SAM coated device was described in detail, while the DMOAP coated device gave a similar performance, as shown in Figure 3-11.

3.7.1 Creating Lipid-decorated LC-aqueous Interfaces

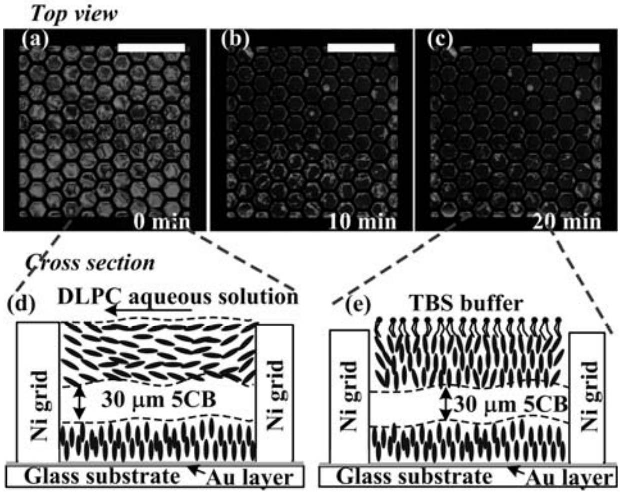

Figure 3-8. Process of creating lipid-decorated LC-aqueous interface with a gold/SAM coated sensing device. LC thin film was formed in the grid structure by cutting with an aqueous dispersion of L-DLPC vesicles, similar to the process described above (flow rate: 8 mm s^{-1}). (a)(d) The freshly-formed thin film demonstrated birefringence upon cutting. (b) 10 min after the cutting DLPC solution was set to be steady. (c)(e) Over a period time of 20 min, monolayer of DLPC was formed at the LC–aqueous interface. LC molecules coupled

with the phospholipid at the interface and resumed homeotropic orientation. With cross-polar observation, the bright and colourful image of LC thin film evolved to a dark image. When the interface was formed, TBS buffer solution slowly flew across the lipid-laden interface for ten minutes rinsing away remaining phospholipid, as shown in the last image (flow rate: 0.3 mm s^{-1}). Scale bar: 1 mm.

To form a lipid monolayer at the aqueous-5CB interface, an aqueous dispersions of L-DLPC was used to conduct the LC pushing and cutting process. Similar with the cutting and pushing process with the DTAB aqueous surfactant solution, the laminar flow of aqueous dispersion of L-DLPC vesicles, at the flow rate of 400 μL min^{-1} (8 mm s^{-1}), was introduced into the sensing channel by a syringe pump and formed 5CB thin films contained in the Ni grid. When the 5CB thin films were initially formed, the optical texture was bright [Figure 3-8(a)], indicating the planar orientation of the 5CB mesogens at the LC-aqueous interface. The tilted angle of 5CB mesogens relative to the surface normal decreases linearly through the 5CB thin film from nearly 90° (to the vertical direction) at the 5CB-aqueous interface to 0° at the mix alkanethiol SAM-5CB interface on the substrate surface. The bending and splay distortions in the 5CB thin film resulted in a continuous variation of the mesogen orientation through the thickness, as shown in Figure 3-8(d), which resulted in a birefringence (~0.09) in the 5CB thin film. This led to a yellow/green/pink appearance under cross-polar observation. After 5CB thin film was formed in the whole grid structure, the phospholipid solution in the sensing channel was set to be static (flow velocity = 0). As time evolved, due to the interaction between the lipid and the 5CB mesogens, homeotropic anchoring of 5CB at the aqueous-5CB interface was achieved, as shown in Figure 3-8 (e). Given the homeotropic alignment of mesogens at the mix alkanethiol SAM-5CB interface at the bottom of the LC film, the 5CB mesogen orientational alignment profile through the film was undistorted. Towards the end of the equilibration period, dark and uniform optical texture was observed, as shown in Figure 3-8 (c). This implied that a monolayer of L-DLPC lipids was formed at the aqueous-5CB interface. For following sensing of PLA_2 binding, lipid-free buffer solution (TBS) was introduced into the sensing channel at a flow rate of 20 μL min^{-1}, flushing away unabsorbed phospholipids.

3.7.2 Detecting PLA_2 binding/hydrolyzing events

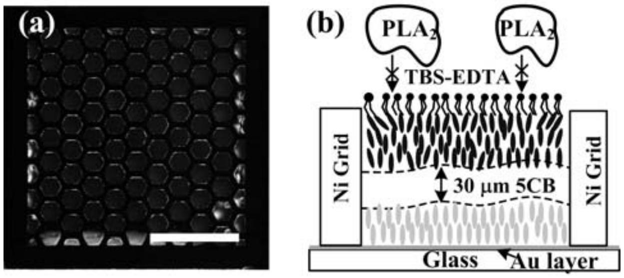

Figure 3-9. PLA_2 solution without Ca^{2+} was introduced into the microfluidic channel by an external syringe pump. The orientation of the LC molecules in the grid structure did not change even after 40 min of exposure to the solution, and under cross-polar observation, the LC remained dark. Scale bar: 1 mm.

The presence of Ca^{2+} is needed for PLA_2 to be functional. The active site of PLA_2 binds Ca^{2+}, which in turn facilitates PLA_2 to recognize the sn-2 acyl bond of L-phospholipids and catalytically hydrolyze the phospholipids, forming single-tailed lysophospholipids and fatty acids [25]. Once formed, the products either phase-separate from the phospholipids or desorb from the interface, thus disrupting the anchoring of the LC.

In our experiment, as a control we first introduced 100 nM PLA_2 solution without Ca^{2+} after the formation of the L-DLPC monolayer at the aqueous-5CB interface. The dark appearance of the 5CB thin film did not change even 40 min after introducing PLA_2 solution without Ca^{2+}. This indicated that the binding event of PLA_2 with the L-DLPC did not take place and the 5CB mesogens remained homeotropic alignment at the interface, consistent with previous study (Figure 3-9) [25].

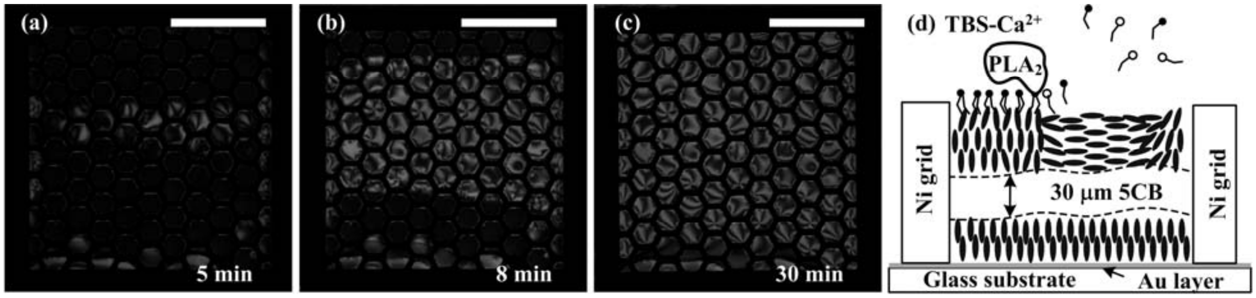

Figure 3-10. 100 nM PLA_2 solution in TBS-Ca^{2+} was introduced into the sensing microchannel by an external syringe pump at a flow rate of 20 µL min^{-1} (0.4 mm s^{-1}). Interaction between PLA_2 and the monolayer of DLPC induced orientational transition of the 5CB mesogens, resulting in a gradual change of the appearance of the LC grids from dark to bright and colorful. The whole process took ~30 min. Scale bar: 1 mm.

A 100 nM PLA_2 solution with Ca^{2+} (also 100 nM) was then introduced into the sensing channel at a flow rate of 0.4 mm s^{-1}. The 5CB thin film in the grids at the centre of the sensing channel started to change the appearance to a colorful and bright image. This indicated that, with the presence of Ca^{2+}, specific binding of PLA_2 to the monolayer of 5CB supported at the aqueous-5CB interface and subsequent hydrolysis of the monolayer took place. In a period of 30 min, this optical texture appearance transit started from the grids close to the center of the channel and spread towards the two sides of the width of the sensing channel, as shown in Figure 3-10 (a)-(c). This optical texture appearance transit indicated that the PLA_2 bound with and hydrolyzed themonolayer of L-phospholipid, which triggered the orientational transition of 5CB to a planar alignment, as shown in Figure 3-10 (d).

3.7.3 Characterizing interaction between PLA_2 and L-DLPC with a DMOAP-coated device

Experimental procedures similar to that described above were employed to demonstrate the capability of the DMOAP-coated device for sensing the PLA2 binding/hydrolyzing event, as shown in Figure 3-11. Figure 3-11 (a) shows the POM image of the LC thin film right after cutting by the aqueous dispersions of L-DLPC. The L-DLPC dispersions were then set steady. The birefringence began to disappear in 2 min and the thin film turned almost completely dark under cross-polar observation (Figure 3-11 (b)). Without Ca^{2+}, PLA_2 was not be able to bind and hydrolyze L-DLPC, thus the POM image remained dark after 40 min since the LC thin film exposed to 100 nM PLA_2 solution without Ca^{2+} (Figure 3-11 (c)). However, after introducing Ca^{2+} (100 nM), PLA2 began to catalytically hydrolyze L-DLPC and thus the LC thin film in most of the hexagonal cells under cross-polar observation turned to bright and colorful in 30 min [Figure 3-11 (d)].

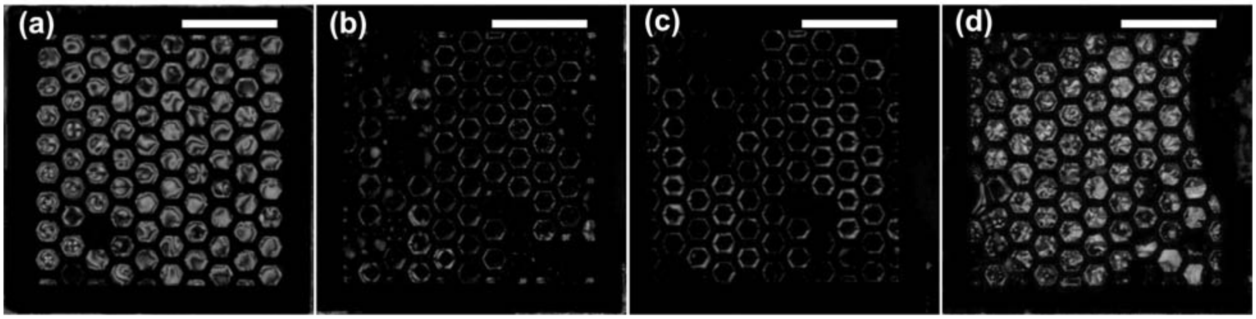

Figure 3-11. Sensing PLA_2 binding/hydrolyzing event using a DMOAP-coated device. (a) The LC thin film immediately after cutting by the L-DLPC dispersion (flow rate: 8 mm s^{-1}). (b) 20 min after the cutting. (c) 40 min after introducing the PLA_2 solution without Ca^{2+} (flow rate: 0.4 mm s^{-1}). (d) 30 min after introducing the 100 nM PLA2 solution with Ca^{2+} (flow rate: 0.4 mm s^{-1}). Scale bar: 1 mm.

3.7.4 Repeatability test

The repeatability of the devices was tested. In this test, DTAB solution was used to form the LC thin film as well as to modulate the LC mesogen alignments. In the first round experiment, LC film was formed by the laminar flow of DTAB solution and stabilized to demonstrate homeotropic alignment as described above. The colour of the film under cross-polar observation changes from bright to dark. Then the sensing channel was purged using ethanol so that DTAB solution as well LC thin film was removed from the channel. N_2 stream was then applied to dry the channel for 30 min. LC was again introduced into the channel and filled the hexagonal Ni container at the bottom. DTAB solution was introduced into the channel and for the second time formed the LC thin film. The experiment was repeated twice, and similar qualities of LC thin films and LC mesogen alignments were achieved. For each cutting process, it was observed that only less than 5% LC cells in the device did not correctly fill after the cutting process. The lifetime of the device, i.e. the time of the LC film remains stable and active, was not optimized in these experiments, but we observed it to be more than 48 h. This was determined by forming the LC film with DI water, storing the device for 36 h, and then using the device to performing sensing tests (as described above).

3.8 Conclusion

We have demonstrated microfluidic devices which integrated thermotropic LC sensing into microfluidic channels. The fluidic dynamic phenomenon in the laminar flow regime was investigated and employed to create a layer of LC thin film in an in situ fashion, which greatly improved the efficiency of preparing the delicate LC sensing element and eliminated the complicated and skill-required manual handling. The subsequent sensing tasks thus can be conducted in situ, and remotely controlled by lab-on-a-chip control methods. As a result, the devices inherit the high sensitivity, real-time sensing and label-free detection properties from LC sensing, and meanwhile possess the capability to conduct multiple consecutive sensing tasks, as well as the detecting tasks in the hazardous environment inaccessible to human being. Two model systems were demonstrated on the sensing devices. The alternative flow of the aqueous dispersion of DTAB surfactant and DI-water was detected by the orientational transits of the LC mesogens and reflected as the real time change of the LC optical texture. LC optical texture change also effectively indicated the spontaneously assembling of the L-DLPC phospholipid monolayer at the LC interface and subsequently, the binding/hydrolyzing event of PLA2 in the sensing channel with this phospholipid monolayer. In future studies, we will focus on using photon detectors to quantify the intensity of the light transmitted through the LC and polarizers, and investigate in detail the sensitivity and reliability of our system for a variety of chemical systems.

3.9 References

[1] R. S. Muller and IEEE Electron Devices Society, *Microsensors*, New York: IEEE Press, 1991.

[2] B. H. Timmer, K. M. van Delft, W. W. Koelmans, W. Olthuis, and A. van den Berg, *IEEE Sensors Journal,* vol. 6, pp. 829-835 (2006).

[3] R. R. Shah and N. L. Abbott, *Science*, vol. 293, pp. 1296-1299 (2001).

[4] K.L. Yang, K. Cadwell, and N.L. Abbott, *Sensors and Actuators: B-Chemical*, vol. 104, pp. 50-56 (2005).

[5] S. S. Sridharamurthy, K. D. Cadwell, N. L. Abbott, and H. Jiang, *Smart Materials and Structures,* vol. 17 (2008).

[6] R. R. Shah and N. L. Abbott, *Journal of the American Chemical Society*, vol. 121, pp. 11300-11310 (1999).

[7] J. J. Skaife, J. M. Brake, and N. L. Abbott, *Langmuir,* vol. 17, pp. 5448-5457 (2001).

[8] J. M. Brake, M. K. Daschner, Y. Y. Luk, and N. L. Abbott, *Science*, vol. 302, pp. 2094-2097 (2003).

[9] J. S. Park, S. Teren, W. H. Tepp, D. J. Beebe, E. A. Johnson, and N. L. Abbott, *Chemistry of Materials,* vol. 18, pp. 6147-6151 (2006).

[10] K. L. Yang, K. Cadwell, and N. L. Abbott, *the Journal of Physical Chemistry B*, vol. 108, pp.20180-20186 (2004).

[11] T. L. Yang, S. Y. Jung, H. B. Mao, and P. S. Cremer, *Analytical Chemistry,* vol. 73, pp. 165-169 (2001).

[12] M. L. Kinsinger, B. Sun, N. L. Abbott, and D. M. Lynn, *Advanced Materials*, vol. 19, pp. 4208-4212 (2007).

[13] D. Cheng, I. H. Lin, N. L. Abbott and H. Jiang, *IEEE Transducers,* Denver, CO, USA, June 21–25, 2009.

[14] J. M. Brake and N. L. Abbott, *Langmuir*, vol. 18, pp. 6101-6109 (2002).

[15] J. M. Brake, A. D. Mezera, and N. L. Abbott, *Langmuir*, vol. 19, pp. 6436-6442 (2003).

[16] J. M. Brake and N. L. Abbott, *Langmuir*, vol. 23, pp. 8497-8507 (2007).

[17] V. K. Gupta and N. L. Abbott, *Physical Review E*, vol. 54, pp. R4540-4543 (1996).

[18] R. A. Drawhorn and N. L. Abbott*, the Journal of Physical Chemistry*, vol. 99, pp. 16511–16515 (1995).

[19] T. Rasing and I. Muševič, *Surfaces and Interfaces of Liquid Crystals*, Springer, 2004.

[20] X. Bi, S. Huang, D. Hartono and K. Yang, *Sensors and Actuators B: Chemical,* vol. 127, pp. 406-413 (2007).

[21] S. Noonan, A. Shavit, B. R. Acharya and D. K. Schwartz, *ACS Applied Material Interfaces*, vol. 3, pp. 4374–4380 (2011).

[22] F. J. Kahn, *Applied Physics Letters*, vol. 22, pp. 386-388 (1973).

[23] J.-W. Kim, H. Kim, M. Lee and J. J. Magda, *Langmuir*, vol. 20, pp. 8110–8113 (2004).

[24] Z. Yang and N. L. Abbott, *Langmuir*, vol. 26, pp. 13797–13804 (2010).

[25] A. G. Chmielewski and E. Lepakiewicz, *Rheologica Acta,* vol. 23, pp. 207–210 (1984).

[26] E. A. Dennis, *the Journal of Biological Chemistry*, vol. 269, pp.13057–13060 (1994).

[27] J. P. Nicolas, Y. Lin, G. Lambeau, F. Ghomashchi, M. Lazdunski and M. H. Gelb, *the Journal of Biological Chemistry*, vol. 272, pp. 7173–7181 (1997).

[28] A. Argiolas and J.J. Pisano, *the Journal of Biological Chemistry*, vol. 258, pp.13697–13702 (1983).

Chapter 4. Lateral tunable liquid microlenses for enhanced fluorescence emission in microfluidic channels

(Parts of the contents in this chapter have been published as:

Y. Liu, B. Aldalali, and H. Jiang, "Lateral tunable liquid microlenses for enhanced fluorescence emission in microfluidic channels,"IOP Journal of Micromechanics and Microengineering, in press.)

Microlenses are important components of optofluidics systems and their lab-on-a-chip applications. In this chapter, we report on liquid microlenses that can be *in situ* formed in microchannels in a single batch via pneumatic control. These microlenses have optical axes that are parallel to the substrate, and their focal length can be pneumatically tuned separately and independently. In addition, the microlenses can also be pneumatically removed individually and reformed on demand. The parameters affecting the profiles and optical properties of the microlenses, such as the pressure difference and gravity, were investigated by simulation. We then demonstrated the enhancement of fluorescence emission in a microfuidic channel using our microlenses to focus attenuated excitation laser beams into regions of interest in the channel. With the microlenses, the region with visible fluorescence response was enlarged by up to 13 times and the intensity of fluorescence emission was enhanced by up to 38 times, compared to the cases without the lenses.

4.1 Introduction

Optofluidics is a rapidly developing area that combines the advantages of microfluidics and optics [1]. Important applications of optofluidics include optofluidic dye lasers [2], liquid-core/liquid-cladding waveguides [3], and especially, lab-on-a-chip (LoC) systems [4–6].

Optofluidic LoC systems not only have many advantages inherited from their microfluidic attributes, such as portability, low-cost and low consumption of analytes and reagents, but also have advantages such as accuracy and remote controllability, inherited from their optic system aspects.

Microlenses, as one of the important components of optofluidic LoC systems, have been intensively investigated recently and utilized in many applications [7–10]. Solid interface microlenses have been integrated into microfluidic chips through photoresist reflow [11], isotropic etching [12], chemical synthesis [13] and self-assembly processes [14]. However, these solid-interface microlenses are generally fixed in their shapes and thus not tunable in their focal lengths. For LoC applications, due to the requirements of compactness and versatility, tunable focal length of microlenses is not only an advantage, but also sometimes a necessity [15]. Tunable microlenses can be realized through various approaches, including reorientation of liquid crystals [16], electrowetting [17], mechanical actuation of polymeric materials [18], hydraulic pressure [19] or mechanical pressure [20], flow-rate-introduced shape change of the interface between two immiscible fluids [21–23] and self-adaptation to environmental parameters using responsive polymers [24–27]. These liquid-based lenses also have additional advantages such as smoother lens surfaces. However, many of these tunable microlenses rely on costly/complicated fabrication processes, various functional materials and complicated external hydrodynamic control systems. Most of them are also difficult to be removed and reformed on demand. Moreover, most of these lenses have their optical axes perpendicular to the substrates (i.e. vertical lenses) so that other optical components involved (e.g., light sources and photodetectors) have to be laid out in different layers, which increases the difficulty in the integration and alignment of the components. Novel mechanical-wetting-based lenses have also been demonstrated [28, 29] with a relative low-cost and simply approach; however, the sizes of the lenses are relatively large (~7 mm).

We previously reported cylindrical liquidmicrolenses that are in situ formed and integrated within microfluidics through the pneumatic manipulation of fluids inside microchannels. Such microlenses are formed via liquid–air interfaces of liquid droplets, which are pinned at T-shaped junctions of channels.Via pneumatic control, these microlenses can uniquely be repositioned, removed, and reformed at predetermined locations within microchannels on demand. Moreover, their focal lengths can be tuned in a large range, from several micrometers to infinity, along the microchannels parallel to the substrate [30, 31].

To further extend our investigation on such pneumatically controlled microlenses, in this chapter we report on *in situ* formed microlens assemblies realized through an extended and improved fabrication and pneumatic control process. Comparing to previously-reported single microlenses [30], multiple lateral microlenses with different optical axes were formed in one batch. The focal length of each microlens can be pneumatically tuned separately and independently, thus being more flexible in applications. The microlenses also inherit the advantages such as large range of tuning, ability to be removed and reformed, smooth surface, simple fabrication process, and minimal requirement of external control systems once formed and sealed. More characterizations of the microlenses were performed, such as simulations of the focal length of the lenses as a result of the pneumatic tuning process, examination of the effect of gravity on the shape of the lenses and the optical properties of the microlenses. To further demonstrate their potential applications in LoC, we also demonstrated the enhancement of fluorescence excitation in microfluidic channels with the microlenses.

4.2 Formation, tuning, removal and reformation of the tunable liquid microlenses

4.2.1 Principles and structures

In a microfluidic channel network, the inner surfaces of the channels can be properly treated to form a hydrophobic monolayer, which is essential for the liquid-air interface to be perpendicular to both the top and bottom surfaces. Then, to form *in situ* tunable liquid microlenses, liquid droplets (here de-ionized, or DI, water) are pneumatically segmented from a static bulk fluid and then driven along the designated channels to desired T-shape junctions under controlled air pressure. Each of such droplets usually has two liquid–air interfaces, one of which would be pinned at the T-junction. This concept is depicted in Figure 4-1.

When a difference in air-pressure is applied to the droplet and equals the internal capillary pressure caused by the difference in curvature between the liquid-air interfaces of the droplet, the liquid-air interface at the junction could protrude out of the junction, and be pinned at the edges- i.e. it tends to form a convex meniscus. The shape of the other interface depends on the static contact angle of the liquid on the inner channel surface under homogeneous pneumatic pressure [31]. Thus, owning to the treated inner surfaces of the channels, it can be flat, forming a plano-convex cylindrical lens, or concave, forming a positive meniscus lens (with a larger radius of curvature than the convex surface). Such lenses have optical axes parallel to the substrate plane. Because of the ‘pinning’ effect at the junction, the curvature of the pinned liquid–air interface can be adjusted by varying the difference in the air pressure across the two liquid–air interfaces within a certain range.

4.2.2 Microfluidic System Setup

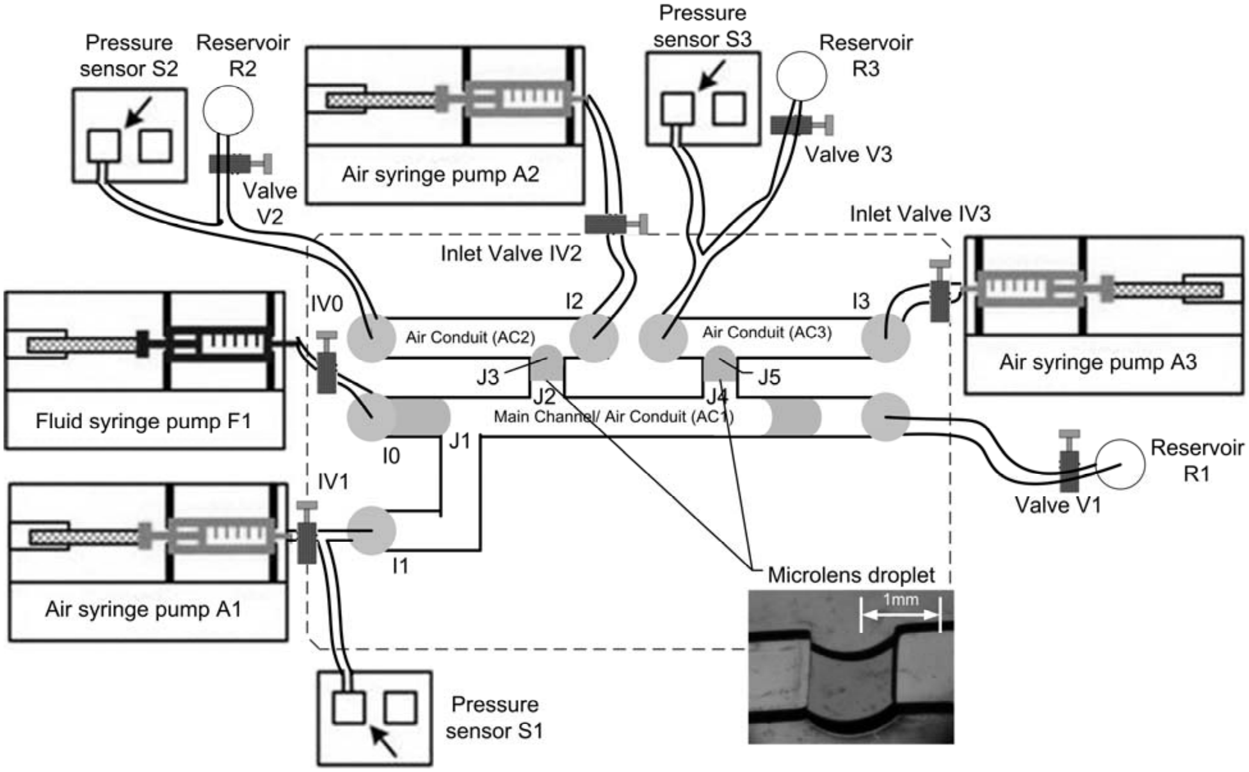

Figure 4-1. Schematic of the microfluidic setup for *in situ* formation of two microlenses. The widths of all microchannels were 1 mm except for the channel segments between junctions J2 and J3, and between J4 and J5, which were 0.75 mm. The depths of the channels were kept uniform at 250µm.

As shown in Figure 4-1, middle section, to form a multiple microlenses, a channel network was designed comprising of a main channel and multiple air conduits (for tuning), with lens channels between them, where the droplets of the liquid microlenses resided. The main channel was the place for forming the DI water droplets and driving them towards the junctions; it also served as an air conduit in the tuning process (AC1). Therefore, it had two inlets, one for the bulk fluid (I0) and one (I1) for the air plug to cut the droplets at J1. The air conduits provided the pneumatic control path for the lenses, thus each of them had an inlet for air (I2 and I3). The junctions (J2 and J3, J4 and J5) between the main channel, the air conduits, and the lens channels served as the designated pinning positions for the lens droplets. The volumes and flow rates of air or DI water injected to the channel networks were controlled by syringe pumps (270810C, Cole-Parmer, Vernon Hills, IL, USA), and the pressure in each air conduit was monitored by pressure sensors (142PC30D, Honeywell, Morristown, NJ, USA). The inlets of the microfluidic channel network (I0, I1, I2 and I3) were connected to the syringe pumps via vinyl tubings (1/32 inch inner diameter, 3/32 inch outer diameter, Cole-Parmer Vernon Hills, IL, USA). For two lenses, four syringe pumps and three pressure sensors were used to allow for individual and independent tuning of each lens. As the formation and tuning process of each microlens is de-coupled, it is highly possible to integrate multiple microlenses into an array. Each lens in the array would require one syringe pump and one pressure sensor. Hence, for an n-lens array, n+2 syringe pumps and n+1 pressure sensors (including the main channel) would be needed.

The dimensions of the channel network for two microlenses, as shown in figure 1, are listed as follows. The width of all channels was 1 mm, except for that of the lens channels between J2 and J3, and between J4 and J5, which was 0.75mm. The distances between J1 and J2, J2 and J3, J3 and J4 and J4 and J5 were 2.5, 1, 3 and 1 mm, respectively. The depths of the channels were kept uniform at 250μm. DI water (dyed in green for easy observation) was prepared in a syringe and delivered though I0, while air was also kept in syringes and infused or withdrawn through I1, I2 and I3. The outlet of each air conduit was also connected to a waste reservoir through a controlling valve. Each inlet or outlet had a valve (inlet valves IV0, IV1, IV2, IV3 and valves V1, V2 and V3). The pressure sensing range and the sensitivity of the pressure sensors were 0-30 lbf/in^2 and 166.7 mV/(lbf/in^2), respectively.

4.2.3 Fabrication of microfluidic channels

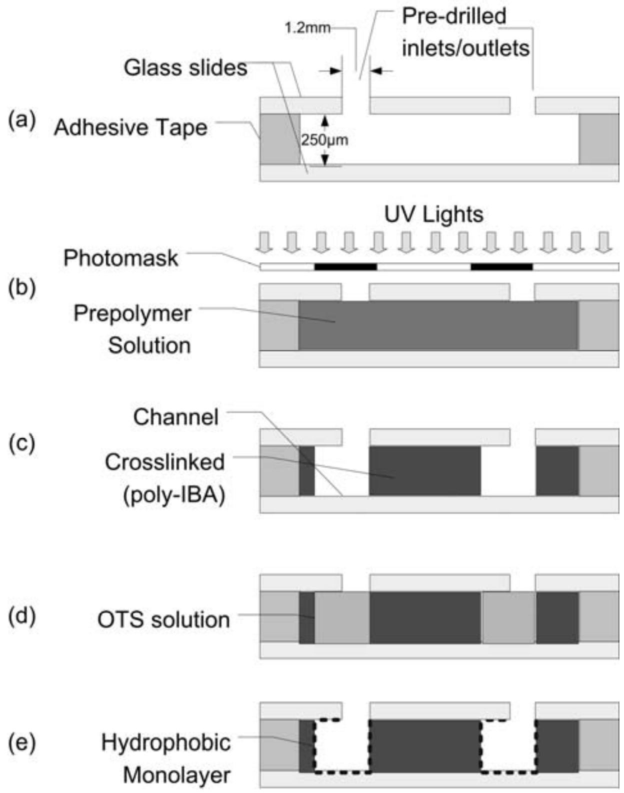

Figure 4-2. Fabrication process of microfluidic channels using LP^3 based on UV photolithography with a single photo mask.

The microchannel network was fabricated through a single mask liquid-phase photopolymerization (LP^3) process without the need for a clean room [32–34]. The photosensitive prepolymer solution used to form the channels was isobornyl acrylate (IBA). The solution consisted of three constituents in the following ratios: 31.66: 1.66: 1.0—monomer:IBA, crosslinker: tetraethylene glycol dimethacrylate (Sigma-Aldrich, Inc., St. Louis, MO, USA) and photoinitiator:2,2-dimethoxy-2-phenylacetophenone (Sigma-Aldrich, Inc., St. Louis, MO, USA). As shown in Figure 4-2(a), a chamber was created by attaching a polymer fluidic cartridge (Grace Bio-Labs, Bend, OR, USA) onto a pre-cleaned glass slide. The depth of the chamber was

250μm. The inlets and outlets of the device (1.2 mm in diameter) were previously drilled on the cartridge with a mechanical driller. To improve the adhesion between the cartridge and the glass, the device was baked on a hot plate at 50 ºC for 5 min. Then, the IBA-based prepolymer was flowed into the chamber and degassed for 10 min to remove bubbles. Afterwards, the microchannels were patterned inside the chamber by exposing it under an ultraviolet (UV) light (A4000, EXFO, Mississauga, Ontario, Canada) with an intensity of 7.8 mW cm^{-2} for 24s, using a single photo mask film (Imagesetter Inc.,Madison, WI, USA) [Figure 4-2(b)]. The device was then developed in a bath of ethanol for 100s, then dried by nitrogen flow [Figure 4-2 (c)]. For the purpose of surface chemical treatment, an octadecyltrichlorosilane (OTS) solution diluted by hexadecane [0.15% (v v^{-1})] was flowed into the microchannels through an inlet and filled the whole channel for 3 min. After that, a peristaltic pump was used to flush away the solution, followed by flushing with a massive amount of isopropanol and drying. Thus, a self-assembled monomer hydrophobic layer was formed on the top surface, bottom surface and sidewalls of the channels, as shown in Figure 4-2 (e).

Compared to our previously reported fabrication approach, this modified process has several advantages. Instead of creating the chamber with two hard glass slides, the use of the flexible polymer cartridge greatly improved the adhesion between the cross-linked IBA and the inner top surface of the chamber, thus improving the air tightness of the fabricated device. Instead of using a massive amount of methanol to flush away the OTS/ hexadecane solution, we used a peristaltic pump to exhaust the solution first, thus preventing the contact of alcohol with hexadecane phase, which might cause the alcohol self-association phenomenon [35], forming aggregates that clog the microscale channels.

4.2.4 *In Situ* formation of the liquid microlenses

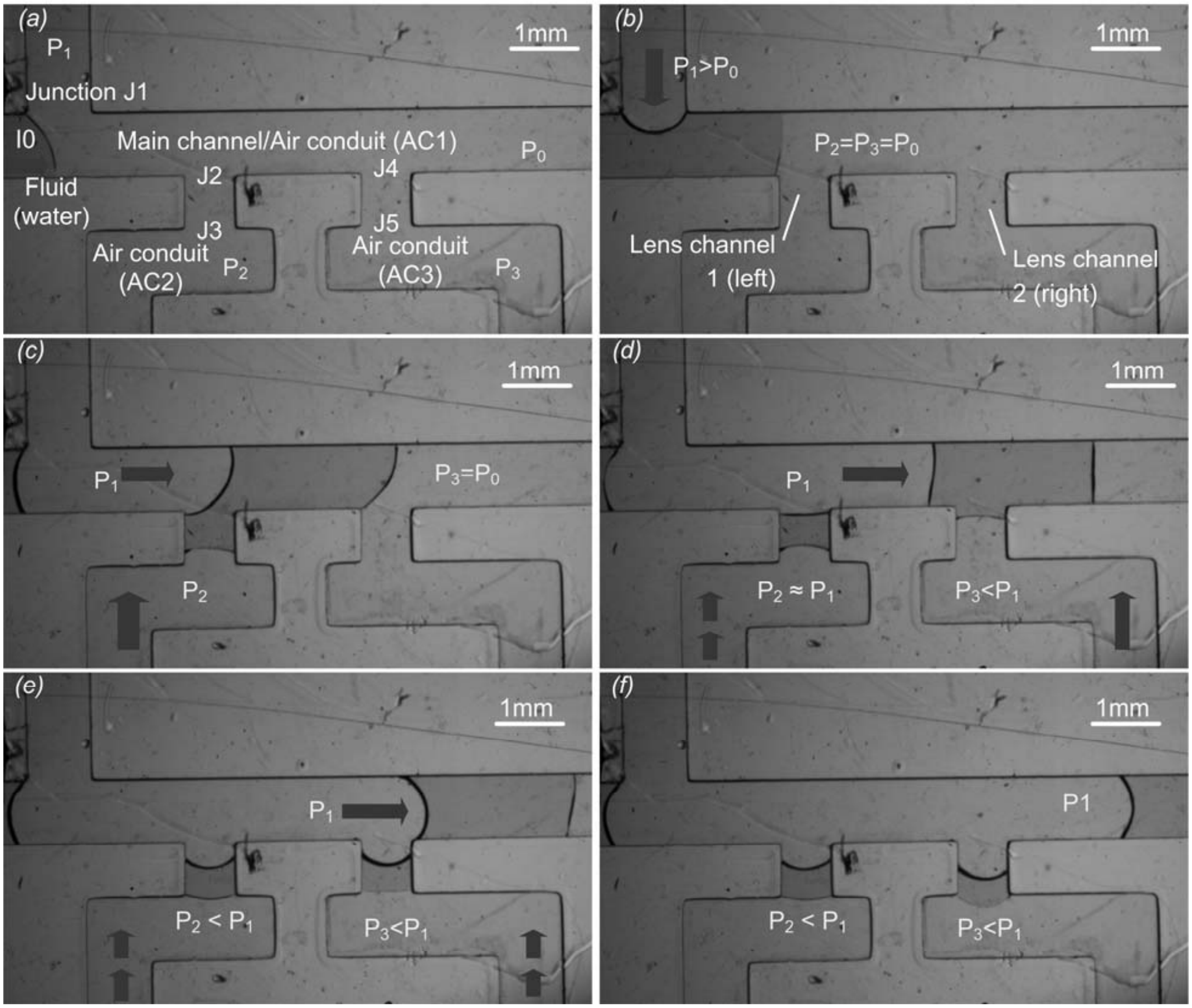

Figure 4-3. *In situ* formation process of two microlenses within the microchannel network. DI water was dyed green for easier observation

Figure 4-3 shows the formation process of two liquid microlenses. At the beginning, all inlet valves (IV0, IV1, IV2 and IV3) and V1 were open, while V2 and V3 were closed. As a result, the initial air pressure in the channels was set at P_0 = 1 atm. A bulk fluid (DI-water, dyed green) was injected through I0 [Figure 4-3(a)] with a flow rate of 5 μL min^{-1}. After the fluid passed junction J1, the air pressure in air conduit AC1 was gradually increased in steps of 10Pa, by periodically infusing air with a flow rate of 4.7 μL min^{-1} through I1 [Figure 3(b)]. The air infusion was paused for 10 s between each infusion step to balance the pressure in the channel. As a result, a small droplet of the fluid was segmented from the bulk fluid. It was found that for this device, a minimal air pressure of $P_1 = P_0$+390Pa was needed to completely cut and begin to drive a droplet of ~0.88μL in the main channel. With the increase in P_1, the droplet arrived at junction J2 and split at J2. A small portion of the droplet was left in the channel from J2 to J3, while a larger portion of the droplet was further driven towards J4 [Figure 4-3(c)]. As discussed in [30], the volume ratio of the smaller portion to the larger portion was proportional to the air pressure difference ratio $(P_1–P_2)/(P_1–P_0)$. Air infusion through AC1 was then paused and P_1 was maintained at ~P_0+900Pa, and an air plug was infused through AC2 to increase P_2 to P_0+750Pa, leaving 0.15μL of water between J2 and J3 and forming a lens droplet.

Air infusion through AC1 was then restarted and the split was completed after P_1 was increased to ~P_0+930Pa. The remaining droplet in the main channel was further driven by P_1 towards J4 [Figure 4-3(d)]. A similar splitting process occurred after P_1 was increased to ~P_0+2020Pa [Figure 4-3(e)]. P_3 was adjusted to P0+1660Pa so that 0.13μL of water was left between J4 and J5, forming another lens droplet.

To prevent the pressure differences between the two air–liquid interfaces of the droplet at J3 from exceeding the critical pressure difference (the pressure difference above which the droplet tends to be pushed to leave the junction; theoretical value: 219Pa [31], experimental value: 217±4Pa), $\Delta P_{12} = P_1-P_2$ was kept below 210Pa, by air infusion through AC2 after each increasing step of P_1. For the same reason, P_3 was increased immediately after splitting to P_0+1830Pa and ΔP_{13} was kept below 210Pa. Figure 4-3(f) depicts the final stage of the formation process of the lenses. P_1 was about P_0+2180Pa. The profile of each lens can also be tuned pneumatically, which will be discussed in the next section. After the formation of the lenses, all the valves at the inlets and outlets were closed and thus the channel network was sealed. The chip with the microlenses could then be detached from the syringe pumps for storage or transfer. The shelf life of our microlenses device, using DI water as the lens liquid without refined air-tight package, is approximately one week before the volume of the lens droplets significantly decreases due to evaporation.

4.2.5 Tuning the Liquid Microlenses in the Array Separately

After the lens droplets were delivered to the lens channels (channels between J2 and J3, J4 and J5, etc), the shape of the microlenses can be tuned by adjusting the pressure difference across their air-liquid interfaces. As shown in Figures 4-4(a), (b) and (c), one of the lens droplets was pinned at junction J4, forming a positive meniscus lens, since the pressure difference across its two surfaces remained at 132.3Pa, and the curvature of the lens droplet was held still. Meanwhile, the air pressure difference across the two surfaces of the lens droplet in the left lens channel (between J2 and J3) was decreased from 216.6 [Figure 4-4(a)] to 0.9Pa [Figure 4(b)] by decreasing P_2; thus, the interface pinned at J2 changed its shape from convex to almost planar. Consequently, the focal length of the microlens in the left channel increased from 0.972 mm (calculated; see discussion in section 3.3) to almost infinity. Further decrease in the pressure difference caused P_1 to be larger than P_2, and the lens droplet was pushed away from J2 and instead pinned at J3, forming another plano-convex lens [Figure 4-4(c)]. Similarly, Figures 4-4(d).(f) show the tuning process of the lens droplet in the right lens channel (between J4 and J5) by decreasing P_3, while keeping the lens in the left lens channel unaffected.

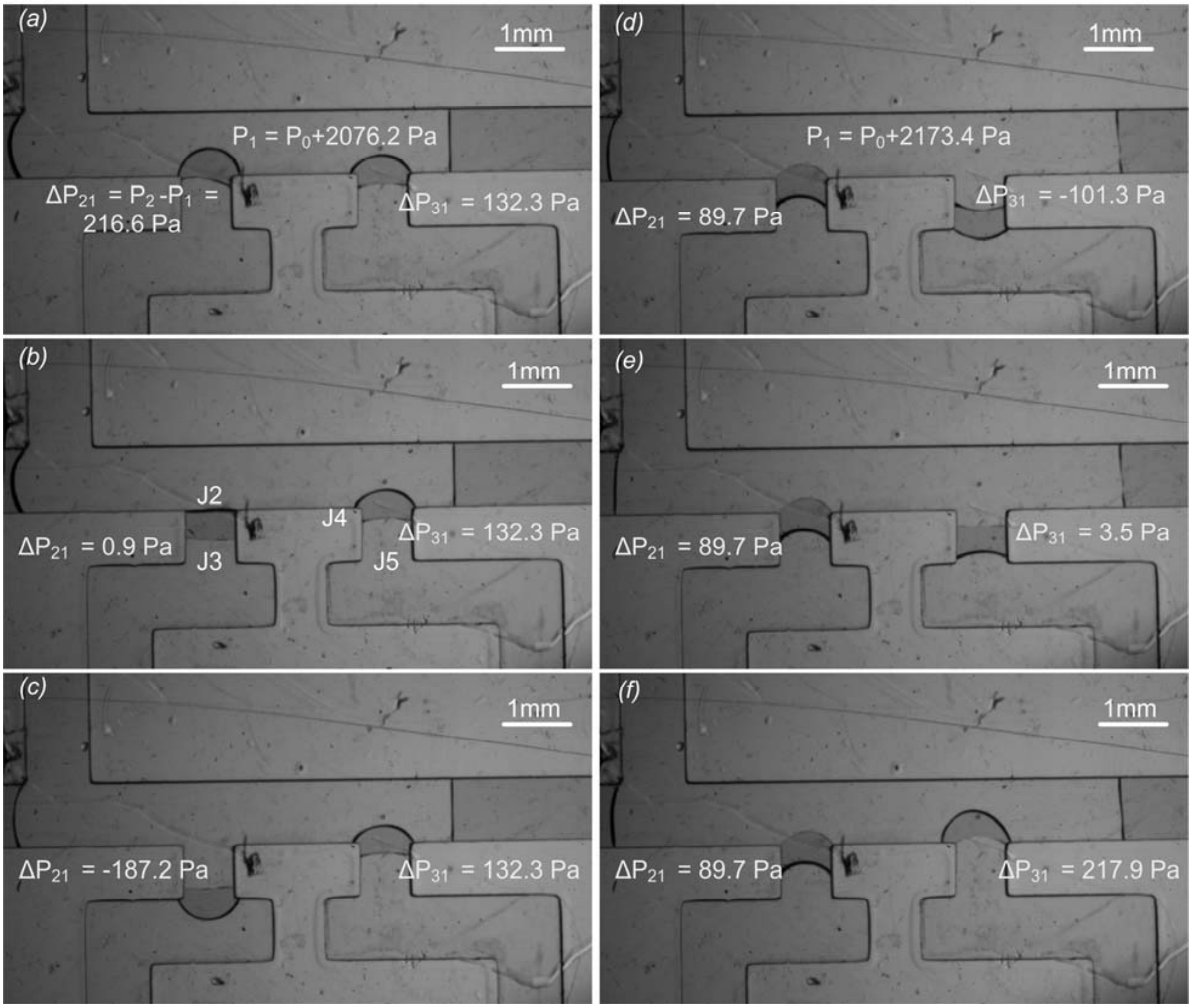

Figure 4-4. Individual tuning of each liquid microlens without affecting the other one.

The relationship between the focal length of the microlenses and the pressure difference across the lens droplet interfaces is plotted in Figure 4-5. As expected, the focal length decreased rapidly with the increase in the pressure difference, as the increase in the pressure difference caused the decrease in the radius of curvature of a lens droplet. The focal length was approximately inversely proportional to the pressure difference, as indicated by the Young-Laplace equation (see section 3.2 for detail).

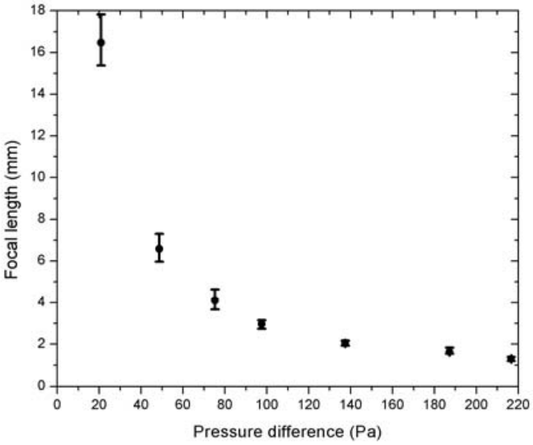

Figure 4-5. Relationship between the focal length of the microlenses and the pressure difference across the interfaces of the lens droplets. Pressure difference was recorded by monitoring the pressure sensors, while the profiles of the corresponding microlenses were recorded and parameters were fitted into a commercial simulation software to calculate the focal lengths (more details in section 3.3).

An important factor affecting the shape and the tuning of the microlenses is the contact angle of the droplet at different surfaces. The profiles of water droplets on glass, poly-IBA and cartridge treated by OTS as mentioned above were examined by a goniometer (OCA 5, Data Physics Instruments GmbH, Filderstadt, Germany) [30], and the contact angles were all estimated to be 90º. However, due to the hysteresis phenomenon of contact angles, this value was not absolute. There are also several non-ideal factors that affect the contact angle, such as the roughness of the channel surfaces and the quality/uniformity of the OTS monolayer on the surfaces. However, based on our observation and measurement by the goniometer, at the quasi-steady state, while only one interface was "pinned" at a junction [such as the lenses in Figures 4-4(b) and (c)], the contact angle of the droplet was within the range of 85º-90º. Thus, for simplicity, we will assume the contact angle of the water droplets on the surfaces to be 90º in following experiments and simulations.

The shape of the liquid-air interface of a lens droplet, which is pinned at a junction of a lens channel, is determined by the Young-Laplace equation (see section 3.2). Meanwhile, theoretically, the shape of the other "unpinned" liquid-air interface depends on the static contact angle of the liquid on the channel material under homogeneous pneumatic pressure [30, 31]. This can be confirmed by a 2D computation fluidic dynamic simulation, discussed in section 3.1. However, situations were more complicated in the 3D experimental case. Since the tuning process was transient, the flow rate and the pneumatic pressure were not always homogeneous. The hydraulic pressure in the droplet was also largely uneven either. Thus, the shape of the other liquid-air interface, which was supposed to be flat, could be distorted during the pneumatic tuning process. As a result, instead of plano-convex microlenses, positive meniscus lenses were sometimes obtained. More analysis and experiments are needed to determine the condition needed to form plano-convex lenses and positive meniscus lenses.

4.2.6 Removal and reformation of the microlenses

One of the unique properties of the fabrication process and control scheme of our lenses was that the lenses can be removed individually and on demand. As shown in Figures 4-6(a)-(c), keeping P_1 and P_3 unchanged while increasing P_2, the lens pinned at J2 was gradually pushed out after the pressure difference ΔP_{21} exceeded the critical pressure (219Pa), and was eventually removed from the junction. Meanwhile, the other lens at J4 was unaffected. Another notable feature of our microlenses is that it provides a simple yet controllable way to remove all lenses in the microchannel network on demand. This was achieved by decreasing the pressure P_1 in AC1, while adjusting the pressure in other ACs. As shown in Figures 4-6(d)-(f), P_1 was decreased from ~P_0+1950Pa to ~P_0+870Pa and then to ~P_0+20Pa in steps of 10Pa each, by withdrawing the air in AC1 at a rate of 4.7 μL min^{-1}. The syringe pump was paused for 10s between each step of withdrawal so as to keep the liquid quasi-stationary. When the droplet was moving along J4, P_3 was kept larger than P_1 to ensure that no liquid was left in the lens channels. Similarly, P_2 was kept larger than P_1 when the droplet was moving along J2. At the end of the withdrawal process, both microlens droplets were removed from the lens channels. This removal of the microlenses is complete as it would not leave any residual liquid except in the main channel, and thus did not require a subsequent cleaning process, which might introduce complexity to the air tightness of the system. We then re-formed two lenses with a similar process as described in section 4.2.4. This time we adjusted P_2 and P_3 so that the liquid volume left in the lens channels was ~0.16μL. The whole process was shown in Figures 4-6(g)-(i).

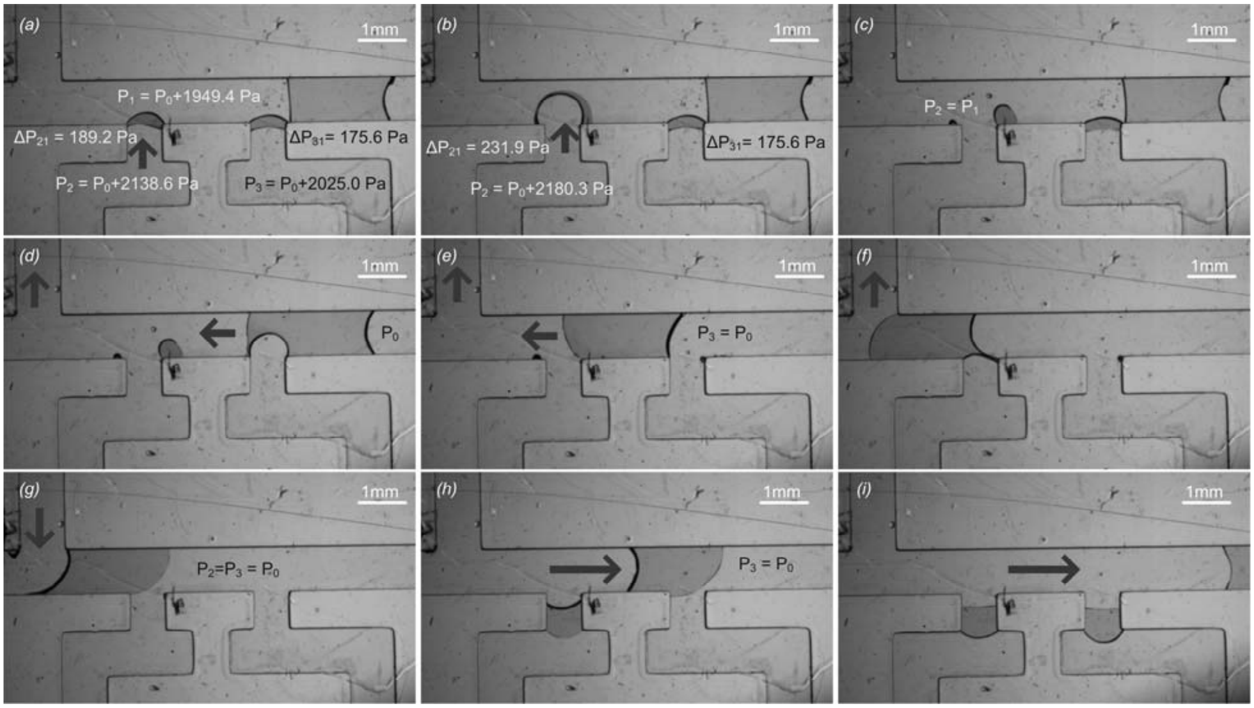

Figure 4-6. (a)-(c) Removal of a liquid microlens at J2 without affecting the other lens pinned at J3. (d)-(f) Removal of both of the microlenses. (g)-(i) Formation of new microlenses.

4.3 Characterizations and simulations

4.3.1 Tuning of the microlens profiles

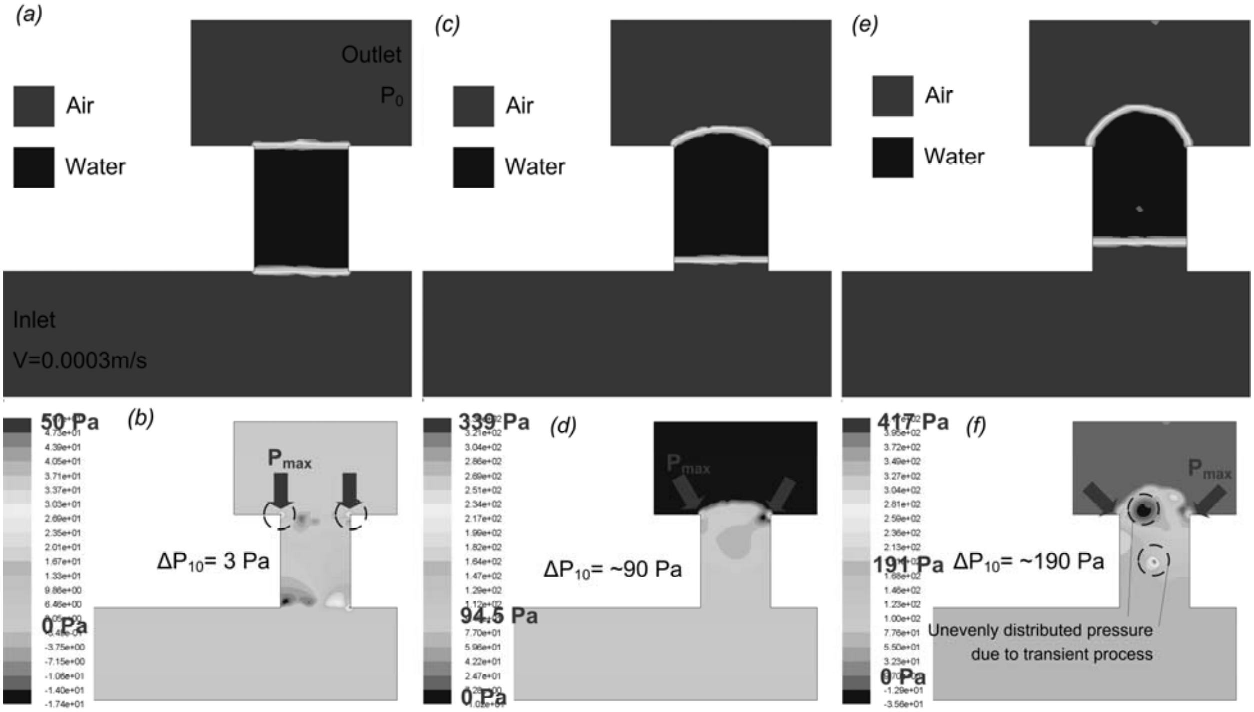

Figure 4-7. CFD simulation results of a microlens droplet in a channel network, pinned at a junction. (a), (c), (e) The shape change of the droplet with the increasing pressure. (b), (d), (f) The pressure distribution in the channel network.

To investigate the relationship between the shape of the pinned microlens and the pressure difference across the interfaces of the lens droplet, a computation fluidic dynamic (CFD) simulation was performed with ANSYS Fluent ® (version 12.0, ANSYS, Inc., Canonsburg, PA, USA). Instead of simply evaluating the shape of one interface of the droplet using Young-Laplace equation, to accurately relate the pressure distribution inside the whole channel with the shape of the microlens from the top view, the simulation was performed as a transient analysis using a volume of fraction (VOF) model. To simplify the problem, the simulation was performed in 2D and the results are shown in Figure 4-7. Consistent with the real case, a channel network with two air conduits (width: 1mm) and a lens channel (width: 0.75 mm) in between was defined, and one of the air conduits had an inlet while the other had an outlet. The interacting liquid phases in this simulation were water and air, and the surface tension between them was set to be 75.64dyn cm^{-1}. The contact angle between water and the channel walls was set to be 90º. At time instant 0, a droplet (0.1875µL) was set to reside in the lens channel, and an air flow with a velocity of 0.0003m s^{-1} (corresponding to a volume velocity of 4.7µL min^{-1}) was injected into the network through the inlet, while the pressure at the outlet was kept at 1 atm. during the whole simulation process. Figures 4-7(a) and (b) depict the lens shape and the pressure distribution in the channel after 10ms of injection, where the surfaces were yet to change owing to the small pressure difference (only around 3Pa). However, with the accumulation of the air in the inlet, the pressure in the air conduit with the inlet increased, pushing the lens droplet out of the lens channel. Combined with the pinning effect at the junction, the droplet protruded out and presented a convex lens. Figures 4-7(c) and (d) demonstrated this phenomenon. When the pressure difference approached 90Pa after 2.4s of injection, the radius of curvature of the lens was approaching 0.92mm (calculated from the profile of the liquid interface). After 6s of injection, the pressure difference reached 190Pa and the radius of curvature of the lens further decreased. According to figures 7(b), (d) and (f), the inner pressure of the droplet was increasing with the accumulation of the air, and the pressure difference across the “unpinned” liquid-air interface was very small. The inner pressure of the droplet experienced a slow decrease from the "unpinned" interface to the "pinned" interface, while the liquid-air pressure decreased abruptly across the "pinned" interface, as expected. The region with the largest pressure (pointed by arrows) appeared at the pinned edge of the droplet. Then, the air injection was stopped (air flow rate was set to 0), and after 800ms, the shape of the droplet stopped changing, and we can consider that the quasi-steady state of the droplet was achieved. However, in the experiment where it is 3D in nature, according to our observation, it took much longer (10s or more) for the droplet to experience small shape transitions and reach its quasi-steady state. Note that since the simulation uses a VOF model, the colorful boundary between water and air indicates the rapid change in the volume fractions of the two phases at the interface. Also note that the simulation was transient. Hence, Figures 4-7(b), (d) and (f) show a transient pressure distribution, which is not homogeneous, and, as a result, the surfaces of the water droplet do not appear as smooth as those in the static state.

4.3.2 Effect of gravity

At the micro scale, gravity is generally dominated by surface tension and thus the shape of an air-liquid interface of a microlens droplet is determined by Young-Laplace equation [36]:

$$\Delta \mathrm{P}=\gamma(\frac{1}{R_1}+\frac{1}{R_2}) \qquad (4.1)$$

where ΔP is the pressure drop across the interface, γ is the liquid-surface free energy, and R_1 and R_2 are the principal radii of curvature of the interface. R_1 corresponds to the "top view" of the air-liquid interface of a lens droplet, while R_2 corresponds to the "cross-section view" along the optical axis of the lens droplet. Ignoring the effect of gravity and assuming fixed height of the channel, R_2 is inversely proportional to the contact angle of the liquid on the substrate (in our case, 90º). Thus, $1/R_2$ equals to 0 and R_1 has a simple relationship with ΔP:

$$R_1 = \gamma / \Delta P \qquad (4.2)$$

Equation (4.2) is only valid if the effect of gravity can be ignored. If the gravity effect is comparable to the surface tension and pressure difference, R_2 cannot be considered to be solely dependent on the contact angle at the liquid-substrate interface. A simulation using Surface Evolver (version 2.50, free software developed by Ken Brakke, Susquehanna University, Selinsgrove, PA, USA, available from http://www.susqu.edu/brakke/evolverevolver.html) is used to elucidate this effect and the results are shown in Figure 4-8. We focused on examining the relationship between the heights of the droplets and the shapes of the free surfaces of the lens, when gravity is taken into account.

To adapt to the algorithm used by Surface Evolver, the problem was simplified to determine the shape of a free surface by the principle of minimum energy, considering the effect of gravity and other boundary conditions and constraints. To this end, a lens droplet in a lens channel with 1/3 of its volume protruding out of the channel and pinned at the junction was considered. The surfaces of the droplet inside the channel [confined in the framework of the solid red lines in Figure 4-8(a)] were set to be stationary in all three dimensions, while the displacement degrees of freedom of the surface of the lens protruding out of the junction (depicted by the framework of the spotted red lines) were not confined. The contact angle between the liquid and the inner channel surface was set to be 90º, the density of the liquid was set to be 1kg m^{-3}, and the gravity was set to be 9.81m s^{-2}. Here, gravity was the only parameter of interest; thus, the pressure within the liquid lens body and the pressure difference across the surfaces were not considered as constraints. The free surface evolved from a cuboid to the ultimate surface with the minimal free energy, as shown in Figure 4-8. Comparing Figures 4-8(a) and (c), gravity effect can be neglected when the height of the lens droplet is low [0.5mm in Figure 4-8(a)], and $1/R_2$ can be considered as 0. When the droplet height increases [Figures 8(b) and (c)], under the gravity effect, the shape of the free surface is distorted and cannot be considered as perpendicular to the substrate, which affects the optical property of the liquid lens. Observing the shapes of the free surfaces of lenses with different heights, an empirical threshold of the height of the microlens was determined to be 0.73mm to avoid distortion. At this height, the maximum deviation from the vertical line on the principal plane was estimated to be 0.01mm; thus, R_2 can be estimated to be 6.67mm. Similarly, R_2 approached 6.02 mm when the height of the droplet approached 1.20mm.

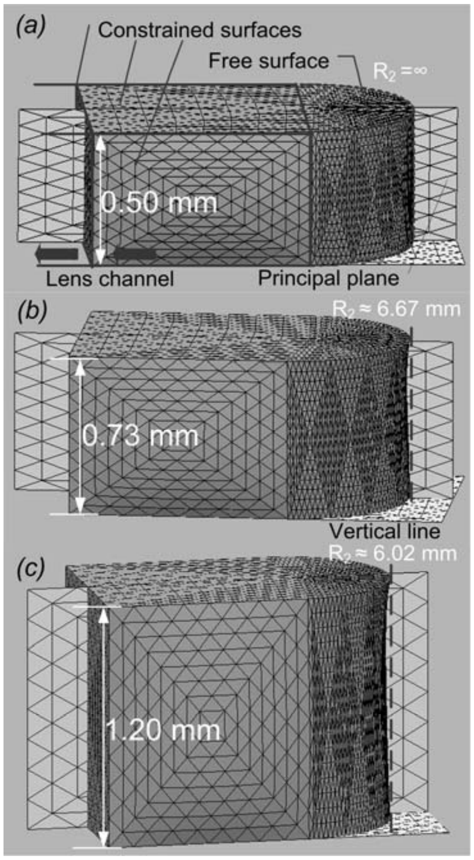

Figure 4-8. Simulation results of the steady state of cylindrical microlenses with different heights: (a) 0.50 mm, (b) 0.73 mm and (c) 1.20 mm. The distortion of the free surface was depicted by the principal plane intersecting the surface, and comparing the intersecting line with a line perpenticular to the substrate.

4.3.3 Optical characterization

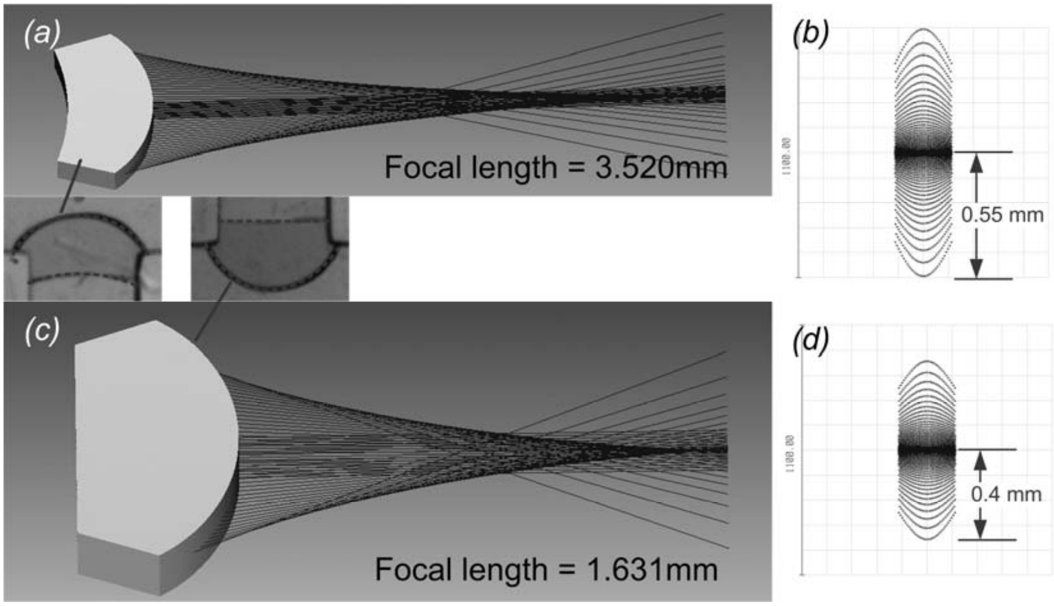

Figure 4-9. Ray-tracing simulation results of two cylindrical liquid microlenses. (a) Ray diagram of a postive menisci lens whose profile matches the lens pinned at J4 in Figure 4-4(c). (b) Spot diagram of the lens in (a) at its focus. (c) Ray diagram of a plano-convex lens matching the profile of the lens pinned at J3 in Figure 4-4(c). (d) Spot diagram of the lens in (c) at its focus.

To investigate the optical properties of our lenses, a ray-tracing simulation was carried out using Zemax$^{®}$ (Radiant Zemax, Redmond, WA, USA). The results for two lenses are shown in Figure 4-9 as examples. The profiles and dimensions of the lenses were measured from the fabricated lenses, and parameters such as radii of curvature of the interfaces were fitted from the obtained profiles. Here we focused on convex lenses. Two types of convex lenses were found among our microlenses: (1) positive meniscus lenses with one convex and one concave surfaces, with the radius of curvature of the convex surface being smaller than that of the concave surface; (2) plano-convex lenses with one convex surface and one planar surface. Figures 4-9(a) and (b) show the ray-tracing diagram and spot diagram of one positive meniscus lens, whose profile matches the lens at J4 in Figure 4-4(c). The lens had a radius of curvature of 0.569 mm for the convex surface, a radius of curvature of -0.975 mm for the concave surface, and a thickness of 0.524 mm. Therefore, it had a focal length of 3.52 mm and a lateral aberration of 0.55 mm. For the plano-convex lens at J3 in Figure 4-4(c), its focal length was simulated to be 1.631 mm and the lateral aberration was simulated to be 0.4 mm.

4.4 Enhancing fluorescence emission in a microfluidic channel using lateral tunable liquid microlenses

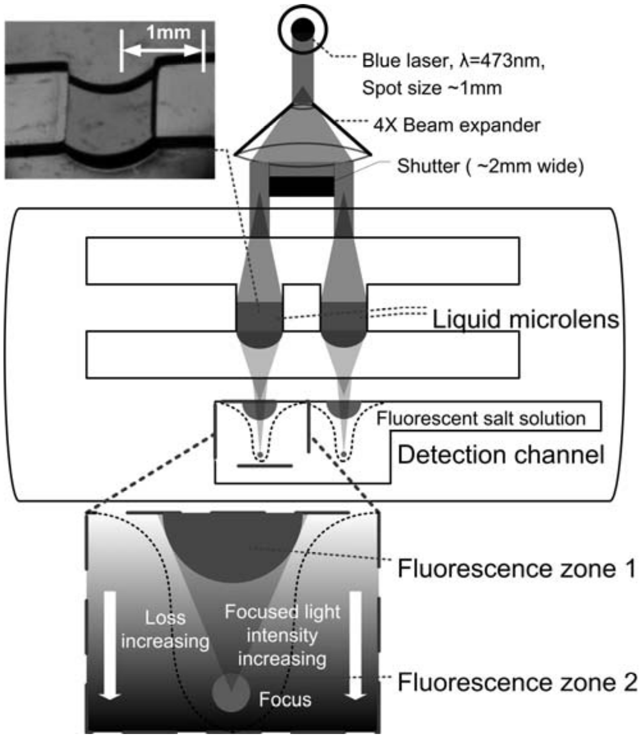

Figure 4-10. Setup for the experiment of using tunable lateral microlenses to enhance fluorescence emission in a microchannel.

It is a prevailing method to utilize fluorescence signals in LoC applications [8, 37, 38]. Conventionally, LoC chips containing the fluorescent materials, the stimulating light source and the fluorescence detection equipments are arranged in different vertical physical layers. However, this layout, as discussed before, may consume large spaces and introduce complexities in the miniaturization and integration. This problem can be alleviated if the stimulating light can be introduced from the lateral direction. However, the loss due to the sidewalls of the microfluidic channels or the mismatch in the coupling of optical fibers might greatly attenuate the stimulation light, thus affecting the feasibility of this design. By re-focusing the diffused/scattered light beam, our microlenses, however, provide an effective and controllable way to compensate for the attenuated stimulating light and to enhance the fluorescence emission.

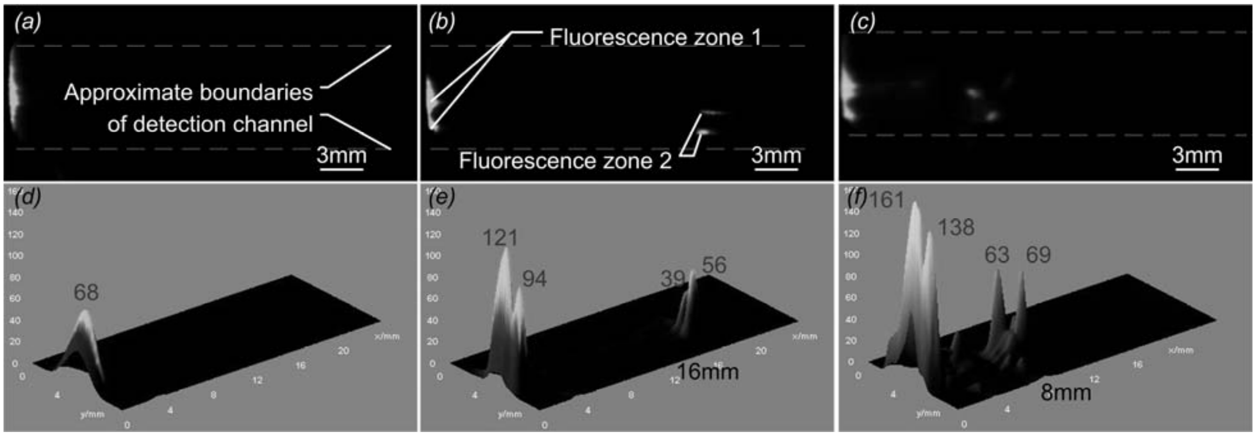

Figure 4-11. (a)-(c) Fluorescence response of a fluorescein sodium salt solution in the detection channel, corresponding to different focal lengths of the two microlenses, and (d)-(f) intensity of the fluorescence signal, represented by the local luminance of the image.

To demonstrate this, an experiment of enhancing the fluorescence signal using our microlenses was performed (Figure 4-10). The channel network to form the microlenses and a detection channel filled with fluorescein sodium salt solution (10 μM in DI water) were integrated on the same glass slide. Two microlenses (Figure 4-10, left corner) were formed through the process described in section 4.2.3. A blue laser (Laserglow Inc., Toronto, Canada, tunable intensity from 0~30 mW, spot size: ~1 mm) was used as the stimulating light source. The light beam was introduced into the microfluidic chip from a lateral direction. The laser beam was expanded with a 4× beam expander (Newport, Irvine, CA, USA), and partially blocked by a shutter in the middle, in order to produce two laser beams with a width of ~1 mm to provide the light simultaneously to both microlenses. The beams (intensity before entering the chip: ~1.2 mW) passed through a layer of poly(IBA) sidewall and were focused into the detection channel by the microlenses. The fluorescent image was taken by a fluorescence microscopy camera (SMZ1500 with fluorescence module, Nikon, Melville, NY, USA). Due to the loss along the optical path in the detection channel, strength of the fluorescence signal would decrease rapidly. As a result, only a small zone close to the incoming light (labeled as "fluorescence zone 1" in Figure 4-10) exhibited visible fluorescence response without a lens or with a lens with a focal length of infinity [Figure 4-11(a)]. However, with the focusing power of the microlenses, the area of the zone with visible fluorescence responses was enlarged and showed a stronger fluorescence emission, and the regions near the focused points of the microlenses (labeled as "fluorescence zone 2" in Figure 4-10, whose positions were adjustable) also showed visible fluorescence responses. By pneumatically adjusting the pressure difference across the interfaces of the lens droplets, thus changing the focal length of the microlenses, the area and intensity of the fluorescence zones could be controlled, as shown in Figures 4-11(b) and (c). The focal length of the two lenses were tuned to approach infinity at first [Figure 4-11(a)], then to 16.7 mm [Figure 4-11(b)], and then to 6.9 mm and 8.1 mm, respectively [Figure 4-11(c)]. The corresponding maximum fluorescence emission (described by the local luminance in the image) in fluorescence zone 1s was increased from 68 [Figure 4-11(d)] to 121 [Figure 4-11(e)], then to

161 [Figure 4-11(c)], indicating the enhancement of fluorescence signal. The fluorescence zone 2 of each microlens could be moved separately [comparing Figures 4-11 (b) and (c)] by individually tuning the focal length of the microlenses. In doing so, the detection channel can be scanned along the optical axes of the microlenses, which could give a more detailed information about the distribution of the fluorescence labeled analytes in the channel. Fluorescence zone 1 of one microlens was observed under a high magnification to study the relationship between the focal length of the microlenses and the properties of fluorescence zone 1 (Figure 4-12). To provide a more comprehensive view, parts of the lens channel and the lens droplet were also included in the images (the lens facet was depicted by the blue stimulating light scattered at the air-liquid interface). When there was no lens, or when the liquid lens had a focal length approaching infinity, only a small region (0.014 mm^2 in area, calculated from the fluorescence image, through the measurement module of ImageJ (open source software developed at National Institutes of Health, available at http://rsbweb.nih.gov/ij/), by estimating the ratio between a pixel and the area of real space, and then counting the pixels with an image luminance larger than 10) near the detection channel sidewall showed visible fluorescence response [Figure 4-12(a)]. Figure 4-12(b) shows the situation when the focal length was decreased to 18.7 mm, and the resultant area of the fluorescence zone 1 was increased to 0.097 mm^2. When the focal length was further decreased to 3.5 mm [Figure 4-12(c)], the area of fluorescence zone 1 was increased to 0.181 mm^2, which was 13 times larger than that without a convex microlens. Considering a 0.3 mm × 0.3 mm region near the sidewall of the detection channel (pink square "**R**" in Figure 4-12), without microlenses, fluorescence-labeled analytes inside this region could not be examined due to insufficient stimulating light. However, with the focusing of a tunable liquid microlens with a

focal length of 3.5 mm, most of the analytes inside **R** can be stimulated by the blue light. Taking a point "**A**" at the right corner of "**R**" as an example, fluorescence signal strength at **A** was increased from 4 to 61 then to 152, increased by 38 times, with the decrease in the microlens focal length.

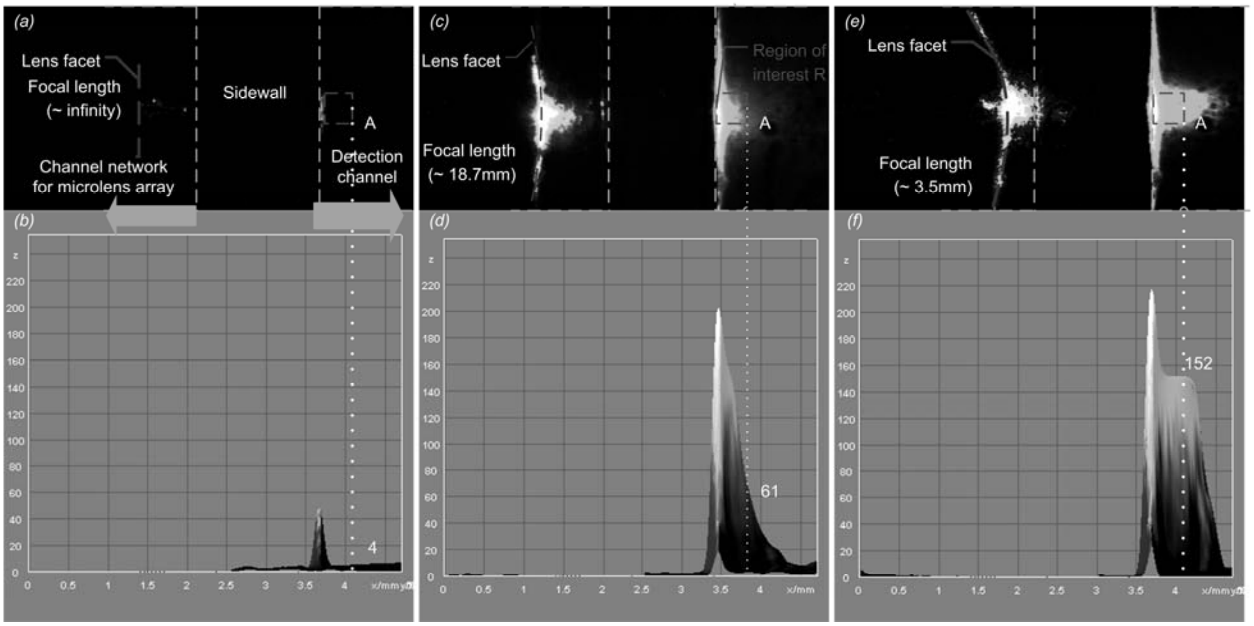

Figure 4-12. (a), (c), (e) Images of the microlens in its channel (left part) combined with the fluorescence image in the detection channel (right part). The sidewall between the two channels was marked by golden dashed lines. The lens facet (fitted by red dashed lines) can be observed from the scattered blue stimulating light. A region of interest "R" near the detection channel sidewall (in fluorescence zone 1) was marked by pink dashed line, with its right lower corner annotated as "A". (b), (d), (f) The intensity of the fluorescence signal, represented by the local luminance of the image, corresponding to (a), (c), (e), respectively.

4.5 Conclusion

We have demonstrated lateral tunable liquid microlenses in situ formed in microchannel networks through pneumatic control. An optimized fabrication process was developed, and two microlenses were formed through pneumatic control. By adjusting the pressure differences across the interfaces of the microlens droplets, the lenses in the assembly can be individually tuned in focal length, removed, and re-formed on demand. Through simulation, the relationships between the profile/shape of the fabricated microlenses and factors such as pressure and gravity were examined. The optical properties of the lenses were also examined through a ray-tracing simulation. The potential applications of our microlenses in lab-on-a-chip applications were also demonstrated by using it to enhance the fluorescence emission in an integrated detection channel. By tuning the focal length of our microlenses, the area of the fluorescence zones can be greatly enlarged (by 13 times), and the fluorescence signal can be effectively enhanced (by up to 38 times).

Future works include the optimization of the microlenses design and extending its applications. We will first integrate more microlenses into a single array and evaluate the limit in the number of microlenses in such an array. Secondly, we will integrate multiple liquid microlenses in one lens channel, which aligns the microlenses into a 2D array for more flexibility. Thirdly, more investigation will be carried out to determine when a pinned droplet will form a positive meniscus lens and when it will form a plano-convex lens. Then, we will also design and conduct more experiments to experimentally characterize the optical properties, such as the spherical aberration and coma of the microlenses, analyze the results, and compare them to the simulation results. Further, we will realize tracking of fluorescent particles in a microfluidic channel with the 2D-scanning capability of our microlenses.

4.6 References

[1] Y. Fainman, L. P. Lee, D. Psaltis and C. Yang, *Optofluidics: Fundamentals, Devices, and Applications*, New York: McGraw-Hill, 2009.

[2] Z. Y. Li, Z. Y. Zhang, T. Emery, A. Scherer and D. Psaltis, *Optics Express*, vol. 14, pp. 696-701 (2006).

[3] D. B. Wolfe, R. S. Conroy, P. Garstecki, B. T. Mayers, M. A. Fischbach, K. E. Paul, M. Prentiss and G. M. Whitesides, *Proceedings of the National Academy of Sciences, USA,* vol. 101, pp. 12434–12438 (2004).

[4] J. C. Roulet, R. Volkel, H. P. Herzig, E. Verpoorte, N. F. de Rooij and R. Dandliker, *Optical Engineering,* vol. 40, pp. 814–821 (2001).

[5] J. Hubner, K. B, Mogensen, A. M. Jorgensen, P. Friis, P. Telleman and J. P. Kutter, *Review of Scientific Instruments*, vol. 72, pp. 229–233 (2001).

[6] J. M. Jang, H. J. Shin, S. W. Hwang and E. G. Yang, *Sensors and Actuators B*, vol. 108, pp. 993–1000 (2005).

[7] K. Carlson, M Chidley, K. B. Sung, M. I. Descour, A. Gillenwater, M. Follen and R. Richards-Kortum, *Applied Optics*, vol. 44, pp. 1792–1797 (2005).

[8] S. Camou, H. Fujita and T. Fujii, *Lab on a Chip*, vol. 3, pp. 40–45 (2003).

[9] J. R. Wendt *et. al., Journal of Vacuum Science & Technology B*, vol. 17, pp. 3252–3255 (1999).

[10] J. Seo and L. P. Lee, *Sensors and Actuators B*, vol. 99, pp. 615–622 (2004).

[11] H. H. Yang, C. K. Chao, M. K. Wei and C. P. Lin, *Journal of Micromechanics and Microengineering*, vol. 14, pp. 1197–1204 (2004).

[12] P. Savander, *Optics and Lasers in Engineering*, vol. 20, pp. 97 (1994).

[13] J. Wenger, D. G´erard, H. Aouani and H. Rigneault, *Analytical Chemistry*, vol. 80, pp. 6800–6804 (2008).

[14] O. J. Cayre and V. M. Paunov, *Journal of Materials Chemistry*, vol. 14, pp. 3300–3302 (2004).

[15] H. Jiang and L. Dong, *Physics World*, vol. 19, pp. 29–31 (2006).

[16] V. V. Presnyakov, K. E. Asatryan, T. V. Galstian and A. Tork, *Optics Express*, vol. 10, pp. 865–870 (2002).

[17] S. Kuiper and B. H. W. Hendriks, *Applied Physics Letters*, vol. 85, pp. 1128–1130 (2004).

[18] D. Y. Zhang, V. Lien, Y. Berdichevsky, J. Choi and Y. H. Lo, *Applied Physics Letters*, vol. 82, pp. 3171–3172 (2003).

[19] S. W. Lee and S. S. Lee, *Applied Physics Letters*, vol. 90, 121129 (2007).

[20] H. Ren and S. T. Wu, *Applied Physics Letters*, vol. 86, 211107 (2005).

[21] X. Mao, J. R. Waldeisen, B. K. Juluria and T. J. Huang, *Lab on a Chip*, vol. 7, pp. 1303-1308 (2007).

[22] X. Mao, S. SC. Lin, M. I. Lapsley, J. Shi, B. K. Juluria and T. J. Huang, *Lab on a Chip*, vol. 9, pp. 2050-2058 (2009).

[23] Y. C. Seow, A. Q. Liu, L. K. Chin, X. C. Li, H. J. Huang, T. H. Cheng, and X. Q. Zhou, *Applied Physics Letters*, vol. 93, 084101 (2008).

[24] L. Dong, A. K. Agarwal, D. J. Beebe and H. Jiang, *Nature*, vol. 442, pp. 551–554 (2006).

[25] L. Dong, A. K. Agarwal, D. J. Beebe and H. Jiang, *Advanced Materials*, vol. 19, pp. 401–405 (2007).

[26] L. Dong and H. Jiang, *Applied Physics Letters*, vol. 89, 211120 (2006).

[27] J. Kim, M. J. Serpe and L. A. Lyon, *Journal of the American Chemical Society*, vol. 126, pp. 9512–9513 (2004).

[28] S. Xu, Y. Liu, H. Ren and S. T. Wu, *Optics Express*, vol. 18, pp. 12430–12435 (2010).

[29] L. Li, Q.-H. Wang and W. Jiang, *Journal of Optics*, vol. 13, 115503 (2011).

[30] L. Dong and H. Jiang, *IEEE/ASME Journal of Microelectromechanical Systems*, vol. 17, pp. 381-392 (2008).

[31] L. Dong and H. Jiang, *Applied Physics Letters*, vol. 91, 041109 (2007).

[32] A. K. Agarwal, S. S. Sridharamurthy, D. J. Beebe and H. Jiang, *IEEE/ASME Journal of Microelectromechanical Systems*, vol. 14, pp. 1409-1421 (2005).

[33] A. K. Agarwa, D. J. Beebe and H. Jiang, *Journal of Micromechanics and Microengineering*, vol. 16, pp. 332-340 (2006).

[34] D. J. Beebe, J. S. Moore, Q. Yu, R. H. Liu, M. L. Kraft, B. H. Jo and C. Devadoss, *Proceedings of the National Academy of Sciences, USA,* vol. 97, pp. 13488-13493 (2000).

[35] E. E. Tucker, S. B. Farnham and S. D. Christian, *The Journal of Physical Chemistry*, vol. 73, pp. 3820–3829 (1969).

[36] J. Atencia and D. J. Beebe, *Nature*, vol. 437, pp. 648-655 (2005).

[37] B. Ibarlucea, E Fernandez-Rosas, J. Vila-Planas, S. Demming, C. Nogues, J. A. Plaza, S. Büttgenbach and A. Llobera, *Analytical Chemistry*, vol. 82, pp. 4246–4251 (2010).

[38] H. Sedgwick, F. Caron, P. B. Monaghan, W. Kolch and J. M. Cooper, *Journal of the Royal Society Interface*, vol. 5, pp. S123-S130 (2008).

Chapter 5. Reversible White-light Actuation of Carbon Nanotube Incorporated Liquid Crystalline Elastomer Nanocomposites

(Parts of the contents in this chapter have been published as:

C. Li*, Y. Liu*, C.-W. Lo, and H. Jiang, "Reversible white-light actuation of carbon nanotube incorporated liquid crystalline elastomer nanocomposites", Soft Matter, vol. 7, no. 16, pp. 7511-7516, 2011. *:equal contribution.)

In this chapter, we present single-wall carbon nanotube (SWCNT) incorporated liquid crystal elastomer (LCE) nanocomposites that demonstrate strong, reversible photoactuation. The matrix nematic LCE material possesses reversible thermal deformation, while SWCNTs perform photo-thermal energy conversion and local heat dissipation upon irradiation. The resultant SWCNT-LCE nanocomposites exhibit effective photo-actuation not only by infrared (IR) irradiation, but also white light with an intensity on the order of 100 mW/cm^2. Rapid and reversible photo-induced strain was observed. The nanocomposite films contracted up to one third of the original length in several seconds under the irradiation of white light, and recovered to the original length in several seconds after the light source was switched off. Moreover, the nematic-isotropic transition temperatures of the SWCNT-LCE nanocomposites were evidently lower than that of the blank LCE (without carbon nanotube incorporation) by up to 19 °C.

5.1 Introduction

Certain materials that can change their dimensions and shapes upon application of a given stimulus, such as heat and light, have been of great interest [1]. Shape-memory alloys [2] or polymers [3] are good examples of such smart actuation materials. However, in most cases a shape-memory system is not reversible, requiring a reset after the actuation. Nematic liquid crystal elastomers (LCEs) [4] have proven to be a truly equilibrium reversible actuating system which can return to the equilibrium shape once the stimulus is removed. They possess several important features that lead to promising new actuation materials [5-11] such as orientational order exhibited by the mesogenic units in amorphous soft materials, topological constraints via the crosslinks, and responsive molecular shape due to the coupling between the orientational order and mechanical strain [4]. Nematic LCEs can dramatically and reversibly contract or elongate in response to temperature change. However, the response to an external stimulus is generally slow due to the low energy-transfer ability and thermal-conductivity, thus being difficult to be actuated remotely and limiting their potential applications. The response of a polymer to an external stimulus can be modified and improved when incorporated with different materials that impart new physical response. Carbon nanotubes (CNTs) are one of the effective filling materials for nanocomposites due to their one-dimension structures, nanometer scale diameters, high aspect ratios, large surface areas, and excellent conductivities and other physical and mechanical properties [12-14]. CNTs, especially the single-wall carbon nanotubes (SWCNTs), show strong absorptions in the visible and near-IR region owing to band gap transitions [15]. They can efficiently absorb and convert photo energy into thermal energy, and serve as a nanoscale heat source and thermal conduction pathway to heat the matrices effectively. Hence, SWCNTs can offer superior opportunities for the photo-actuation of thermal responsive materials. Studies showed that the shape-memory behavior of CNT-polyurethane nanocomposites irradiated via infrared (IR) light is more sensitive compared to the simplex polyurethane material [16]. It was also recently reported that LCEs incorporated with CNTs can be significantly actuated by IR irradiation [17, 18]. In this work, we prepared LCE nanocomposites using SWCNTs as fillers in a nematic side-chain LCE matrix with polysiloxane backbones. LCE nanocomposites with high loading level of SWCNTs up to 1.8 wt% were made by a relatively simple method. Experimental results showed that the addition of SWCNTs into the LCE matrix evidently lowered the material's nematic-isotropic transition temperature (T_{ni}) by up to about 19 °C, from 82 °C to about 63 °C. The decrease in T_{ni} of LCE due to incorporating SWCNTs was much larger than previously reported [18]. Moreover, we demonstrated that the SWCNT-LCE nanocomposites could be reversibly and rapidly actuated by white light from a wide-spectrum light source, rather than limited to IR or other specific wavelength as previously reported.

5.2 The Synthesis of the compounds

The pendant mesogenic group, 4-methoxyphenyl-4-(1-buteneoxy) benzoate (MBB), and di-functional crosslinking group, 1,4 alkeneoxybenzene (11UB), were synthesized as follows by leveraging the work reported in literature [19] and [20].

5.2.1 Synthesis of 4-methoxyphenyl-4-(1-buteneoxy) benzoate (MBB)

A solution of but-3-en-1-ol (6.2 g, 86 mmol), 4-hydroxybenzoic acid ethyl ester (14.3 g, 86 mmol) and triphenyl phosphine (22.56 g, 86 mmol) in tetrahydrofuran (40 mL) was added with diethyl azo dicarboxylate (13.54 mL, 14.98 g, 86 mmol) in drops over 30 minutes at the room temperature under an anhydrous nitrogen atmosphere. The reaction mixture was stirred for 24 hours and the solvent was removed in vacuum. The product was purified by flash column chromatography using silica gel as the stationary phase and the mixture of hexane and dichloromethane, with a ratio of 4:1, as the eluent. The solvent was removed in vacuum to yield 4-but-3-enyloxy-benzoic acid ethyl ester (13.4 g, 61 mmol, yield ratio: 71%) as a slightly yellow oil. A solution of 4-but-3-enyloxy-benzoic acid ethyl ester (7.8 g, 35.4 mmol), sodium hydroxide (3 g, 75 mmol) in ethanol (100 mL) and water (100 mL) was heated under reflux for 10 hours. The reaction mixture was cooled to the room temperature and acidified to pH 2 by hydrochloric acid. The white precipitate was collected and purified by washing with water. The product was recrystallized from ethanol to give 4-but-3-enyloxy-benzoic acid as a white solid (6.5 g, 33.8 mmol, yield ratio: 97%, mp =116 °C).

A mixture of 4-but-3-enyloxy-benzoic acid (1.89 g, 9.84 mmol), 4-methoxy phenol (1.2216 g, 9.84 mmol), 4-dimethylaminopyridine (1.2022 g, 9.84 mmol), 1,3-diisopropylcarbodiimide (1.4654 g, 11.6 mmol) and para-toluene sulfonic acid (1.8718 g, 9.84 mmol) in dry dichloromethane (20 mL) was stirred at the room temperature for 12 hours. The solvent was removed in vacuum and the resultant white solid was purified by flash column chromatography using silica gel as the stationary phase and dichloromethane as the eluant to give MBB. The product was recrystallized from ethanol (2.00 g, 6.7 mmol, yield ratio: 69%, mp =79 °C) as white crystals. ^{1}H NMR (ppm rel. to TMS): 2.55 (dt, 2H, =CHCH$_2$, J = 6.7), 3.82 (s, 3H, OCH$_3$), 4.09 (t, 3H, =CHCH$_2$CH$_3$, J = 6.7), 5.14 (dd, 1H, CH= trans to R, J = 10.3, 1.3), 5.19 (dd, 1H, CH= cis to R, J = 17.2, 1.6), 5.91 (m, 1H, CH=CH$_2$, J = 6.7–17.1), 6.92 (d, 2H, 2 aromatic H ortho to OCH$_3$, J ¼ 9.0), 6.96 (d, 2H, 2 aromatic H ortho to OR', J = 8.9), 7.11 (d, 2H, 2 aromatic H meta to OCH$_3$, J = 9.0), 8.13 (d, 2 aromatic H meta to OR', J = 8.9). Synthesis of 1,4 alkeneoxybenzene (11UB). A solution of hydroquinone (5.5 g, 50 mmol) and potassium carbonate (24.2 g, 175 mmol) in 100 mL ethanol was heated under reflux. A solution of 11-

chloro-1-undecene (22.65 g, 120 mmol) in ethanol (250 mL) was then added in drops to this over 30 minutes. After 18 hours of continued heating under reflux, the reaction mixture was poured into 1000 mL of iced water. This solution was extracted three times with diethyl ether (2000 mL in total). The organic layer was washed twice with saturated aqueous solution of sodium carbonate (500 mL in total) and once with water (500 mL), followed by drying over anhydrous magnesium sulfate. The diethyl ether was removed in vacuum, and the precipitation was subsequently purified by flash column chromatography using silica gel as the stationary phase and a mixture of dichloromethane and hexane, with the ratio of 1:3, as the eluent, followed by solvent removal in vacuum to yield 11UB as a white solid. The product was recrystallized from ethanol (30.1 g, yield ratio: 65%, mp = 56 °C). ^{1}H NMR (ppm rel. to TMS): 1.18 (m, 12H, $O(CH_2)_2C_6H_{12}$, J =7), 1.73 (qn, 2H, CH_2 CH_2, J = 6.5–7.0 Hz), 2.03 (dt, 2H,$=CHCH_2$, J = 6.5–7.0 Hz), 3.88 (t, 2H, OCH_2, J = 6.6 Hz), 4.92 (dd, 1H, CH= trans to R, J = 6.9, 1.1), 4.98 (dd, CH= cis to R, 1H, J = 13.0, 2.1), 5.80 (m, 1H, = CH, J = 6.8–3.2), 6.80 (s, 1H, aromatic H).

5.2.2 Material preparation

The pendant mesogenic group, MBB and 11UB were first synthesized as above. The polymer backbone was a poly-dimethylhydrosiloxane (PMHS) with approximately 60 Si–H units per chain, obtained from ACROS Chemicals (Belgium, USA). The commercial platinum catalyst dichloro(1,5-cyclooctadiene) platinum(II), obtained from Aldrich (St Louis, USA), was solved in toluene. The side-chain nematic LCE networks with the polysiloxane backbone, aligned in the uniaxial orientation, were prepared by leveraging the procedure reported in ref. 4 and 5. The polysiloxane backbone (PMHS) had its Si–H bonds reacted, using platinic acid catalyst, with the terminal vinyl groups of the mesogenic rod-like molecule (MBB) and the two-functional crosslinker (11UB) by hydrosilation, with a molar ratio of 20:1, thus achieving the 10:1 ratio of substituted groups on each chain or the effective 9% cross-linking density. The synthesis procedure was through two-stage crosslinking coupled with a drawing process.

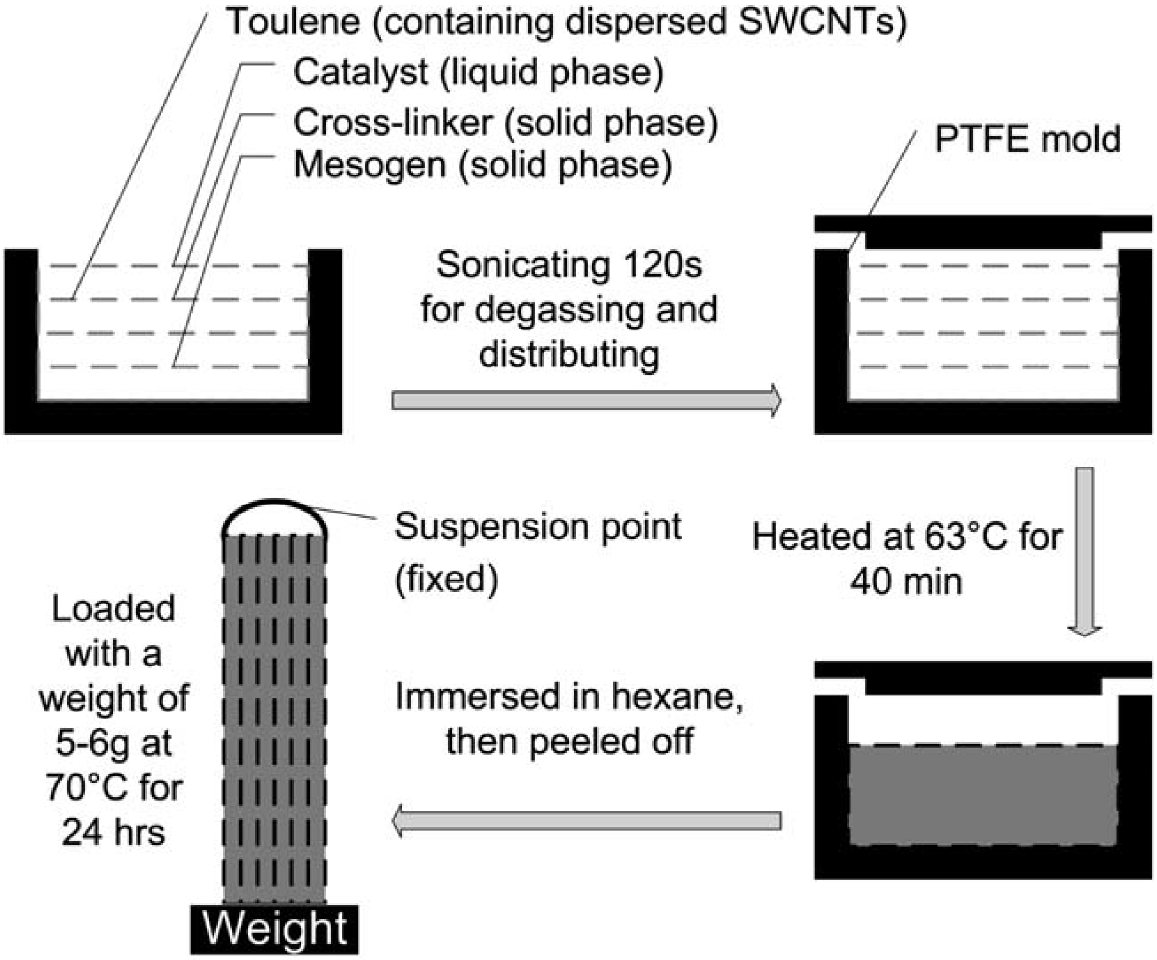

Figure 5-1. Fabrication process of SWCNT–LCE nanocomposite films.

The fabrication process of the SWCNT–LCE nanocomposite films is shown in Figure 5-1. SWCNTs were mixed into the reaction mixture solution, which was 0.12 g of PMHS, 0.5 g of MBB (1.68 mmol) and 0.068 g of 11UB (0.165 mmol) solved in 2 mL of toluene, under ultrasonication to ensure homogeneous dispersion; the ultrasonic mixing was performed for about 2 min. 100 mL of catalyst solution was added into the reaction mixture solution containing SWCNTs; then the solution was cast into a polytetrafluoroethylene (PTFE) rectangular parallel-piped mold with dimensions of 8 cm×1 cm ×1 cm. The mold was first high-power ultrasonicated for 3 minutes to remove the tiny bubbles entrapped in the mixture (this step was necessary, or the fabricated LCE would contain plenty of defects), then heated in an oven at 63 °C for 40 min for partial crosslinking process (first crosslinking stage). Thereafter the mold was cooled to the room temperature. The elastomer was then carefully removed from the mold, dried, and slowly uniaxially stretched along the length under a load—it can generally be stretched to 30% to 40% to attain a stable length—to obtain nematic alignment (drawing process). Then the film with the load was heated at 70 °C overnight to complete the crosslinking reaction in nematic phase (second crosslinking stage). We prepared SWCNT–LCE samples with SWCNT contents of 0.1, 0.3, 0.7, 1, and 1.8 wt% respectively. The blank nematic LCE was prepared by the same procedure but without SWCNTs.

5.2.3 Characterization methods

The phase transformation behavior was investigated by differential scanning calorimetry (DSC) measurements (TA Instruments Q100 modulated differential scanning calorimeter, New Castle, DE) at a heating and cooling rate of 10 K min^{-1}. The distribution of SWCNTs in the LCE matrix was examined with scanning electron microscopy (SEM; Zeiss LEO 1530, Thornwood, NY). The SWCNT¨CLCE nanocomposite was broken, and the cross-section was observed with SEM. The LCE mesomorphic properties were observed using polarizing optical microscopy (Nikon Instruments, SMZ 1500, Melville, NY). The photoactuation measurements of the LCE nanocomposite films were performed by using a wide spectrum light source (New Port, Oriel

Productline, Model 66885, Irvine, CA). The white light source illuminated the samples with irradiation intensities on the order of 100 mW cm^{-2}. The measurements of the actuation of the LCE and LCE nanocomposite films under IR irradiation were performed by using an IR source (Hotspot, Model H. S. 250.3, I^2R, Cheltenham, PA). The temperature change of the blank LCE film and the SWCNT-LCE films in response to the light stimulus was tested by a multilogger thermometer (HH 506 RA, OMEGA Engineering, Stamford, CT). The detector, with the dimension of 2mm in length and 100 mm in diameter, was placed on the sample surfaces. The contraction stresses of the films under light irradiation and their tensile strength were measured with a stress meter. All data reported in this paper were taken at a room temperature of 25 °C.

5.3 Results and discussions

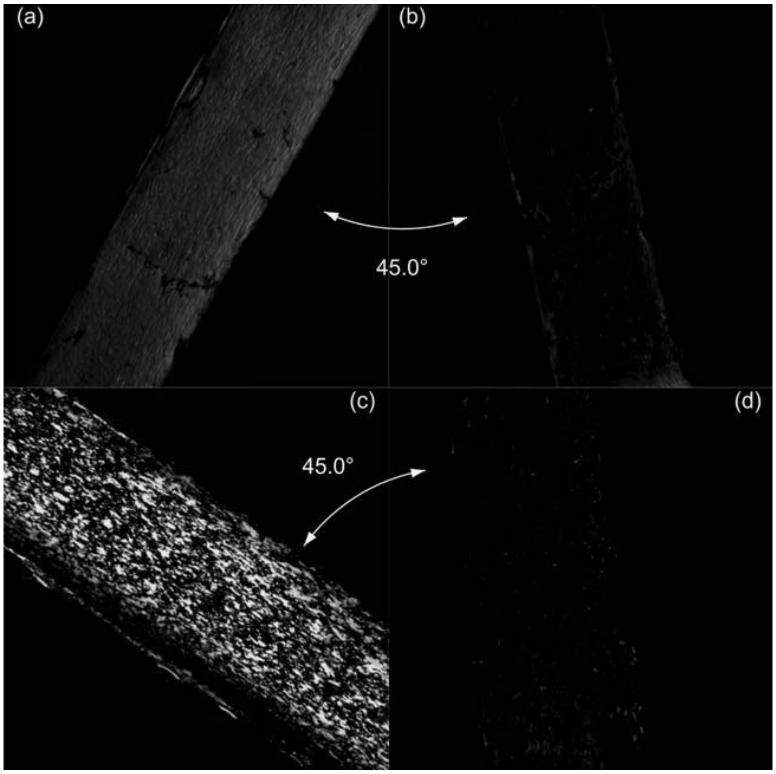

Figure 5-2. POMs of a blank LCE film and an SWCNT¨CLCE nanocomposite film (0.3 wt% of SWCNT content). (a) The angle between the stretch direction of the blank LCE film and the polarization direction of either polarizer is 45°. (b) The stretch direction of the blank LCE film is parallel to one of the polarization directions. (c) The angle between the stretch direction of the SWCNT-LCE nanocomposite film and the polarization direction of either polarizer is 45°. (d) The stretch direction of the SWCNT-LCE nanocomposite film is parallel to one of the polarization directions.

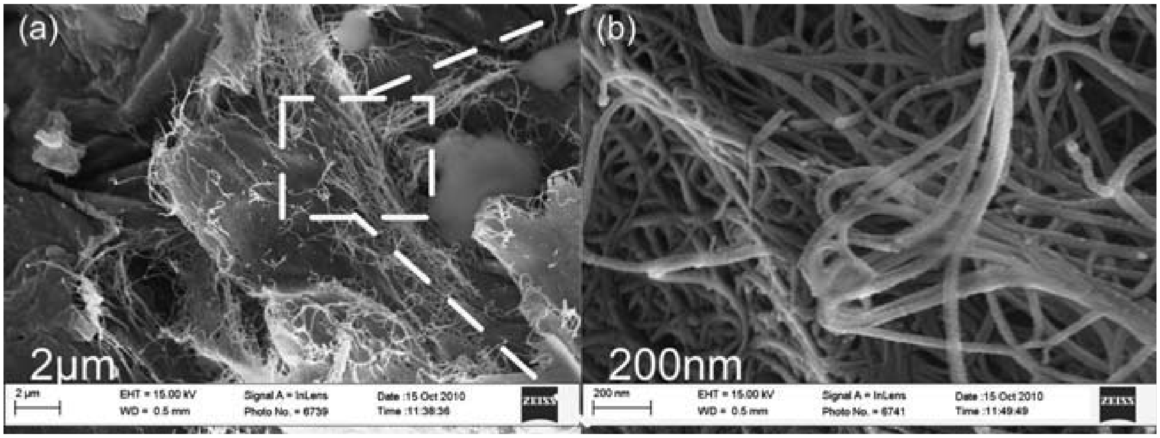

Figure 5-3. SEM image of SWCNTs in the LCE matrix. The SWCNT content in this nanocomposite film is 0.3 wt%.

The anisotropic alignment of the mesogens in the LCE matrix was evaluated at the room temperature by measuring the transmittance of a probe light through two crossed polarizers with a film between them. The polarizing optical micrographs (POMs) of a blank LCE film and an SWCNT-LCE nanocomposite film are shown in Figure 5-2. The highest transmittance appeared when the angle between the stretch direction of the films and the polarization direction of either polarizer was 45°, while the lowest appeared when the stretch direction was parallel to one of the polarization directions. Periodic changes of dark and bright images were observed by rotating the films with an interval of 45°. The POM observations of the blank LCE film and the SWCNT-

LCE nanocomposite film exhibited consistent result, though due to the blocking of light by SWCNTs, the transmittances in the images of the SWCNT-LCE nanocomposite film were much darker. The result proved an LCE nematic-phase texture, and that the mesogenic units were well aligned along the stretch direction. SEM images of the SWCNT-LCE nanocomposites proved that the SWCNTs were effectively dispersed in the LCE matrix, as shown in Figure 5-3. Experiments indicated that these LCE and LCE nanocomposite films contracted along the axis when heated, and regained their original length after cooling down, as shown in Figure 5-4.

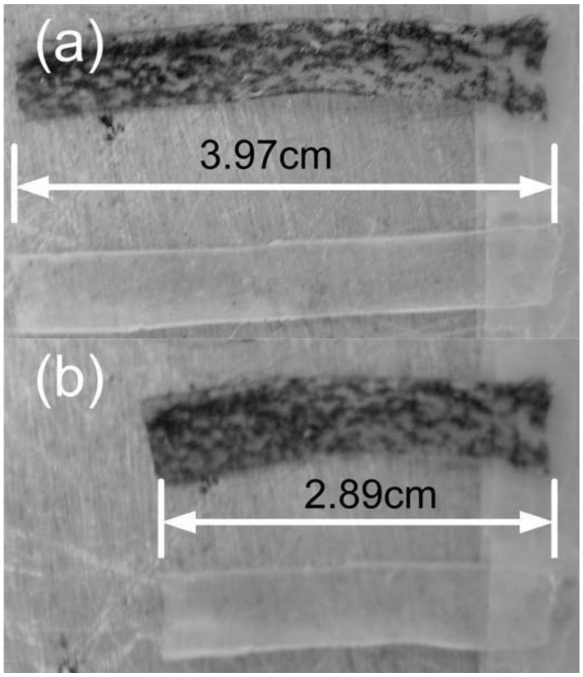

Figure 5-4. Optical images of the thermal actuation of a blank LCE film and an SWCNT-LCE nanocomposite (SWCNT content: 0.3 wt%) film on a hot plate. The films have a dimension of 4 cm×0.5 cm×0.7 mm. (a) The state of the films when the temperature of the hot plate is 25 °C. (b) The state of the films when the temperature of the hot plate is 85 °C.

Fully reversible contraction and restoration were observed under these heating/cooling cycles. This shape deformation was induced by the change in the nematic order. Nematic LCE possesses the uniaxial orientational order. The order is characterized by its principal axis, which is the nematic director, and the scalar order parameter which measures the mean orientation of the mesogenic groups with respect to the director. Owing to such internal degree of freedom coupled to the elastic body constituted by rigid rod-like mesogens linked to the chain conformation, the relative movement of crosslinking points provides elastic strains and forces, while the director rotation causes local torques and couple-stresses, which are both intricately connected in the overall macroscopic response of the body. The change in the degree of alignment of mesogenic rods leads to spontaneous elongation or contraction of the whole network along the nematic director. When the nematic LCE is heated above or cooled down below its T_{ni}, the nematic order is changed, and the spontaneous uniaxial contraction/restoration of the nematic LCE along the director axis can be realized [4, 21]. Figure 5-5 presents the DSC measurement of phase transformations in the prepared LCE and SWCNT-LCE nanocomposites. The glass transition temperature (T_g) and T_{ni} measured from the DSC heating cycles are listed in Table 1. It shows that T_g of all samples are near 0 °C. Therefore, they maintain the elastic property at normal temperatures. T_{ni} of blank nematic LCE is about 82 °C, while those of the SWCNT-LCE nanocomposites are evidently lower. In general, the higher the SWCNT contents, the lower the T_{ni}. With 1.8 wt% of SWCNTs, T_{ni} decreases to about 63 °C. We believe that the mechanism might lie in the thermal-mechanical response of CNTs in the polymer matrices [16, 22]. Such thermal stress of CNTs might have promoted the transition of the mesogenic groups from the nematic state to the isotropic state, leading to the lowering of T_{ni}. Experiments also demonstrated attractive photo-induced actuation characteristics of the SWCNT–LCE nanocomposites. We used a white light source, without filtering to any specific wavelength.

Figure 5-6 shows the response of a blank LCE film and an SWCNT–LCE nanocomposite film under a white-light irradiation of 230 mW cm^{-2} in intensity. The blank LCE film, which was essentially photo-transparent with a low photo-thermal energy conversion efficiency, remained unaffected and did not contract. Our experiment further showed that the blank LCE film could not be actuated even under a 10W cm^{-2} intensity of white-light irradiation (maximum output from our light source). In contrast, the SWCNT-LCE nanocomposite film started conspicuous contraction ~5 seconds after being exposed to 230 mW cm^{-2} of irradiation and reached maximum contraction after ~10 seconds, as demonstrated in Figure 5-6. It recovered to its initial length ~9 seconds after the light source was switched off, indicating completely reversible photoactuation. In addition, experiment indicated that under an irradiation of 413 mW cm^{-2}, a contraction stress of 75 kPa was created in the SWCNT-LCE nanocomposite film, while the contraction stress in the blank LCE film was almost 0. The SWCNTs can efficiently absorb and convert photo-energy into thermal energy, thus acting as nanoscale heaters uniformly embedded in the LCE matrix. SWCNTs also have high thermal conductivities. Moreover, previous research work showed that SWCNTs can form a percolation network in polymer matrices at loading levels above 0.1 wt% [23]. Thus, at such loading levels of SWCNTs, SWCNTs can serve as effective thermal conduction pathways to heat the LCE matrix uniformly and rapidly. The absorbed thermal energy increased the temperature in the material to above T_{ni}, leading to the nematic-isotropic phase transition and axial strain in the LCE nanocomposite. The IR-induced actuation characteristics of the LCE and SWCNT-LCE nanocomposites were also measured. Experimental results showed that when the IR irradiation was 1.7 W cm^{-2}, there was almost no contraction stress in the blank LCE film, while the contraction stress in the SWCNT-LCE nanocomposite film with an SWCNT content of 0.3 wt% was 55 kPa.

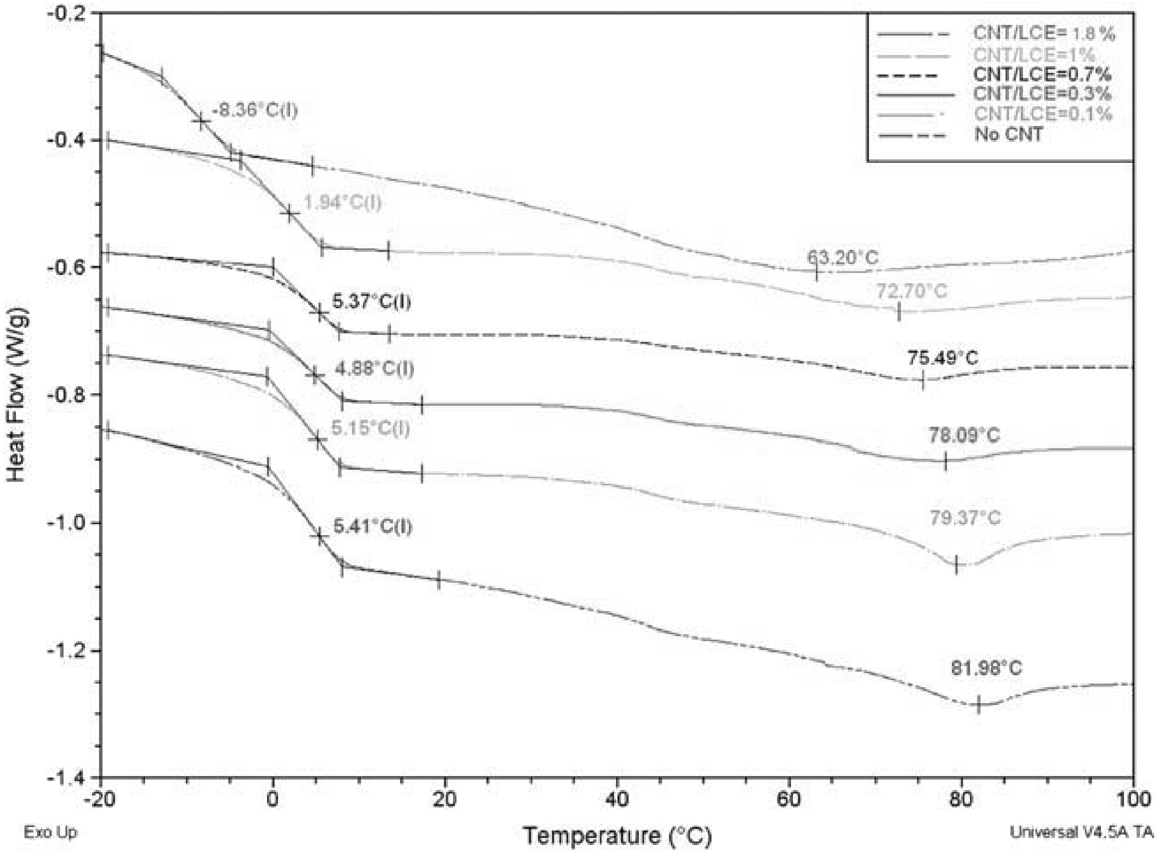

Figure 5-5. DSC data curves of the blank LCE and different SWCNT-LCE nanocomposites.

Table 5-1. Characteristics of the blank LCE and SWCNT-LCE nanocomposites. The maximum axial contraction ratios actuated by a photoirradiation is defined as (L_0-L)/L_0, where L_0 is the initial length, and L_0-L is the maximum stable axial contraction strain under the photoirradiation. The SWCNT-LCE nanocomposites are actuated by white light, while the blank LCE is actuated by IR light. The films have a dimension of 4 cm×0.5 cm×0.7 mm, and are loaded by 3 g of weights during the photoactuation process.

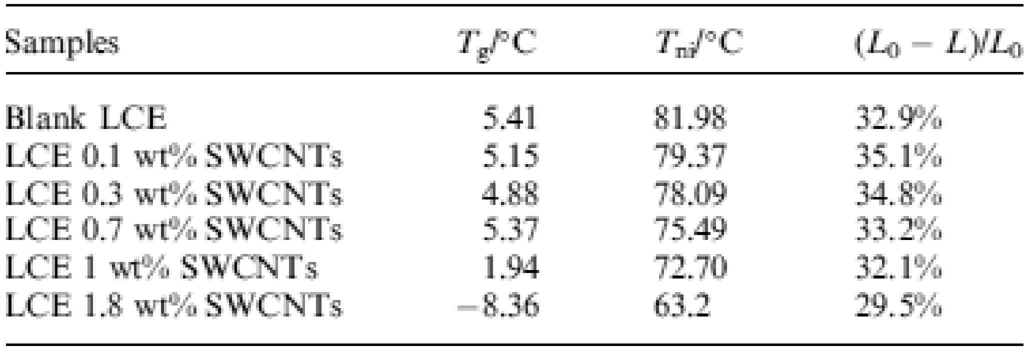

Samples	T_g/°C	T_{ni}/°C	$(L_0 - L)/L_0$
Blank LCE	5.41	81.98	32.9%
LCE 0.1 wt% SWCNTs	5.15	79.37	35.1%
LCE 0.3 wt% SWCNTs	4.88	78.09	34.8%
LCE 0.7 wt% SWCNTs	5.37	75.49	33.2%
LCE 1 wt% SWCNTs	1.94	72.70	32.1%
LCE 1.8 wt% SWCNTs	−8.36	63.2	29.5%

When the IR irradiation was 3.4W cm^{-2}, the contraction stress in the blank LCE film was 14 kPa, while the contraction stress in the SWCNT-LCE nanocomposite film was 80 kPa. This indicates that both the blank LCE and the SWCNT-LCE nanocomposites can be actuated by IR irradiation since IR is a strong thermal radiation source compared to the general visible light sources, including white light. However, in the SWCNT-LCE nanocomposites, the SWCNTs can efficiently absorb the irradiation and convert it into thermal energy to heat up the LCE matrix; therefore, the needed IR irradiation intensity to actuate the blank LCE is much higher than that to actuate the SWCNT-LCE nanocomposites. The maximum axial contraction ratio, which is the axial contraction strain between T_{ni} and the room temperature, under photo-irradiation for each sample is also listed in Table 1. All of the SWCNT-LCE nanocomposite samples were fully contracted under white light, while the blank LCE was actuated by IR light. The maximum axial contraction ratio of the blank LCE is about 1/3. The SWCNT-LCE nanocomposites with different SWCNT contents show similar maximum axial contraction ratios to the blank LCE, indicating that the addition of SWCNTs into LCE matrix did not attenuate the actuation.

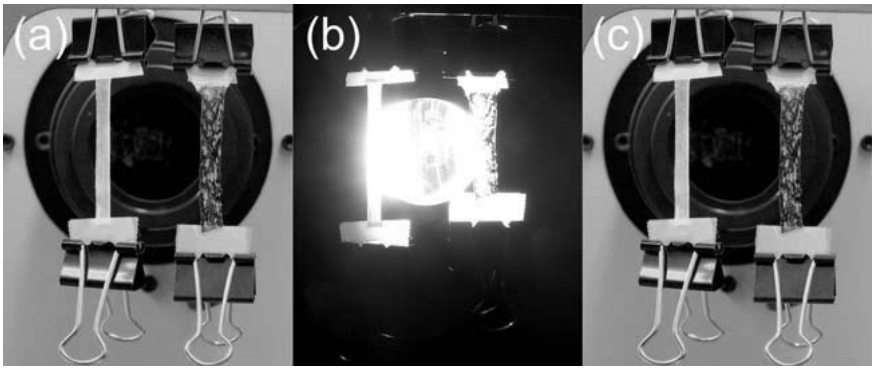

Figure 5-6. Optical images of the photo-actuation of blank LCE and SWCNT-LCE nanocomposite (SWCNT content: 0.3 wt%) films. The films have a dimension of 4 cm×0.5 cm×0.7 mm. They are loaded by 3 g of weights during the photo-actuation process. The irradiation intensity here is 230 mW cm^{-2}. (a) The initial state of the blank LCE and SWCNT-LCE nanocomposite films. (b) Comparison of the two films under irradiation. The blank LCE does not deform after being illuminated for several minutes. In contrast, SWCNT-LCE nanocomposite film starts conspicuous contraction after ~5 seconds, and reaches the stable length, which is about 2/3 of the initial length, after ~10 seconds. (c) The SWCNT-LCE nanocomposite film recovers to its initial length ~9 seconds after the light source is switched off.

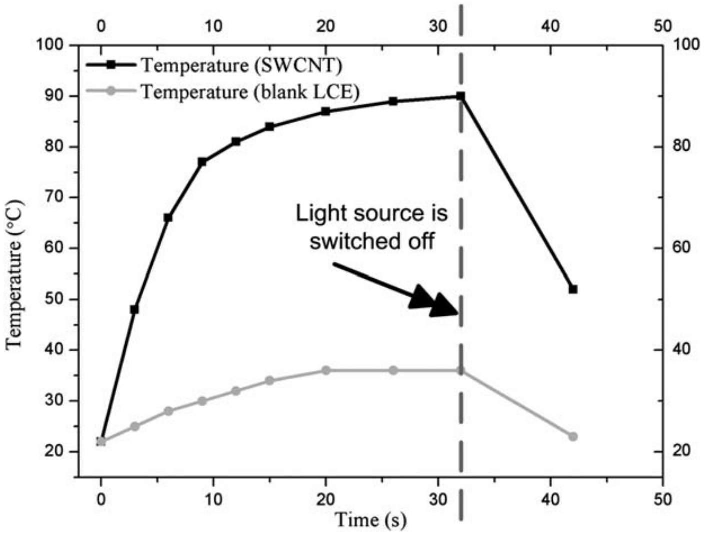

Figure 5-7. Change in temperature of the blank LCE film and the SWCNT-LCE nanocomposite film (SWCNT content: 0.3 wt%) under the white light stimulus. The irradiation intensity is 230 mW cm^{-2}.

Figure 5-7 shows the temperature change of the blank LCE and SWCNT-LCE nanocomposite films under the irradiation of the white light. After the irradiation started, the temperature at the surface of the SWCNT-LCE nanocomposite film could rise from room temperature to about 80 °C, which is above its T_{ni}, within 10 seconds, and eventually reached 90 °C. When the light source was switched off, its temperature dropped from 90 °C to near 50 °C, which is obviously below its T_{ni}, within 10 seconds. In contrast, the temperature at the surface of the blank film could only rise to 36 °C, which is far below its T_{ni}, under the irradiation of the white light. In addition, experiments indicated that some mechanical properties of the SWCNT-LCE nanocomposites were improved due to reinforcement from the SWCNTs.

5.4 More characterization results

More characterizations regarding the blank LCE, the SWCNT/LCE and LCE incorporated by graphene oxide ~0.3% w/w, were conducted in order to examine the difference in molecular level of the above three, including a Fourier transform infrared spectroscopy (FTIR) and an X-ray diffraction spectroscopy. The results are shown in Figure 5-8 and Figure 5-9. However, comparing the 3 curves in Figure 5-8, no obvious differences could be observed, indicating FTIR was not a valid method to distinguish the three samples. The reason of such result may be that the concentration of the CNTs and graphene oxide in the LCE matrix is not high enough to exhibit obvious absorption peaks, comparing to the excessive amount of highly-ordered LCE molecules. Meanwhile, the XRD patterns demonstrate the polarization and alignment of the LCE films, but it’s also not a valid approach to distinguish the three kinds of LCEs. The patterns do not show much differences except for intensity difference, which is not related to the difference components in the matrix.

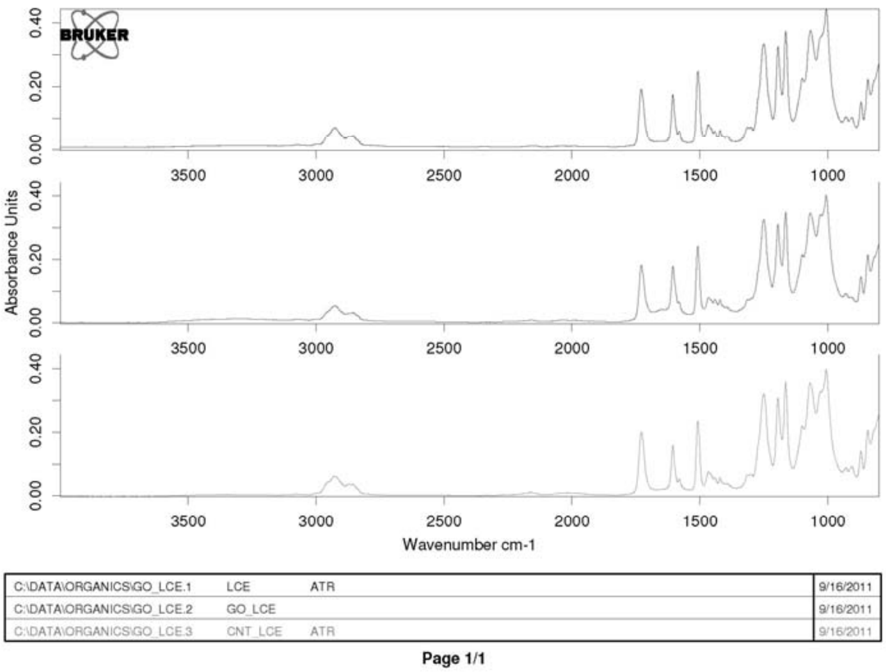

C:\DATA\ORGANICS\GO_LCE.1	LCE	ATR	9/16/2011
C:\DATA\ORGANICS\GO_LCE.2	GO_LCE		9/16/2011
C:\DATA\ORGANICS\GO_LCE.3	CNT_LCE	ATR	9/16/2011

Page 1/1

Figure 5-8. FTIR spectrums of blank LCE (LCE), graphene-oxide incorporated LCE (GO/LCE) and CNT incorporated LCE (CNT/LCE) films with thicknesses of 200µm.

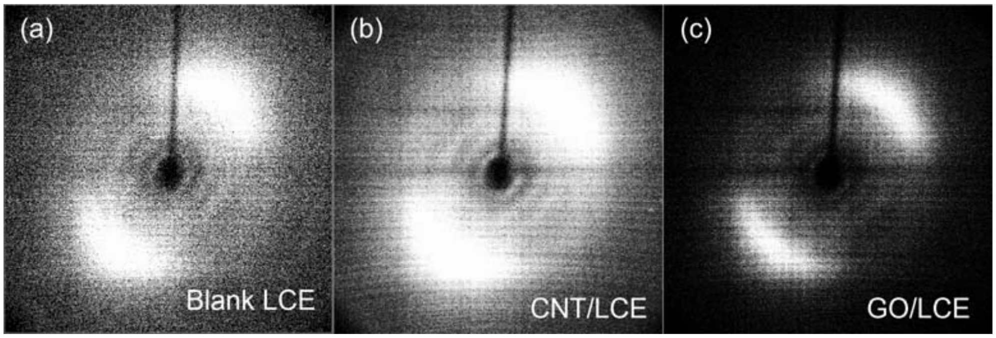

Figure 5-9. X-ray diffraction pattern of blank LCE (blank LCE), graphene-oxide incorporated LCE (GO/LCE) and CNT incorporated LCE (CNT/LCE) films with thicknesses of 200µm.

5.5 Conclusion

Among various materials used in actuator designs, the nematic LCEs would be of especial importance due to their large deformation, reversible actuation, relative ease to manipulate and control, etc. The study of photo-actuation of LCE materials shows that nematic LCEs have a great potential in practical applications, including artificial muscles, micro- and nano-actuators, and micro-robots [8–11]. In our work, the nanocomposite films of SWCNT-LCE with polysiloxane backbone and pre-aligned side-on mesogenic units were successfully prepared via a two-stage crosslinking process coupled with a drawing technique.

High level of SWCNTs can be loaded and effectively dispersed into the LCE matrix in this simple process, and relatively thick films can be fabricated. Some salient characteristics were observed: the SWCNT–LCE nanocomposites can not only be actuated by IR light as previously reported, but also by much wider spectrum of light with an intensity on the order of $100 mWcm^{-2}$; T_{ni} of SWCNT–LCE nanocomposites are significantly lowered from that of the blank LCE as compared to previously reported; the maximum contraction was not attenuated by SWCNTs filled in the LCE matrix. Much wider choice of light source for actuation and much lower required actuation temperature (due to much lower T_{ni}) of our SWCNT–LCE nanocomposites significantly increase the practicality of the applications of the nematic LCE materials. Filling SWCNTs in LCE matrix can also help improve the mechanical properties, which also enhances the practicability of the materials.

5.6 References

[1] J. E. Huber, N. A. Fleck and M. F. Ashby, *Proceedings of the Royal Society, London, Series A*, vol. 453, pp. 2185-2205 (1997).

[2] K. Bhattacharya, *Microstructure of Martensite*, Oxford University Press, Oxford, 2004.

[3] A. Lendlein, A. M. Schmidt and R. Langer, *Proceedings of the National Academy of Sciences, USA*, vol. 98, pp. 842-847 (2001).

[4] M. Warner and E. M. Terentjev, *Liquid Crystal Elastomers*, Oxford University Press, Oxford, 2003.

[5] J. Kupfer and H. Finkelmann, *Makromolekulare Chemie, Rapid Communications*, vol. 12, pp. 717-726, (1991).

[6] H. Finkelmann, E. Nishikawa, G. G. Pereira and M. Warner, *Physical Review Letters*, vol. 87, 015501 (2007).

[7] Y. L. Yu, M. Nakano and T. Ikeda, *Nature*, vol. 425, pp.145 (2003).

[8] M. Camacho-Lopez, H. Finkelmann, P. Palffy-Muhoray and M. Shelley, *Nature Materials*, vol. 3, pp. 307-310 (2004).

[9] M. Yamada, M. Kondo, J. I. Mamiya, Y. L. Yu, M. Kinoshita, C. Barrett and T. Ikeda, *Angewandte Chemie International Edition,* vol. 47, pp. 4986-4988 (2008).

[10] S. Xu, H. W. Ren, Y. J. Lin, M. G. J. Moharam, S. T. Wu and N. Tabiryan, *Optics Express*, vol. 17, pp. 17590-17595 (2009).

[11] F. T. Cheng, R. Y. Yin, Y. Y. Zhang, C. C. Yen and Y. L. Yu, *Soft Matter*, vol. 6, pp. 3447-3449 (2010).

[12] S. Iijima, *Nature*, vol. 354, pp. 56-58 (2001).

[13] S. N. Kim, J. F. Rusling and F. Papadimitrakopoulos, *Advanced Materials*, vol. 19, pp. 3214-3228 (2007).

[14] W. Y. Zhou, X. D. Bai, E. G. Wang and S. S. Xie, *Advanced Materials*, vol. 21, pp. 4565-4583 (2009).

[15] M. A. Hamon, M. E. Itkis, S. Niyogi, T. Alvaraez, C. Kuper, M. Menon and R. C. Haddon, *Journal of the American Chemical Society,* vol. 123, pp. 11292-11293 (2001).

[16] H. Koerner, G. Price, N. A. Pearce, M. Alexander and R. A. Vaia, *Nature Materials*, vol. 3, pp. 115-120 (2004).

[17] L. Q. Yang, K. Setyowati, A. Li, S. Q. Gong and J. Chen, *Advanced Materials*, vol. 20, pp. 2271-2275 (2008).

[18] Y. Ji, Y. Y. Huang, R. Rungsawang and E. M. Terentjev, *Advanced Materials,* vol. 22, pp. 3436-3440 (2010).

[19] S. V. Arehart and C. Pugh, *Journal of the American Chemical Society*, vol. 119, pp. 3027-3037 (1997).

[20] O. Mitsunobu, *Synthesis*, vol. 1, pp. 1-28 (1981).

[21] K. K. Hon, D. Corbett and E. M. Terentjev, *The European Physical Journal E,* vol. 25, pp. 83-89 (2008).

[22] S. V. Ahir and E. M. Terentjev, *Nature Materials*, vol. 4, pp. 491-495 (2005).

[23] R. Ramasubramaniam, J. Chen and H. Liu, *Applied Physics Letters*, vol. 83, pp. 2928-2930 (2003).

Chapter 6. Enhancing Solar Cell Output through Artificial Heliotropism Utilizing Actuators Directly Driven by Sun

(Parts of the contents in this chapter have been published as:

C. Li*, Y. Liu*, X. Huang, H. Jiang, "Direct sun-driven artificial heliotropism for solar energy harvesting based on photo-thermo-mechanical liquid crystal elastomer nanocomposite," Advanced Functional Materials, doi: 10.1002/adfm.201202038, 2012. *: equal contribution.)

In this chapter, we have demonstrated artificial heliotropism energy harvesting system utilizing the SWCNT-LCE photomechanical actuators based on the LCE nanocomposite described in chapter 5. Heliotropism, or solar tracking, is an intriguing attribute possessed by some plants whose leaves or flowers can follow the sun for increased light interception. Inspired by heliotropism in nature, artificial heliotropic devices that can follow the sun for increased light interception are realized. The mechanism of the artificial heliotropism is realized via direct actuation by the sunlight, eliminating the need for additional mechatronic components and resultant energy consumption. For this purpose, the reversible photo-thermomechanical liquid crystalline elastomer (LCE) nanocomposite, based on the nanocomposite described in chapter 5, is developed that can be directly driven by natural sunlight and possesses strong actuation capability. Using the LCE nanocomposite actuators, the artificial heliotropic devices show full-range heliotropism in both laboratory and in-field tests. As a result, significant increase in the photocurrent output from the solar cells in the artificial heliotropic devices is observed.

6.1 Introduction

As a renewable clean energy source, solar energy, and converting it to electric power is of great commercial and research interest [1]. Generally, two kinds of strategy are used to enhance the harvesting of solar energy, the first focuses on the direct enhancing the solar-to-electric conversion efficiency [2-4], while the second is increasing the available solar radiation onto the solar cell surface to significantly augment the power output by [5]. One approach of the second strategy is to use the concentrators [6-9]. Another approach is through solar tracking, inspired by some plants that show heliotropism (following the sun), so that their flowers or leaves always face the sun to increase interception of the sunlight [10]. The goal of solar-tracking, as indicated by the name, is allowing the solar energy harvesting devices (for example, solar cells) to change their positions (adaptively) along with the change of the incident angle of the sunlight, so as to maximize the inception of the sunlight for the solar energy harvesting devices. For example, with full-range (devices change position along with the movement of the sun in both azimuth and altitude direction) solar tracking, the yearly electric output of a solar cell in Madison, WI, USA could theoretically be increased by 31%, as compared to a fixed tilt configuration [11]. However, mechatronic designs are generally used in current man-made systems for active full-range solar tracking [12]. For these designs, generally a sensing system is needed to determine the position of the sun and an actuator (for example, a motor) is needed to drive the solar cell to its designated position. These sensing-actuator systems may imply high cost, and high power consumption, which might negate the gain.

Here, we report on prototype solar-tracking devices in which artificial heliotropism is realized by SWCNT-LCE actuators that are driven by the sunlight *directly* and *adaptively*, eliminating the need for any electric-power-consuming sensing and actuating components. Integrated with those devices, the electric output from solar cells can be significantly enhanced as a result of full-range solar tracking. This approach is self-contained, thus is compatible with other methods to increase the solar cell output, such as the enhancing of the conversion efficiency of the solar cells and implementing concentrators.

6.2 Operation principle and optimizations

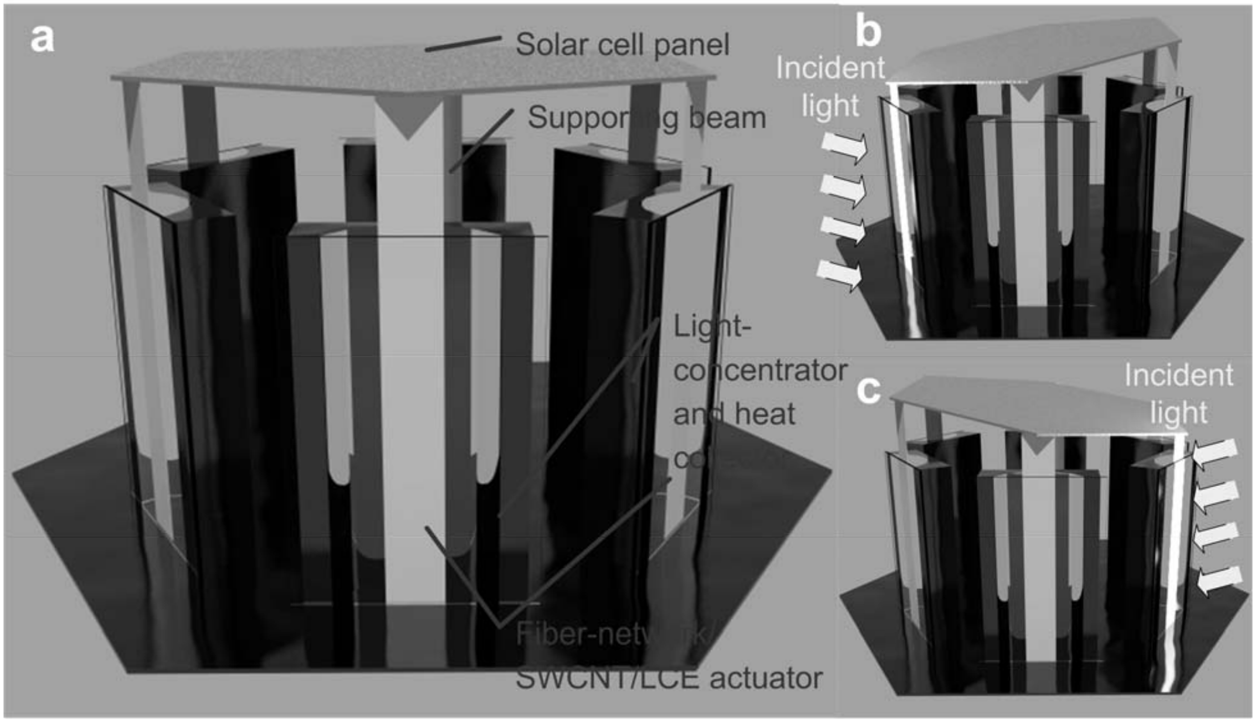

Figure 6-1. Concept of the solar-tracking system. (a) 3D schematic of the system. (b, c) 3D schematic of the heliotropic behavior. Actuator(s) facing the sun contracts, tilting the solar cell towards the sunlight.

Figure 6-1 shows the concept of our artificial heliotropism. The solar cells are installed on a platform that is connected to actuators and flexibly supported so that it can tilt under the actuation force [Figure. 6-1(a)]. At any time instant, actuator(s) facing the incoming sunlight would be in a contracted state, while other actuators not exposed to sunlight would be in the relaxed state. Consequently, the platform holding the solar cells would be driven by the contracted actuator(s), and self-adaptively tilt towards the sunlight, hence the artificial heliotropism and increased photocurrent output from the solar cells [Figure 6-1(b)]. Note that the actuation/tilting and the resultant solar tracking are directly driven by the sunlight.

Our solar-tracking mechanism requires actuators that can photo-mechanically respond to the intensity of normal sunlight (i.e., about 1000W/m^2, or 1 Sun, Air Mass 1.5 G; without filtering). Such photomechanical response must also be reversible. There is yet a material that can fulfill both of these requirements. In chapter 5, we reported an opto-thermo-mechanical liquid-crystal elastomer (LCE) nanocomposite that can be reversibly and rapidly actuated by a wide-spectrum white light. The LCE nanocomposite is formed by incorporating single-wall carbon nanotubes (SWCNTs) into a matrix of nematic LCE [13]. Since SWCNTs can efficiently absorb / convert photon energy into thermal energy and have excellent thermal conductivities [14], thus acting as nanoscale heat source and thermal conduction pathway to effectively heat the LCE matrix, raising its temperature to above the nematic–isotropic transition temperature (T_{ni}), leading to an axial contraction and mechanical actuation [13, 15, 16]. This nanocomposite material has the potential to be used in the required actuator for our solar-tracking mechanism. To fully meet the aforementioned requirements for solar tracking, we have improved the properties of the SWCNT/LCE nanocomposite and designed actuators based on this nanocomposite.

6.2.1 Improving of the SWCNT/LCE actuators

First, we significantly enhanced the mechanical property, especially the rupture strength of the SWCNT/LCE material by embedding polyurethane fiber-networks as the reinforcement phase into the LCE matrix. The resultant actuator has much improved rupture strength compared to our previous SWCNT/LCE nanocomposite, and is sufficiently strong for the device testing later described. Meanwhile, the photomechanical response of the fiber-network/SWCNT/LCE actuators is maintained as compared to the SWCNT/LCT actuators. Figure 6-2 (a) shows an X-ray diffraction pattern obtained from a fiber-network/ SWCNT/LCE sample, while Figure 6-2 (b) shows the corresponding azimuthal intensity distribution of the X-ray diffraction pattern., from which we can clear observe that the LCE molecular compositing the fiber-network/ SWCNT/LCE actuator is aligned along its uni-axial direction. Figure 6-2 (c) depicts the DSC curve (heat-flow v. s. temperature) of the fiber-network/SWCNT/LCE actuator, comparing to a blank LCE, from which we can see the incorporating of SWCNT effectively lowers the T_{ni} of the actuators by ~13ºC, while the incorporation of the fiber-network does not exhibit negative effect on the lowering of the $T_{ni.}$ Figure 6-2(d) and (e) demonstrate the photomechanical response of a fiber-network/SWCNT/LCE actuator film under a white light radiation (intensity: 230 mW/cm^2, ~2.3 Suns, Air Mass 1.5 G). The fiber-network/SWCNT/LCE actuator film exhibits a uniform contraction of ~27%, consistent with that of the SWCNT-LCE film reported in chapter 5[13].

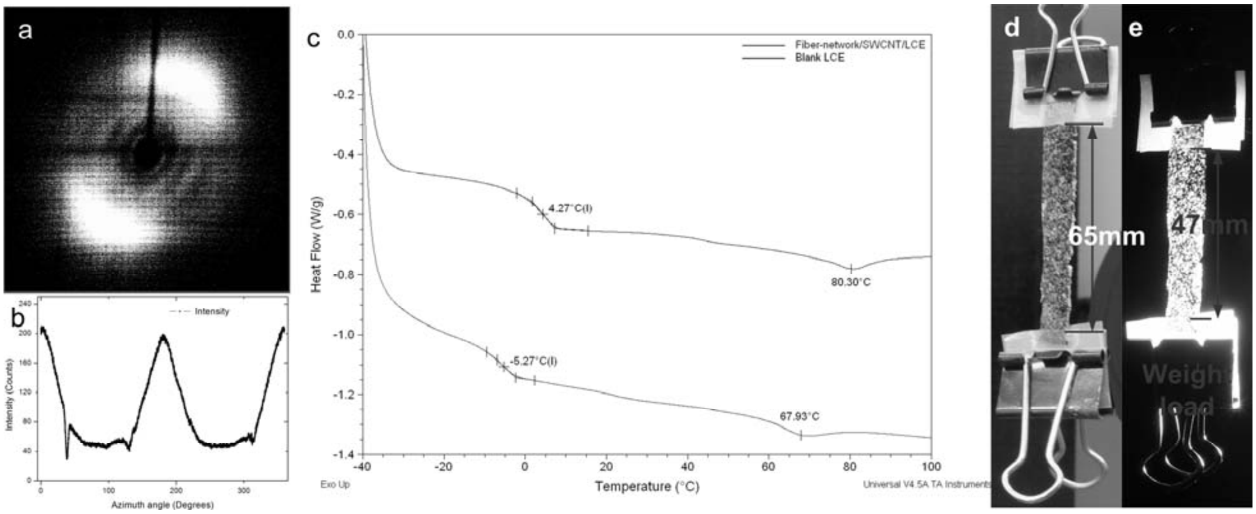

Figure 6-2. a) An X-ray diffraction pattern obtained from a fiber-network/ SWCNT/LCE sample. b) Azimuthal intensity distribution of the X-ray diffraction pattern of fiber-network/SWCNT/ LCE. c) DSC data curves of the blank LCE and fiber-network/ SWCNT/LCE nanocomposite. (d) Response of a fiber-network/SWCNT/LCE film (65mm×4mm×0.8mm), loaded with a 2.92 g weight, to an incident white light of 230 mW/cm^2. (d) Before irradiation. (e) After irradiation.

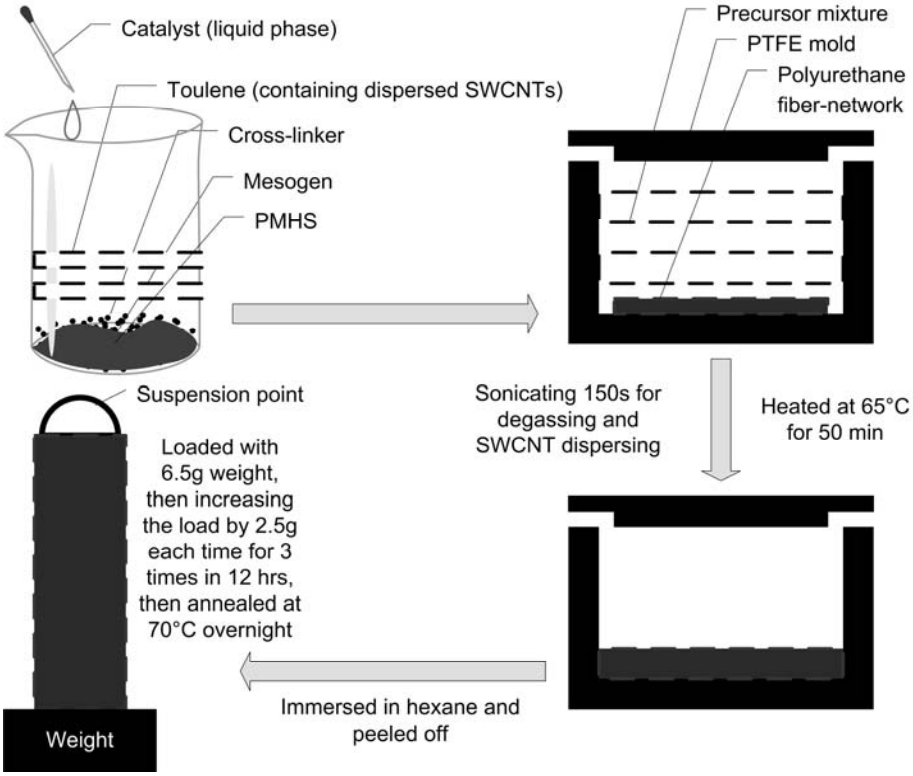

Figure 6-3. Fabrication process of the fiber-network/SWCNT/LCE composite film.

The fabrication process of the fiber-network/SWCNT/LCE is illustrated in figure 6-3, similar to that reported in chapter 5. The pendant mesogenic group, 4-methoxyphenyl-4-(1-buteneoxy) benzoate, and di-functional crosslinking group, 1, 4 alkeneoxybenzene, were synthesized as reported in chapter 5. The polymer backbone was a poly-methylhydrosiloxane (PMHS) with approximately 60 Si–H units per chain, obtained from ACROS Chemicals (Geel, Belgium). The commercial platinum catalyst dichloro(1, 5-cyclooctadiene) platinum(II) was obtained from Sigma-Aldrich (St Louis, MO, USA). The catalyst solution was prepared by dissolving 0.025g of the dichloro(1, 5-cyclooctadiene) platinum(II) (from Sigma-Aldrich, St Louis, MO, USA) in 2 ml of dichloromethane, then adding 20 ml of toluene. The polyurethane fiber-network was obtained through slicing a polyurethane porous bulk material to a lamella with the thickness of 0.4 mm. It became a flexible layer of polyurethane fiber-network with irregular meshes.The synthesis of the side-chain nematic LCE networks with polysiloxane backbone, aligned in uniaxial orientation, was based on a two-stage crosslinking coupled with a drawing process, as reported chapter 5.

The fabrication process of the fiber-network/SWCNT/LCE composite films with SWCNT/nematic LCE (the content of SWCNTs in LCE was about 0.4 wt%) as the matrix and polyurethane fiber-network as the reinforcement phase is shown in Figure 6-3. 3.7 mg of SWCNTs were mixed into the reaction mixture solution, which was 0.16 g of PMHS, 0.65 g of 4-methoxyphenyl-4-(1-buteneoxy) benzoate (2.18 mmol) and 0.088 g of 1, 4 alkeneoxybenzene (0.214 mmol) solved in 2.6 mL of toluene, under ultrasonication for better dispersion; the ultrasonic mixing was performed for about 2 min. 120 μL of catalyst solution was added into the reaction mixture solution containing SWCNTs; then the solution was cast into a polytetrafluoroethylene (PTFE) rectangular parallel-piped mold with dimensions of 90 mm × 14 mm × 10 mm, on the bottom of which a rectangular lamella of polyurethane fiber-network with the length and width of 90 mm and 12 mm, respectively, was pre-laid. The precursors inside the mold was first ultrasonicated for 2.5 minutes to degas the mixture, then heated in an oven at 65°C for 50 min for partial crosslinking process (first crosslinking stage). A swollen gel of partially crosslinked elastomer with the toluene solvent absorbed inside it was generated during this first crosslinking stage. Thereafter the mold was cooled to the room temperature. 7 mL of hexane was poured into the mold to facilitate the removal process of the partially crosslinked elastomer embedded with the polyurethane fiber-network, which was then carefully removed from the mold. The elastomer was immediately hung at one end with a clamp for drying at the room temperature. As the toluene contained in the partially crosslinked elastomer evaporated, the elastomer gradually shrank and the flexible polyurethane fiber-network shrank together. The drying process proceeded for about 40 min, and the composite film contracted to a stable length of about 6.3 cm from its original length of 9 cm. Subsequently the drawing process started, with the other free end of the composite film now loaded with a 6.5 g weight. The loading weight was increased step by step, with 2.5 g of increment every two hours, to 14 g. After 12 hours of gradual uniaxial stretch along the length by the load, the composite film extended to a stable length of about 9 cm and a nematic alignment in LCE matrix was obtained. After this drawing process, the length of the composite film was equal to that of the mold, and the embedded polyurethane fiber-network recovered to its initial length. Finally the composite film with the load was annealed at 70 °C overnight to complete the crosslinking reaction in the nematic phase (second crosslinking stage). All the prepared fiber-network/SWCNT/LCE composite films have dimensions around 90 mm×12 mm×0.8 mm.

6.2.2 Design, fabrication and simulation of the light concentrator and heat collector (LCHC) structure

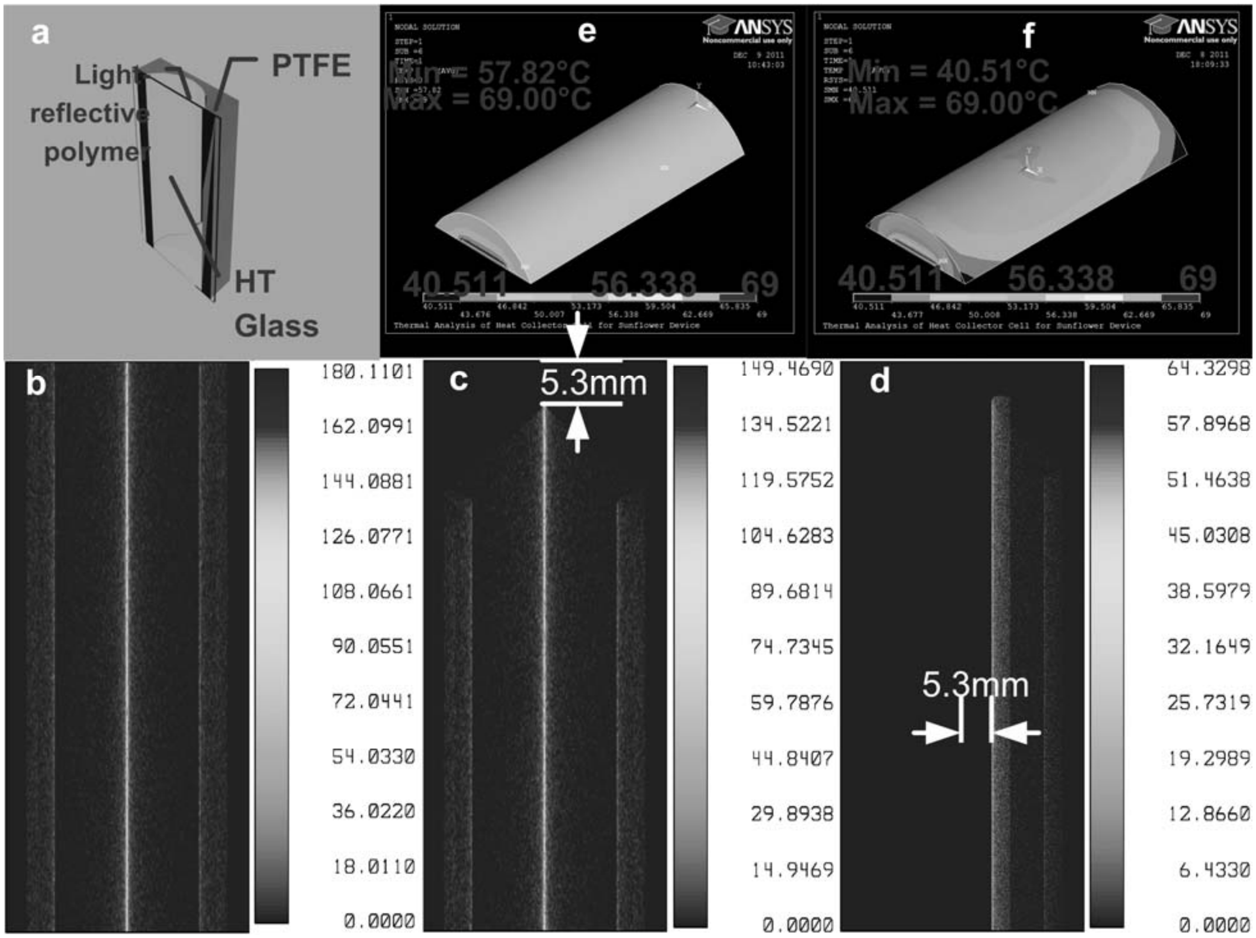

Figure 6-4. The LCHC in the solar-tracking system. (a) 3D schematic of the LCHC and its components. (b) Zemax® simulation of the intensity distribution of the collected and refocused light from a normal incident (0° altitude, 180° azimuth) collimated light beam (intensity: 100mW/cm^2), on the plane where the actuator resides. (c) Intensity distribution on the same plane with an incident collimated light illuminating from 30° altitude and 180° azimuth. (d) Intensity distribution at the same plane with an incident collimated light illuminating from 30° altitude and 150° azimuth. (e) Contour plot of the air temperature distribution inside the LCHC by simulation using ANSYS®, considering the radiation absorption of the black PTFE bulk. (f) Contour plot of the air temperature distribution

around the actuator without an LCHC. The temperature of the actuator was set at 69°C (> T_{ni}) and the ambient temperature was set at 22°C. Comparing (e) and (f), the heat dissipation with LCHC is much less than without an LCHC.

Second, a relatively simple structure is designed to accompany the nanocomposite film actuators to ensure the actuation under natural sunlight (1 Sun, Air Mass 1.5 G), since, according to our previous experiments, the fiber-network/SWCNT/LCE nanocomposite needs at least 230 mW/cm^2 of white light radiation to be fully actuated. This structure [Figure 6-3(a)] serves as both a light concentrator and a heat collector (LCHC). The high-reflectivity multilayer polymer film at the inner back of the structure forms a cylindrical mirror, and the actuator is placed close to its focal line. The distribution of the intensity of the reflected light at the plane where the actuator is placed is simulated using Zemax®. As shown in Figure 6-3(b), the major portion of the incident light is collected by the cylindrical mirror and focused back onto the actuator plane. The position of the focal line translates as the direction of the incident light varies. As shown in Figure 6-3(c) and (d), when the altitude and the azimuth of the incident light both deviate around 30° from the normal incidence, the focused line moves vertically laterally, both by ~5.3mm. Thus, in our design, we use actuators with widths of more than 12 mm and lengths more than 75 mm to ensure that the major part of the focused light would be onto the actuator film. The black polytetrafluoroethylene (PTFE) bulk of the LCHC structure helps maintain a higher local temperature around the actuator by reducing the heat conduction with its low thermal conductivity [~0.25W/(m*K)]. The LCHC chamber is also semi-sealed by a high-transmittance glass slide, greatly reducing the airflow and heat convection around the actuator. Simulation result by ANSYS® shows that the LCHC is able to maintain the temperature of the air inside the LCHC [Figure 6-3 (e)], while without the LCHC the heat dissipates to the ambient much more easily [Figure 6-3(f)]. As a result, the utilizing of the LCHC ensures that the temperature of the fiber-network/SWCNT/LCE actuator stay above its T_{ni} when the actuator is facing the sunlight, which, subsequently ensures the actuator remains in the contracted state after several seconds of sunlight radiation.

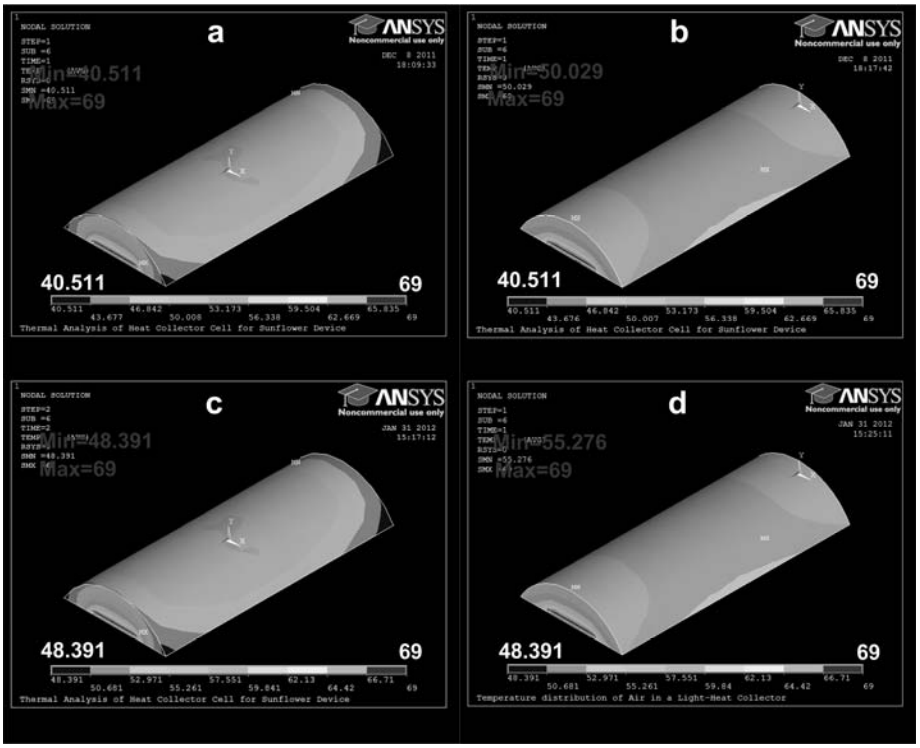

Figure 6-5. ANSYS® simulation results (contour plots) of the air temperature distribution in different circumstances. (a), Results without an LCHC in a laboratory circumstance; (b), Results within an LCHC in the laboratory circumstance; (c), Results without an LCHC in an in-field circumstance; (d), Results within an LCHC in the in-field circumstance.

Simulation was conducted intensively to determine the heat-collecting property of the LCHC, and the results are shown in Figure 6-5. We employed ANSYS$^{®}$ 12.1 to analyze the heat-confining ability of our LCHCs. Here we utilized a simplified model by setting the actuator at a fixed temperature (> T_{ni}) and comparing the heat dissipation with and without the LCHC. This essentially studies, assuming the actuator is heated up due to the concentrated light from the cylindrical mirror, how well the LCHC could help maintain the temperature of the actuator. Two circumstances were considered: the laboratory testing with a white light source, and the in-field testing with natural sunlight. After observing the contraction of the actuator and measuring its surface temperature during its operation by a multilogger thermometer (HH 506 RA, OMEGA Engineering, Stamford, CT, USA), we picked a reasonable actuator temperature of 69°C for both circumstances. The ambient temperature was set at 22°C (room temperature) to simulate the laboratory circumstance and at 35°C to simulate the in-field circumstance. While calculating the heat dissipation, only heat transfer by conduction and convection were taking into account. Thermal convection constraints were applied at all “free” surfaces such as the surface of the actuator, and the inner and outer surfaces of the LCHC. We also assumed that there was little forced-convection as we put our device in a transparent chamber to further reduce the convection by wind or air-flow. The natural thermal convection coefficient was assumed to be 2.542 $W/(m^2 \times K)$ in the in-field circumstance, larger than that in the laboratory circumstances [1.622 $W/(m^2 \times K)$]. The simulation results are shown in Figure 6-5, where in Figure 6-5(a) and (b) depict the laboratory circumstances, and Supplementary Figure 6-5(c) and (d) depict the in-field test circumstances. Figure 6-5(a) shows the air temperature distribution around the actuator without an LCHC, while Figure 6-5(b) shows the air temperature around the actuator in an LCHC. Similarly, Supplementary Figure 6-5(c) shows the air temperature distribution around the actuator without an LCHC, while Figure 6-5(d) shows the air temperature around the actuator in an LCHC. By comparing Supplementary Figure 6-5(a) and (b), the effectiveness of the LCHC of maintaining the heat is proved, as in Figure 6-5(a) the air temperature within the LCHC is kept above 50°C, while in Figure 6-5(b) the air temperature around the actuator drops quickly to 40°C. Similar conclusion can be drawn from Figure 6-5(c) and (d).

The materials needed for the fabrication of the LCHC is needed as following: Black static-dissipative PTFE bulk material, light reflective film (thickness: 0.0026 inch, estimated reflectivity: 99.8%), and high transmittance glass were purchased from McMaster-Carr, Inc (Elmhurst, IL). The PTFE bulk material was shaped and polished with a mill (GEVS500A, Eisen Machinery, Inc., Santa Fe Springs, CA). Then, the light-reflective film was bonded with the cylindrical surface of the PTFE bulk by a thin adhesive tape (~0.06mm, 3M Inc., St Paul, MN). The dimensions of the LCHC is shown in Figure 6-6 (a) (b) and (c).

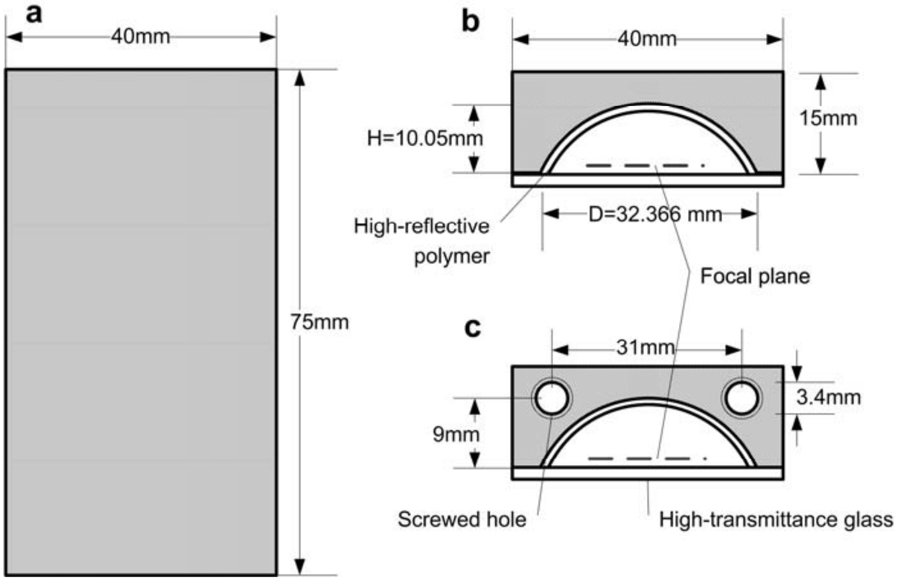

Figure 6-6. Dimensions of the LCHC.

6.3 Design and fabrication of the artificial heliotropism devices

The 3D structure of a prototype device with three LCHC-actuator units that was used for laboratory testing has already been shown by Figure 6-1(a). The LCHCs as well as a flexible supporting beam were fixed on a pedestal. The beam supported a light-weight platform to hold the solar cells. The platform was initially positioned horizontally. The actuators were placed inside the LCHCs, with one ends fixed on the pedestal and the other ends fixed on the solar cell platform. The pedestal of the prototype device was made from black PTFE. As shown in Fig. 6-7(a), the layout of the LCHC-actuator units on the pedestal is illustrated by the dashed line, and the positions of the straight holes matched the screwed holes on the LCHCs. Each actuator was fixed in the actuator slot, which was 15mm in length, 1.6mm in width, and 2.5mm in depth. The solar cells that we purchased are rectangular [length: 34mm, width: 23mm, from Hobby Engineering, Inc. (South San Francisco, CA)]. We connected these rectangular solar cells in series and arranged them in a central-symmetrical fashion on a hexagonal cardboard.

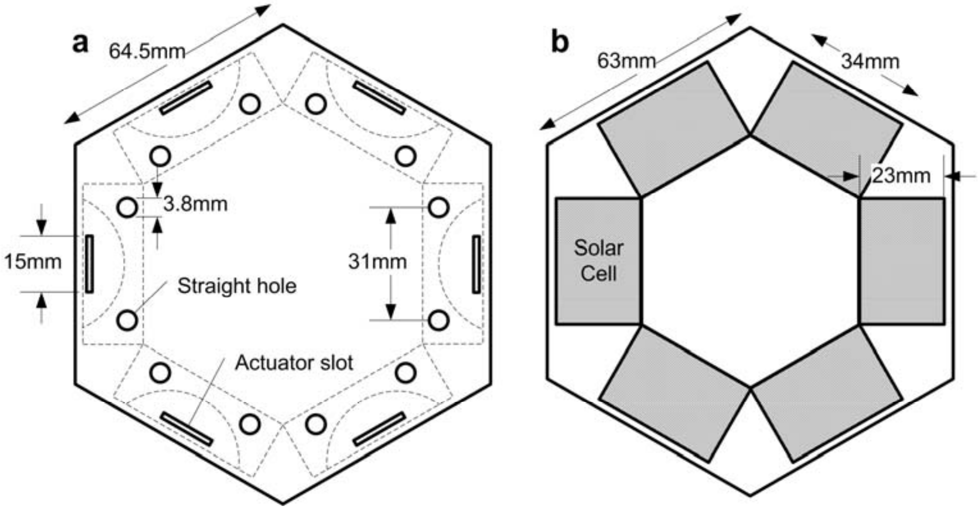

Figure 6-7. Schematic showing (a), the pedestal and its dimensions, and (b), the platform holding the solar cells. The solar cells were electrically connected in series.

6.4 Artificial heliotropism experiments and results

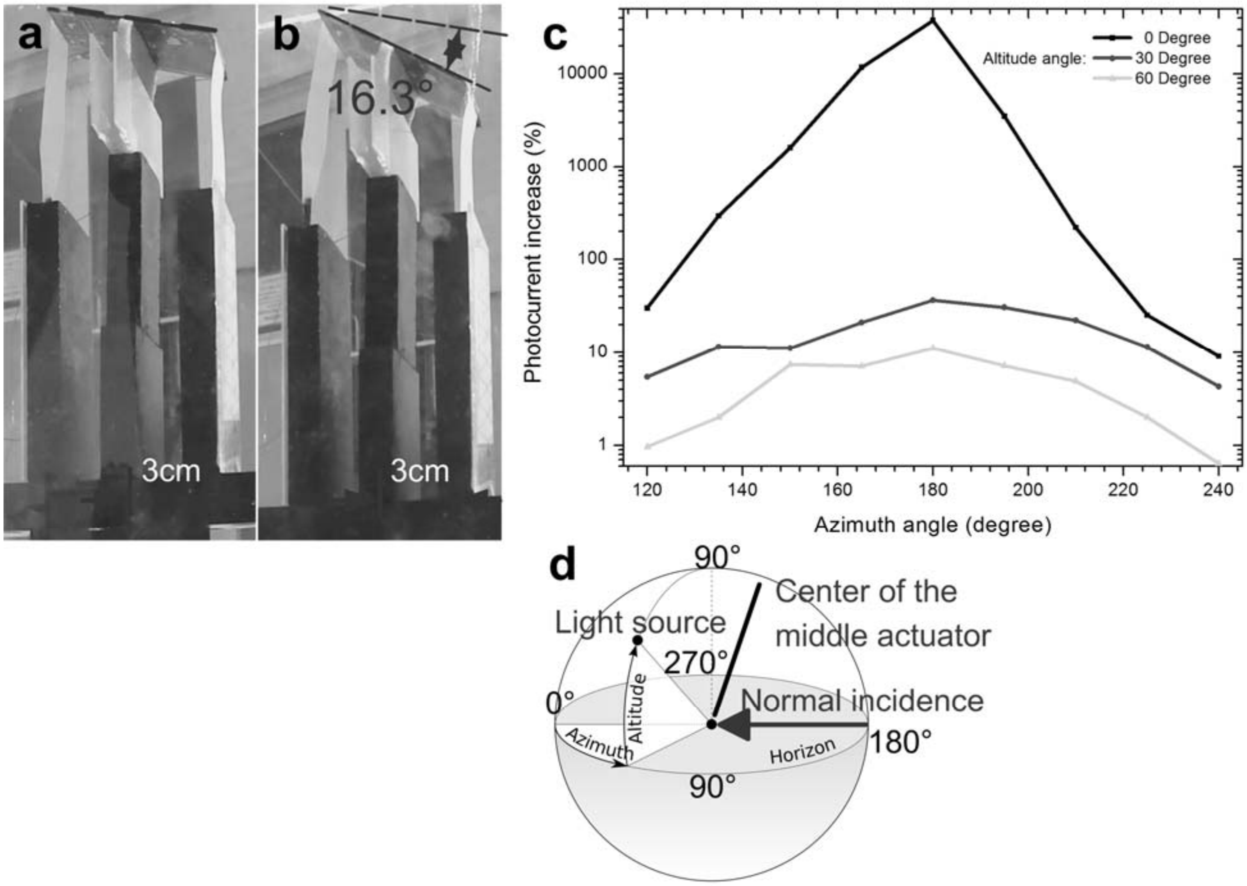

Figure 6-8. (a) (b) Light-tracking behavior of a 2-LCHC-actuator-unit device during one in-field testing at 43°4′20″N, 89°24′44″W on August 3rd, 2011. Initially the device was blocked from the sunlight. (a) The actuator was just exposed to the sunlight and began to contract. (b) After 110s, the actuator achieved a full contraction state and the solar cell was tilted by 16.8°. (c) Photocurrent increase owing to light tracking with a single LCHC-actuator unit. The incident light was kept at 100mW/cm^2 but was from different directions. (d) The altitude-azimuth coordinate system used. The origin was the center of the actuator in the middle. The normal incidence direction was 0° altitude, 180° azimuth.

We then characterized the solar-tacking capability of a single unit consisting of one LCHC and one fiber-network/SWCNT/LCE film actuator (~80mm×12mm×0.8mm) placed at the focal line of the cylindrical mirror of the LCHC. In-field tests were performed between July and August, 2011 in Madison, WI, USA. Two units were utilized but only one would face towards the sun in these tests. Figure 6-8(a) and (b) shows the result during one in-field testing at 43°4′20″N, 89°24′44″W on August 3rd, 2011. Initially the device was blocked from the sunlight. Then the actuator in the right unit was made facing the sun and started to contract. In ~110 seconds, it stopped contraction and the solar cell was tilted towards the sun by 16.8°. The increase in photocurrent output from the solar cells due to solar-tracking *vs*. the direction of the incident light was characterized in our laboratory so that the tests would be less affected by natural elements such as wind, haze, and clouds. In these laboratory tests, the solar cells were initially horizontal (the photocurrent output at this initial state was the baseline), and the incident light was from a white light source (intensity: 100mW/cm^2; partially collimated; spot diameter: 101.6 mm). Figure 6-8(c) shows the results. The direction of the incident light is identified by the altitude angle and the azimuth angle of the light source with respect to the center of the actuator, considering the direction of "normal incidence" to the actuator as 0° altitude and 180° azimuth [Figure 6-8(d) shows the altitude-azimuth coordinate systems used]. Light-tracking owing to one LCHC-actuator unit was able to increase the photocurrent output by up to ~37500% at normal incidence (note that the base photocurrent was low in this situation), and by more than 100% in the 150°-210° azimuth range at 0° altitude. When the altitude angle of the light source increased to 60°, increase in the photocurrent was still more than 4%. Altitude more than 60º (e.g. 70º) left little room for increasing the photocurrent by light tracking, as it was already fairly close to normal radiation onto the solar cells. From the experiments indicated by Figure 6-8, for one LCHC-actuator unit, an empirical estimation of the effective range of solar tracking is thus 0º - +60° in altitude angle and between ±30° in azimuth angle, with respect to the “normal incidence”.

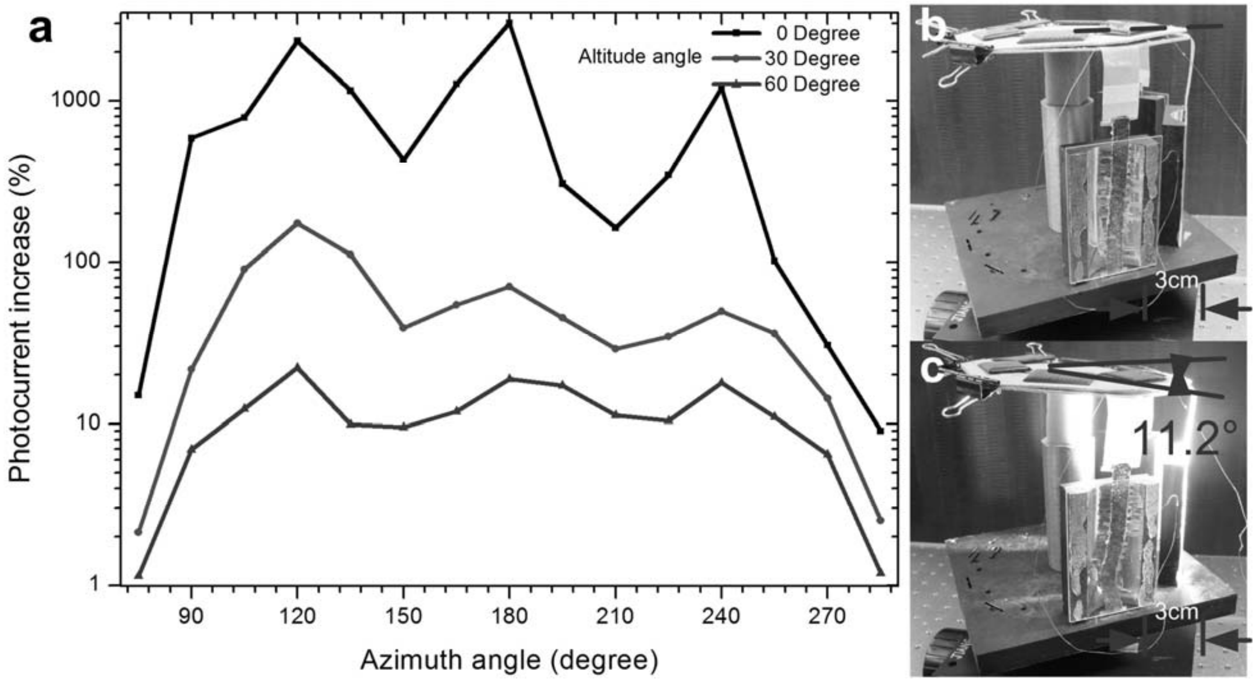

Figure 6-9. (a) Photocurrent increase owing to light tracking by the prototype device with 3 LCHC-actuator units. A similar altitude-azimuth coordinate system in Fig. 3D was used. Origin was the center of the actuator in the middle. (b) (c) Light-tracking behavior of the 3-LCHC-actuator-unit prototype device in laboratory. Irradiation was from a white light source (intensity: 100mW/cm^2; partially collimated; spot diameter: 101.6 mm; 0° altitude; 180° azimuth). (b) Before irradiation. (c) 30s after irradiation was on.

Considering the information of the solar-tracking range of a single LCHC-actuator unit as well as data related to the solar altitude and azimuth angles [17], we then realized prototype device designs that utilized multiple LCHC-actuator units for full-range solar tracking, as described in section 6.3. First, a typical range of solar altitude angle during a day at most locations in the U.S. is 0° (dawn or dusk) to 70° (midday). Second, though the solar azimuth angle range during a day at most U.S. locations varies, a coverage from 90° (6-8 a.m.) to 270° (5-7 p.m.) in the azimuth angle would be sufficient. Therefore, a design utilizing three or four LCHC-actuator units (three shown in Figure 6-9) could provide full range of solar tracking. The LCHC-actuator units were arranged centrosymmetrically, with a 60° angular separation between their medial axes. With this arrangement, 3 LCHC-actuator units were placed corresponding to azimuth angles of 120°, 180°, and 240°, respectively, and the resultant range of solar tracking is essentially the superposition of that from each single unit. The increase in the solar cell photocurrent output with this prototype device with 3 LCHC-actuator units *vs.* the direction of the incident light from the same white light source as above is shown in Figure 6-5. As expected, at 0° altitude and 120°, 180°, or 240° azimuth, the light-tracking effect was the strongest, with an increase in the photocurrent by up to 3700%. The effective azimuth light-tracking range was indeed nearly tripled. The increase in photocurrent was more than 100% at 0° altitude. Within most of the 90°-270° azimuth range, even when the altitude angle increased to 60°, the photocurrent was still increased by around 10%. Figure 6-9 (b) and(c) show the images of this device in one laboratory test; the platform with solar cells tilted towards the light source after the actuation (incident light - 0° altitude, 180° azimuth). In-field tests of a similar prototype device with 4 LCHC-actuator units were conducted from August to September, 2011 in Madison, WI, USA. The solar-tracking range and the increase in the solar cell photocurrent output were consistent with the results obtained in the laboratory environment.

6.5 More details about the in-field and in-lab artificial heliotropism experiments and results

6.5.1 Device testing under natural sunlight

Devices were tested under natural sunlight between July and September, 2011, in Madison, WI. The GPS coordinate of the two testing locations in Madison, WI, USA were 43°4′20″N and 89°24′44″W (location I), and 43°5′12″N and 89°26′31″W (location II). The tests demonstrated effective artificial heliotropism under natural sunlight using our LCHC-actuator units. Artificial Heliotropism using 2 LCHC-actuator units (only one of them was actuated during the testing) was tested from July to August, 2011. A prototype device with 4 LCHC-actuator units was tested in-field from August to September 2011. The device was similar to the 3-LCHC-actuator-unit device we used for laboratory testing, with a larger heliotropic range. The devices were put in a chamber (made from clear casting acrylic sheet, 12 inches × 12 inches × 12 inches) during the test, to reduce the effect of wind outdoor (average wind speed ~12 mph). The transmittance of the acrylic sheets in the visible light range was around 95%, while the main portion of the UV-spectrum was blocked by the acrylic sheets. Effects of clouds and haze were also a major issue; hence we chose to conduct experiments in sunny/clear or partly cloudy days. Before each test, the air temperature around the device and the ground surface temperature were measured using a multilogger thermometer (HH 506 RA, OMEGA Engineering, Stamford, CT), and the intensity of incident sunlight was estimated using an intensity meter (FieldMax II-P, Coherent, Inc, Santa Clara, CA). Before and after each test, the complete testing unit including the chamber was blocked from sunlight to reset the actuators. During most experiments, the photocurrent output was monitored by a digital multimeter (Model 34401A, Agilent, Santa Clara, CA, USA). The heliotropic behavior of the devices during each test was video-taped using a digital camera (model: 13655, Konica Minolta, Inc., Ramsey, NJ, USA). The detailed parameters pertinent to six standard experiments are listed in Table 6-1, and the movies corresponding to them are also available upon request. The reference coordinate of both the device position and the camera shooting angle was defined as: 0° altitude - parallel to the ground surface; 0° azimuth - straight towards the north [Figure 6-8(d)]. Figure 6-10 depicts the increase in the photocurrent output from the solar cells *vs*. time in one typical experiment (corresponding to Experiment 3) after the actuator was exposed to the sunlight (time instant 0). Roughly 15% of increase was observed after 80s, when the actuator reached and maintained the most contraction. Note that this measurement was slightly affected by the natural elements during the process, especially clouds and haze.

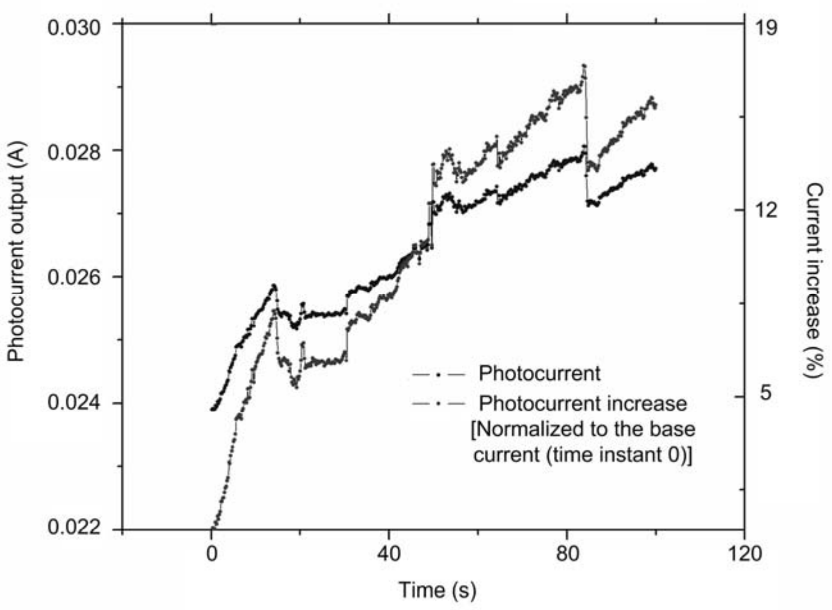

Figure 6-10. Photocurrent output (blue) and increase in percentage (red) vs. time after the actuator was exposed to the sunlight (time instant 0). The photocurrent increase was normalized to the current at time instant 0. The measurement stopped at the time instant of 100s.

Table 6-1. Detail of the typical in-field experiments. The "initial device position" refers to the direction which is normal to the actuator plane of the functioning LCHC-actuator unit. The reference coordinate of both the initial device position and the camera shooting angle was defined as: 0° altitude - parallel to the ground surface; 0° azimuth - straight towards the north.

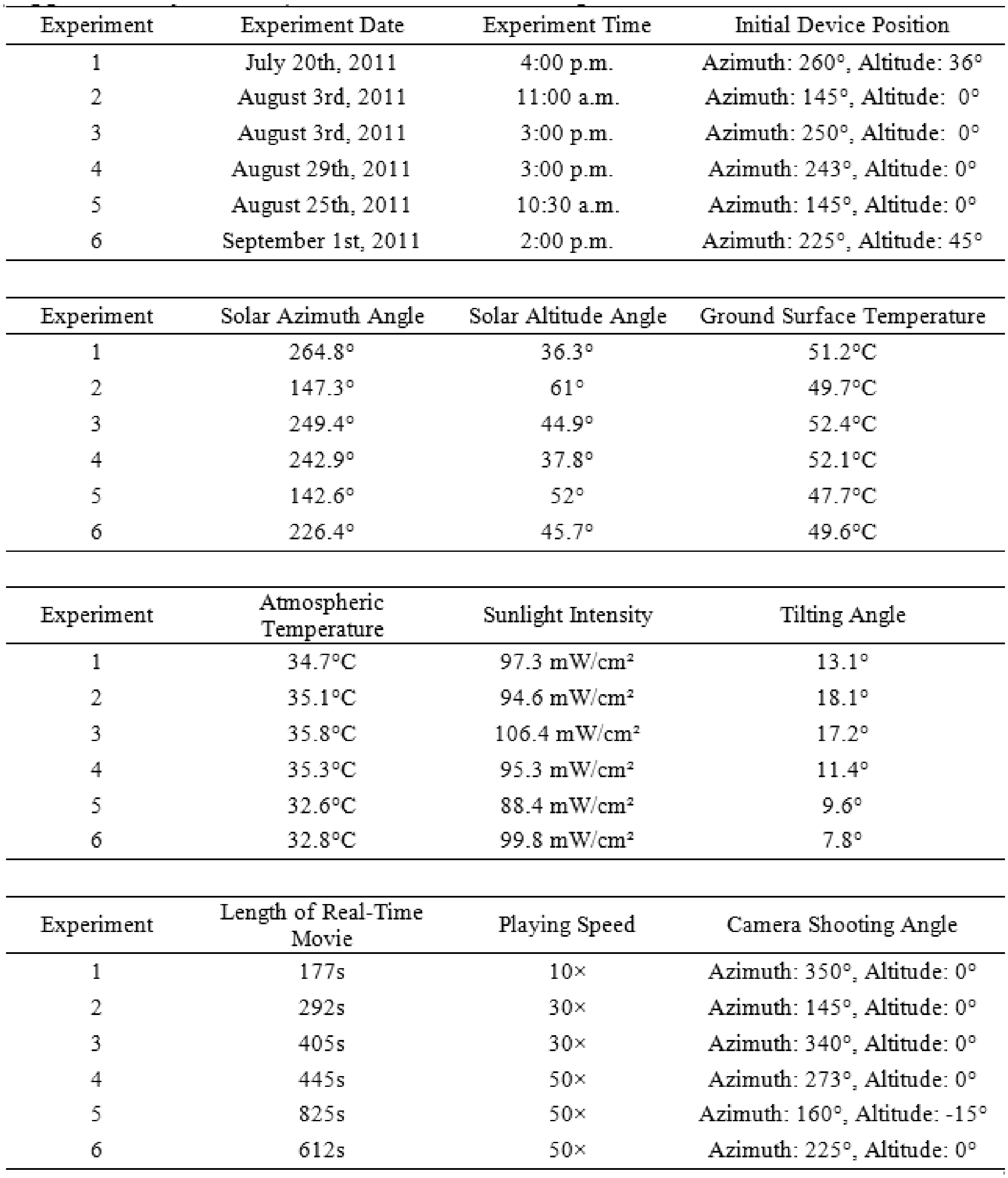

Experiment	Experiment Date	Experiment Time	Initial Device Position
1	July 20th, 2011	4:00 p.m.	Azimuth: 260°, Altitude: 36°
2	August 3rd, 2011	11:00 a.m.	Azimuth: 145°, Altitude: 0°
3	August 3rd, 2011	3:00 p.m.	Azimuth: 250°, Altitude: 0°
4	August 29th, 2011	3:00 p.m.	Azimuth: 243°, Altitude: 0°
5	August 25th, 2011	10:30 a.m.	Azimuth: 145°, Altitude: 0°
6	September 1st, 2011	2:00 p.m.	Azimuth: 225°, Altitude: 45°

Experiment	Solar Azimuth Angle	Solar Altitude Angle	Ground Surface Temperature
1	264.8°	36.3°	51.2°C
2	147.3°	61°	49.7°C
3	249.4°	44.9°	52.4°C
4	242.9°	37.8°	52.1°C
5	142.6°	52°	47.7°C
6	226.4°	45.7°	49.6°C

Experiment	Atmospheric Temperature	Sunlight Intensity	Tilting Angle
1	34.7°C	97.3 mW/cm²	13.1°
2	35.1°C	94.6 mW/cm²	18.1°
3	35.8°C	106.4 mW/cm²	17.2°
4	35.3°C	95.3 mW/cm²	11.4°
5	32.6°C	88.4 mW/cm²	9.6°
6	32.8°C	99.8 mW/cm²	7.8°

Experiment	Length of Real-Time Movie	Playing Speed	Camera Shooting Angle
1	177s	10×	Azimuth: 350°, Altitude: 0°
2	292s	30×	Azimuth: 145°, Altitude: 0°
3	405s	30×	Azimuth: 340°, Altitude: 0°
4	445s	50×	Azimuth: 273°, Altitude: 0°
5	825s	50×	Azimuth: 160°, Altitude: -15°
6	612s	50×	Azimuth: 225°, Altitude: 0°

6.5.2 Device testing in laboratory:

To better characterize the increase in the photocurrent output from the solar cells owing to artificial heliotropism while avoiding the effects of natural elements such as wind, clouds and haze, experiments were conducted in a dark room in our laboratory. The room temperature was kept around 22°C and airflow was also carefully limited. The devices (with two LCHC-actuator units and three LCHC-actuator units, respectively) were attached on a horizontal rotational stage, so that the azimuth angle could be adjusted from 0° to 360° by rotating the stage. A white light source (New Port, Oriel Productline, Model 66885, Irvine, CA, USA) was used as the actuating light. Due to the required high intensity of light and large spot size, the output beam was only partially collimated, and the light intensity in the center of the round-shaped output beam was the highest. The original light beam was reflected by a high-reflective mirror (diameter: 4 inch, reflectivity: 99.8%), whose position and reflection angle was varied to adjust the altitude angle of the incident light onto the solar cells. The spot diameter of the incident light was kept at ~101.6mm, and the intensity at the center of the incident beam spot was kept at ~100mW/cm^2. The center of the incident beam spot was kept at an “aligned position” with the center of the functioning LCHC-actuator unit (i.e., if we connect these two points by a line, this line was kept to be parallel to the incident light beam). By doing so, a uniform irradiation upon the functioning LCHC-actuator unit was realized with an intensity of 100mW/cm^2. Unlike the in-field tests, normal incidence during the lab tests was arbitrarily defined: the direction normal to the actuator plane of the LCHC-actuator unit in the middle was defined as 0° altitude and 180° azimuth.

During the tests, the altitude of the incident light was fixed at first and the azimuth angle was changed from 180° to 90° and then from 180° to 270° in steps of 15° (by rotating the stage). Then the angle of the mirror was adjusted to change the altitude steps of 30° (i.e., 0º, 30º and 60º). As in the in-field tests, the photocurrent output of the solar cells connected in series was monitored by the same digital multimeter as described previously.

6.6 Conclusion

We have demonstrated artificial heliotropism for solar cells, utilizing fiber-network/SWCNT/LCE actuators that can be directly driven by the sunlight instead of relying on other power consuming components for tracking the sun and actuation. When these actuators face the sun, they contract, and as a result, tilt the solar cells towards the sun, thus the artificial heliotropism. Both laboratory tests and in-field tests confirmed that the devices were capable of full-range artificial heliotropism, with 60 of range in altitude angle, and 180 of range in azimuth angle. Significant increase in the output photocurrent of the solar cells was observed owing to the artificial heliotropism. In the future, we will improve the LCE nanocomposite for larger contraction ratio, lower threshold of response to the sunlight, and higher loading capability. We will investigate on improving the LCE matrix materials and the continuous fibers, as well as the effect of the orientations of carbon nanotubes in regard to the nematic LCE matrices on the nematic orders and the photo-thermomechanical actuation performance. We will also improve the design for more effective heliotropism, and scale up the system design to accommodate large solar panels. Our artificial heliotropism for solar energy harvesting is an effective approach to making the best use of the solar energy as a renewable clean energy source. Our approach can further be combined with others that aim to enhance the solar-to-electric conversion efficiency of the solar cells themselves and those that incorporate solar concentrators.

6.7 References

[1] K. W. J. Barnham, M. Mazzer, B. Clive, *Nature Mateials,* vol. 5, pp. 161 (2006).

[2] D. Kraemer *et al.*, *Nature Mateials,* vol. 10, pp. 532 (2011).

[3] B. O'Regan, M. Grätzel, *Nature,* vol. 353, pp. 737 (1991).

[4] H.-Y. Chen *et al.*, *Nature Photonics,* vol. 3, pp. 649 (2009).

[5] K. Araki *et al., Progress in Photovoltaics: Research and Applications,* vol. 13, pp. 513 (2005).

[6] J. Yoon *et al.*, *Nature Communications,* vol. 2, pp. 343 (2011).

[7] M. J. Currie, J. K. Mapel, T. D. Heidel, S. Goffri, M. A. Baldo, *Science,* vol. 321, pp. 226 (2008).

[8] M. R. Lee *et al.*, *Science,* vol. 324, pp. 232 (2009).

[9] J. W. Schwede *et al.*, *Nature Materials,* vol. 9, pp. 762 (2010).

[10] R. A. Sherry, C. Galen, *Plant, Cell and Environment,* vol. 21, pp. 983 (1998).

[11] The Renewable Resource Data Center, National Renewable Energy Laboratory*, PVWATTS online data system* (2011*),* http://rredc.nrel.gov/solar/calculators/PVWATTS/version1/US/Wisconsin/Madison.html.

[12] H. Mousazadeh *et al.*, *Renewable and Sustainable Energy Reviews,* vol. 13, pp. 1800 (2009).

[13] C. Li, Y. Liu, C. Lo, H. Jiang, *Soft Matter,* vol. 16, pp. 7511 (2011).

[14] P. M. Ajayan *et al.*, *Science,* vol. 296, pp. 705 (2002).

[15] A.R. Tajbakhsh and E.M. Terentjev, *The European Physical Journal E,* vol. 6, pp. 181 (2001).

[16] A. Greve, H. Finkelmann, *Macromolecular Chemistry and Physics,* vol. 202, pp. 2926(2001).

[17] The U.S. Naval Observatory (USNO), *Sun or Moon Altitude/Azimuth Table* (accessed 2/28/2012), http://aa.usno.navy.mil/data/docs/RS_OneDay.php.

[18] J. Kupfer, H. Finkelmann, *Makromolekulare Chemie, Rapid Communications,* vol. 12, pp. 717 (1991).

[19] R. Ramasubramaniam, J. Chen, H. Liu, *Applied Physics Letters,* vol. 83, pp. 2928 (2003).

[20] S. Courty, J. Mine, A. R. Tajbakhsh, E. M. Terentjev, *Europhysics Letters,* vol. 64, pp.654 (2003).

Chapter 7. Conclusion and Future Work

7.1 Conclusion

Two distinct yet relative research fields: analytical microfluidic and optofluidic systems utilizing multiphase interfaces for (biochemical) sensing, and novel photomechanical actuators which can both be integrated in above analytical micro systems and energy harvesting devices, the former, however, has been demonstrated.

Three different analytical microfluidic and optofluidic systems utilizing multiphase interfaces were demonstrate, used for sample collecting, real time sensing and sensing enhancement. The first one includes devices with reliable liquid-air interfaces for aerosolized particle and gas collection (and detection) using different methods. The simplistic and inexpensive fabrication of these devices provides robustness and the potential to integrate them into practice detection systems. With liquid-air interfaces pinned at hydrophilic/hydrophobic SAM-gold/glass interfaces, we have demonstrated channel devices with lateral gas-liquid interfaces, and further optimized the channel structure to increase the exposing interface area to the environment analytes. We also demonstrated collecting devices utilizing air pillar structure to pin the liquid–gas interface at the edge of patterned holes. Because of the much simpler fabrication process and robust materials (i.e. no SAM thin film), these devices have much longer shelf life, lower cost and better compatibility. Moreover, the capability of collecting different analytes in the environment simultaneously with different levels has been demonstrated by multi-level air pillar devices. The potential of the devices for real-time collecting and analyzing of aerosolized or gaseous chemical and biological agents have also been demonstrated by both direct observation and measurement of the conductance of collecting liquid.

The second system includes microfluidic devices integrating *in situ* thermotropic LC sensing into microfluidic channel. The fluidic dynamic phenomenon in the laminar flow regime was investigated and employed to create a layer of LC thin film in an autonomous fashion, which greatly improved the efficiency of preparing the delicate LC sensing element and eliminated the complicated and skill-required manual handling. The subsequent sensing tasks thus can be *in situ* conducted, and remotely controlled by lab-on-a-chip control methods. As a result, the devices inherit the high sensitivity, real-time sensing and label-free detection properties from LC sensing, and meanwhile possess the capability to conduct multiple consecutive sensing tasks, as well as the detecting tasks in the hazardous environment inaccessible to human being. Two model systems were demonstrated on the sensing devices. The alternative flow of the aqueous dispersion of DTAB surfactant and DI-water was detected by the orientational transits of the LC mesogens and reflected as the real time change of the LC optical texture. LC optical texture change also effectively indicated the spontaneously assembling of the L-DLPC phospholipid monolayer at the LC interface and subsequently, the binding/hydrolyzing event of PLA_2 in the sensing channel with this phospholipid monolayer.

The third system is an optofluidic system of *in situ* formed tunable liquid microlens arrays. Design, fabrication and formation of 2 microlenses in a single batch have been reported, and the microlenses in the array are demonstrated to be capable of separately tuning. This shows the potential of making microlens arrays with more separately tunable microlenses (only need to add more pressure control components and more air conduit channel). Within such an array, the multiple micolenses with optical axis parallel to the substrate plane have the potential to enhance lab-on-a-chip detection at different spatial points (i.e. x-axis in space cartesian coordinate system) along the detection channel. Meanwhile, the parallel liquid microlens is used to enhance fluorescence excitation signals because of their function to converge an excitation light beam. The fluorescence emission signal is thus enhanced, as well as the detection sensitivity and the lower analyte concentration limit. By tuning the focal length of our microlenses, the area of the fluorescence zones can be greatly enlarged (by 13 times), and the fluorescence signal can be effectively enhanced (by up to 38 times). The relationships between the profile/shape of the fabricated microlenses and factors such as pressure and gravity were examined by simulation. The optical properties of the lenses, including focal length and lateral aberration were also examined through a ray-tracing simulation. The potential applications of our microlenses in lab-on-a-chip applications were also demonstrated by using it to enhance the fluorescence emission in an integrated detection channel.

To provide a novel method for remotely controlling of certain micro systems directly by photo-mechanical coupling, a novel opto-thermo-mechanical actuator based on SWCNT incorporated liquid crystal elastomer (LCE) is developed and characterized. High concentration of SWCNTs can be loaded and effectively dispersed into the LCE matrix in this simple process, and relatively thick films can be fabricated. Some salient characteristics were observed: the SWCNT–LCE nanocomposites can not only be actuated by IR light as previously reported, but also by much wider spectrum of light with an intensity on the order of 100mW cm^{-2}. Filling SWCNTs in LCE matrix can also help improve the mechanical properties, which also enhances the practicability of the materials.

Such actuators were then used in a system for energy harvesting, in order to maximize the utilization of its capability that it can be directly driven by sunlight. Self-adaptive artificial heliotropism for photovoltaic energy harvesting systems has been demonstrated, instead of relying on other power consuming components for tracking the sun and actuation. When these actuators face the sun, they contract, and as a result, tilt the solar cells towards the sun, thus the artificial heliotropism. Both laboratory tests and in-field tests confirmed that the prototype devices were capable of full-range light tracking, with 60º of range in altitude angle, and 180º of range in azimuth angle. Significant increase in the output photocurrent of the solar cells was observed owing to the artificial heliotropism.

7.2 Future Work

For the aerosolized particle and gas collecting devices with reliable liquid–air interfaces, future works may include four aspects. Firstly, for the channel devices, the quality of the surface treatment could be further improved, and more calculation and optimization is needed to further increase the exposed surface area, and to make a trade-off between a higher flow rate (i.e. a high collecting rate) and a larger risk of breaking the water balance and wearing-out of the SAM (i.e. a shorter life for operating). Secondly, the air pillar structures can be expanded to multiple layers by stacking more glass slides with aligned holes. Thirdly, in the gold channel structure, the analytes enter the stream from the lateral direction; while in the air pillar structure, the analytes enter the stream from the vertical direction. Hence, a combination of the two structures is possible where the device collects analytes from both the lateral and vertical directions; the collecting efficiency is expected to be enhanced. Moreover, for the real-time sensing experiment, electrodes with different kinds of metals should be used as the sensing probe, especially inert metals such as gold and platinum, for better sensitivity and less affect to the bias resistance of the bulk flow. Finally, with an accurate control module, and either structure as the core device, an automatic total analysis system on a chip could be implemented, which would further demonstrate the commercial potential of our designs.

For the LC sensing microfluidic systems in future, we will focus on using photon detectors to quantify the intensity of the light transmitted through the LC and polarizers. By varying the critical dimensions of the devices and control profiles of the system, we can also find the optimizations for the system. Moreover, detection of interactions of other biochemical systems can be demonstrated in the future.

For the *in situ* formed tunable liquid microlenses, further data analysis and optimization of the pneumatic control of the microlens arrays structure, and integration of more microlenses into the microchannel to form a microlenses array would be the prior future work. Another interesting work would be performing a 2-D scan of the whole detection channel by separately focal-length tuning of microlenses at different spatial locations in a microlens array. After that, since in lab-on-a-chip systems, controlled microfluidic interfaces are also important and as our microlens array directly faces the cross sections of these interfaces, the potential for surface reaction study at such interfaces by the microlens array would be useful. Investigations and calculations should be performed to determine whether the lens droplet will form plano-convex or convex meniscus morphology. Optical properties of the lens should also be examined by experiment.

For the novel SWCNT/LCE opto-thermo-mechanical actuators, the effects of SWCNTs on the mechanical properties of the LCE nanocomposites should be investigated. The mechanism of lowering of transition temperature of the LCE with incorporated CNTs should also be further investigated. Moreover, utilizing this actuator in optofluidic systems would be an interesting project. The dispersion of the SWCNT in LCE matrix is also in need to be improved by functionalizing the SWCNT and alleviating the aggregation problem of carbon nanotubes. Alignment of CNTs in the matrix, should also be studied to see if it plays a role in the modification of the properties of the LCE matrix.

For the actuator-enhanced artificial heliotropism energy harvesting system, we will be focusing on improving the LCE nanocomposite for larger contraction ratio, lower threshold of response to the sunlight, and higher loading capability. As shown in the results, the uniformity of photocurrent increase is determined by the "density" of the actuator-LCHC units used in the tracking range. Thus, we also need to improve the design to adapt more units in the tracking range for more effective solar tracking. We also need to analyze the stress of different parts of the devices, so as to reduce the inner stress which limits the performances of the devices. This is critical to the future scaling up of the system so as to accommodate larger solar panels. Miniaturization of the devices would be another direction for optimization, as miniaturization will release the requirement for a large actuator, and will also effectively reduce the inner pressure of the devices. To take advantage of the benefits brought by miniaturization without maximize the output current increase, artificial heliotropism arrays are also expected to be developed and utilized.